Title

Microfluidics-enabled 3D printing and its applications

Author

Mea, Hing Jii

Publication Date

2022

Peer reviewed|Thesis/dissertation

Microfluidics-enabled 3D printing and its applications

By

HING JII MEA

DISSERTATION

Submitted in partial satisfaction of the requirements for the degree of

DOCTOR OF PHILOSOPHY

in

Chemical Engineering

in the

OFFICE OF GRADUATE STUDIES

of the

UNIVERSITY OF CALIFORNIA

DAVIS

Approved:

Jiandi Wan

Steven George

Priya Shah

Committee in Charge

2022

ACKNOWLEDGEMENTS

I would like to thank Jiandi Wan for the confidence he placed in me in recruiting me to join his research group in the first place as well as inviting me to follow him from Rochester NY to Davis CA. His amicable and reliable hands-on style of mentorship, as well as his infectious curiosity/enthusiasm about all things science & engineering, has shaped me into the researcher I am today, and I am most grateful the opportunity to benefit from his guidance and support.

A big thanks to the various peer groups that have accompanied me throughout my graduate education, whether it's the Microsystems Engineering PhD incoming class of 2016, or the Chemical Engineering incoming graduate class of 2018. I will always cherish the times we sloughed through core classes together only to emerge on the other end stronger.

A special thanks to all my labmates and research assistants over the years: Dr. Rong Fan (Arthur), Dr. Sitong Zhou (Agnes), Xinye Chen, Tianyi Liu, Stephanie Boula, Yunju Chang, Yaojun Guo, Meghann Ma, Brianna Urbina, Yuting Zhou, Isabelle Crisostomo, Kyla Leacox, Miyu Horiuchi, Matthew Sujanto and Erin Shea. Much of my work would not have been possible without your support and assistance. In addition to your good spirits and eagerness to help, I sincerely appreciate your confidence in me and friendship throughout the years, and I wish you all the best in your future careers and endeavors.

To the various student groups who've had the (mis)fortune of having me as their teaching assistant, thank you for your good spirits and confidence in me even in trying times. Despite prior outward expressions of exhaustion and exasperation, I'm genuinely pleased and honored to have served as your instructor during the liminal and precious years of your undergraduate education.

I would also like to acknowledge the Microsystems Engineering department at Rochester Institute of Technology (RIT) and the Chemical Engineering department at UC Davis for their help and support over the years, especially amidst the times of transition (i.e. transferring) and challenge (i.e. COVID-19 pandemic).

To my family. To ma and pa, thank you for emulating for me a lifelong love for learning, and for helping me pursue my dreams. I stand upon your shoulders and am grateful every day for your love and support. To my siblings, thank you for your steady companionship over the years despite the spatial and temporal distance. Now that I'm finally done with school, I'm excited to see what the next chapter of life holds for us as family.

To my network of friends in diverse settings and locations, thank you for enriching my life. I regard my transience and moving around not as a breach of the bonds that tie us together, but an expansion. Thus, I am in many respects a stitching of the compassion, wisdom and love that you've extended to me. These I will carry forward wherever my travels take me.

Last but not least, I would like to thank God for the amazing gift of this life. As I celebrate this moment/milestone in my study and mastery of the tiny little corner/subset granted to me of the natural world, I recall that "it is the glory of God to conceal a matter, but the glory of kings to investigate a matter" (Proverbs 25:2). And so, in light of this kingly privilege among other providences, I must express my gratitude for arriving at this point. *Soli deo gloria*.

DISSERTATION ABSTRACT:

Microfluidics-enabled 3D printing and its applications

The emergence of 3D printing has revolutionized the world of manufacturing through its ability to enable production of parts with unparalleled geometric complexity and functionality. While the list of materials (e.g. polymers, ceramics, metals) compatible with 3D printing workflows grows steadily, multi-material printing has proved challenging, with existing strategies for mixing materials prone to introducing defects to the printed part (e.g. during nozzle swapping) or requiring robust electromechanical control systems to be in place that can be prohibitively costly. At the same time, microfluidics has been shown in the literature to excel at handling different material flow stream whether for mixing or swapping of multiple materials. With numerous studies over the past two decades thoroughly describing the physics of sub-millimeter flows along with various experimental setups for different applications (e.g. emulsification/droplet production, material synthesis), microfluidics technology is well-positioned to assist researchers in enabling new multi-material 3D printing workflows and applications.

This dissertation is a compilation of works demonstrating the adoption of microfluidic technologies and principles to enable multi-material 3D printing processes and novel applications in the areas of functional printing and tissue engineering. First, glass capillary microfluidic devices were adapted for use as printheads in a novel droplet-based 3D printing technique that allows for programmable tuning of printed object local properties through the inclusion of droplets at select points. Soft robotic grippers that respond to an external B-field and bend at select points were designed and printed to demonstrate the utility of this droplet-based 3D printing technique. Second, a multimaterial bioprinting workflow involving Matrigel bioink core within an agarose shell was developed to enable the enhancement of *in vitro* intestinal epithelium growth and tissue organization. These works showcase the continuing trend of exploiting the unparalleled spatiotemporal control of materials offered by microfluidics to facilitate multi-material 3D printing strategies and thereby contribute to the emerging body of knowledge on the matter.

TABLE OF CONTENTS

CHAPTER 1: INTRODUCTION

1.1 3D Printing Technologies and Capabilities

1.1.1 Introduction to 3D printing and applications in soft robotics & tissue engineering

Additive manufacturing or 3D printing refers to the sequential addition of material into specified shapes made using computer-aided design (CAD) and stands in direct contrast to conventional subtractive manufacturing wherein a substrate material is milled or cut into shape. An assortment of 3D printing methods has emerged that employ different workflows according to material processing applications, mostly relying on layer-by-layer patterning of material, such as thermoplastic filaments[1,2], metallic powders[3,4] or solution-based polymeric precursors[5–9] into their final shape. Compared to conventional subtractive manufacturing and machining processes, 3D printing is a more cost-effective and less energy-intensive manufacturing process due to the minimal amount of machining/cutting required and waste material generated (i.e. cutting fluids, lubricants, material debris)[10]. Moreover, in contrast to traditional subtractive or transformative manufacturing (i.e. die-casting, injection molding) that typically rely on economies of scales, 3D printing is highly cost effective at small scales, making it a widely accessible manufacturing technology for the general public.

Several 3D printing technologies have gained widespread adoption for different applications due to steady developments in equipment capabilities (e.g. stepper motors, temperature controls) and ability to process different materials, especially soft polymeric materials relevant in the areas of soft robotics and tissue engineering. In the area of soft robotics, extrusion-based and inkjet printing are highly favored as simple and reliably strategies for shaping soft polymers into complex shapes that are otherwise unattainable using traditional casting/molding methods[11]. Moreover, such methods are widely used for direct writing of functional inks, which is critical for imparting sensory or actuation capabilities to the soft robotic part[11–14]. For tissue engineering, extrusion-based and, more recently, light-based 3D printing is increasingly used as a means for shaping cell-laden biomaterials into physiologically relevant tissue constructs with a view towards drug/disease modeling and regenerative medicine (e.g. organ transplant)[6–8,15,16]. Although such 3D

printing methods can easily achieve sub-millimeter resolution, with some methods being more amenable to higher print resolutions than others, the ability to handle and mix multiple materials to create heterogeneous prints is still limited, with most commercial 3D printing setups being capable of handling only one ink stream at a time. Such limitations greatly restrict applications in soft robotics and tissue engineering where parts are increasingly expected to have compositional and functional heterogeneity. Bone, for instance, consists of multiple domains with distinct composition and microstructure (i.e. compact vs spongy bone), meaning that bioprinting methods for recreating bone must be able to seamlessly vary composition and mechanical properties. Thus, ongoing research is needed to develop new techniques to address performance limitations, specifically in terms of the ability to handle multiple materials without sacrificing print resolution or introducing printing defects.

This first chapter will be focused primarily on how microfluidic technology can be used to enable robust control over multiple material flow streams and thus facilitate multimaterial printing in extrusion-based and inkjet 3D printing. In addition to a broad review of 3D printing and microfluidics, specific case studies will be provided to highlight the role of microfluidics in enabling novel capabilities and material combinations for 3D printing, which thus sets up the detailed discussion of the remaining works in Chapters 2 & 3 of this dissertation.

1.1.2 Common 3D printing technologies

3D printing relies on the coordinated deposition/placement of precursor material into CAD-generated 3D shapes followed by post-processing steps to produce the final printed object. While a range of 3D printing methods have been developed, some methods are more favored due to well-characterized working principles, straightforward instrumentation, low-cost and flexibility in processing different materials. In the following section, we will review the working principles of well-established 3D printing methods for soft polymers, including extrusion printing, inkjet printing and stereolithography, and discuss their limitations that can potentially be addressed using microfluidics.

Extrusion-based 3D printing relies on the controlled layer-by-layer extrusion/dispensing of material onto a build surface or existing layers of material, culminating in a multilayer 3D printed structure. Materials used in extrusion printing are typically viscoelastic inks that are designed for ease of flow during printing and shape retention post-printing, especially. For many research applications, inks are typically composed of polymer precursors (e.g. epoxies, hydrogels) with other materials, whether it be thinning solvents or solid additives, being added to impart the suitable rheology for extrusion, shape retention as well as other chemical or functional properties according to the desired application[17]. The final ink is typically extruded through a nozzle as a continuous filament via pressure applied using different controls such as pneumatic controls, pistons or screw displacement (Fig. 1A), while spatial positioning is defined using a series of programmable servo motors. When constructing multimaterial prints however, defects are easily introduced when using the common approach of sequentially printing one material at a time, with robust and costly control systems needed in order to minimize such defects. A comparatively simple and streamlined approach to handling multiple inks can be found in microfluidics where researchers have demonstrated the ability to manipulate different fluid streams within a single device. For extrusion-based printing, integrating microfluidic elements into a single printhead provides the user on-the-fly control over incoming fluids to customize composition and architecture of the outgoing ink stream, thereby enabling the construction of multimaterial prints with programmable compositional and functional heterogeneity.

Inkjet technology is similar to extrusion printing, except ink is typically dispensed as uniform discrete droplets at high frequencies. It thus represents one of the earliest examples of microfluidics technology in printing. Traditionally used for 2D patterning, inkjet printing employs either a continuous inkjet or droplet-on-demand approach. The former features a column of liquid that subsequently breaks up into droplets via Rayleigh instability, while the latter features an actuator to generate individual droplets pulse-by-pulse at frequencies as high as 60kHz (Fig. 1B). Between the ability to generate picoliter-size droplets and ease of incorporating multiple nozzles within the same inkjet printhead, inkjet printing can easily achieve

multimaterial printing and high spatial resolution (10 μm). However, along with the strict material property requirements for inkjet printing[18], the seemingly paradoxical material requirements of breaking up into discrete droplets while retaining its shape post-printing present a significant hurdle in designing inkjet-based 3D printing process and selecting suitable ink materials. Inks densely loaded with suspended particles typically used in extrusion-based 3D printing are prone to cause clogging in inkjet printheads. Meanwhile, reactive precursors inks that solidify post-printing can be used to achieve layer-by-layer material deposition, but this approach requires a well-controlled sequential deposition of reactants to avoid unwanted reactions. To this end, droplet-based microfluidics may prove especially useful for overcoming or circumventing limitations to inkjet-based 3D printing. Since droplet-based microfluidics has been used extensively to generate and closely manipulate of individual droplets for facilitating microparticle synthesis, the design and working principles associated therewith can be readily translated into a 3D printing application, whether via enhancing traditional inkjet printing capabilities or inspiring novel and emergent droplet-based printing approaches.

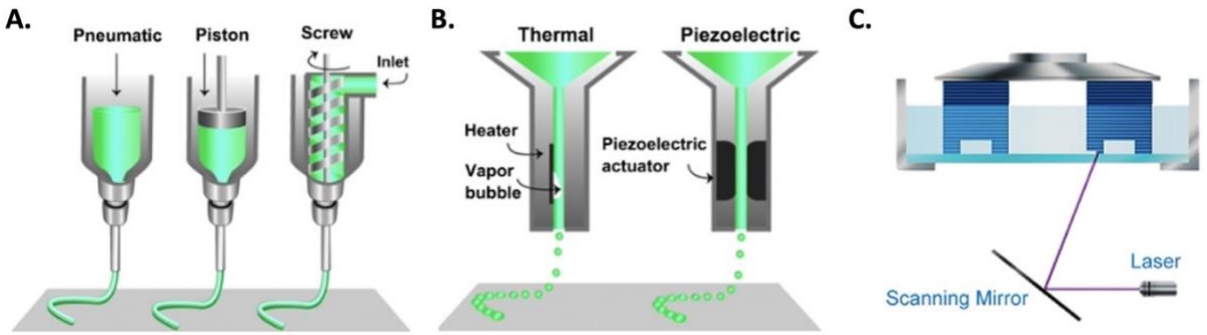

Figure 1. Three well-established 3D printing technologies. (A) Extrusion-based printing, with three different modes of extrusion being illustrated. (B) Inkjet printing, with two different types of droplet-on-demand techniques being shown[5]. Reproduced with permission from Adv. Mater. 25, 36 (2013). Copyright 2013 WILEY-VCH Verlag GmbH \& Co. KGaA, Weinheim. (C) Stereolithography (SLA) printing with a scanning laser-based photopolymerization setup[7]. Reproduced with permission from Chem. Rev. 120, 19 (2020). Copyright 2020 American Chemical Society.

Stereolithography (SLA) is a light-based additive manufacturing technique that relies primarily on the sequential photopolymerization of resins to form 3D objects. Specifically, standard operation of SLA involves a build stage on which photoresin layers are sequentially applied, typically via immersion into a photoresin vat, followed by photopolymerization of the layer. This process is repeated layer after layer to generate a 3D object. Photopolymerization is typically performed either using a scanning laser for line-by-line patterning (Fig. 1C) or digital light processing (DLP) technology in which entire planes/layers are patterned at once. The latter is especially favored for its capacity to dramatically speed up fabrication. At the same time, continuous liquid interface production (CLIP) technology has emerged wherein an oxygen-permeable window is used to create a photopolymerization-inhibitory "dead" zone" adjacent to the printing layer that continuously wets the printing layer, thereby enabling controlled and continuous photopolymerization that further speeds up the SLA printing process[19]. As such, vertical print speeds have increased from several mm/hr in a traditional layer-by-layer scanning laser method to excess of hundreds of mm/hr. A variety of photoresins have been developed for use in a variety SLA 3D printing applications, including optically clear resins and bioresins for use in cellular/tissue engineering applications[6–8]. The development of a multimaterial SLA 3D printing where the composition and functional properties of 3D printed objects are varied across space would require material exchange/switching steps which, due to the vat-based nature of conventional SLA process, can be prohibitively time-consuming and wasteful in terms of material usage. The targeted introduction and manipulation of fluids offered by microfluidics can thus streamline the handling of different materials (i.e. material switching and intermediate washing steps) and thus facilitate a more material-efficient workflow for multimaterial SLA 3D printing than otherwise achievable. Such a discussion can be found elsewhere in the literature and is beyond the scope of this dissertation[20].

1.2 Using Microfluidics to Enhance 3D Printing Capabilities

1.2.1 Introduction to microfluidics

Microfluidic technology, which manipulates fluid flows in miniaturized channels with characteristic lengths of between 1 – 100 μm, has developed contemporaneously with 3D printing. Flows within microchannels are characterized by having low Reynolds numbers, and the relative dominance of viscous and surface forces in microfluidics results in highly predictable transport behavior, enabling a high degree of spatiotemporal control over fluid composition arising from multiple fluid phases[21]. Consequently, decades of research have yielded a large library of microfluidic device design, each specifically tailored to facilitate a different set of fluidic phenomena according to the desired application (e.g. biochemical analysis[22,23], separations[24–26], material synthesis[27–29]). Given the overlapping length scales with 3D printing technology, microfluidics is well poised to interface with and complement 3D printing technology by unlocking independent material handling abilities. For instance, continuous microfluidics offers well-controlled mixing and separation capabilities that can be utilized in 3D printing to homogenize or texturize inks prior to dispensing, enabling programmable ink composition and structure. Similarly, droplet-based microfluidics offers controlled droplet generation and unprecedented multiphase flow capabilities that can augment existing 3D printing methods or even inspire entirely new modes of 3D printing.

1.2.2 Microfluidics for filament-based 3D printing

For most applications, nozzle diameters used for extrusion-based printing are on the order of hundreds of microns, which is on the high end of the length scale used in microfluidics. This overlap in length scale has led researchers to develop applications incorporating both technologies, including the 3D printing of microfluidic devices or, more relevant to our current discussion, microfluidics-enabled printing. The latter generally refers to using microfluidics technology and principles to augment the capabilities of a 3D printing process, whether it be improving print resolution or enabling multimaterial printing. In the following section, the recent literature surrounding the use of microfluidic elements within a single

printhead to continuously handle multiple incoming material streams and tune the final composition of the outgoing ink filament is discussed.

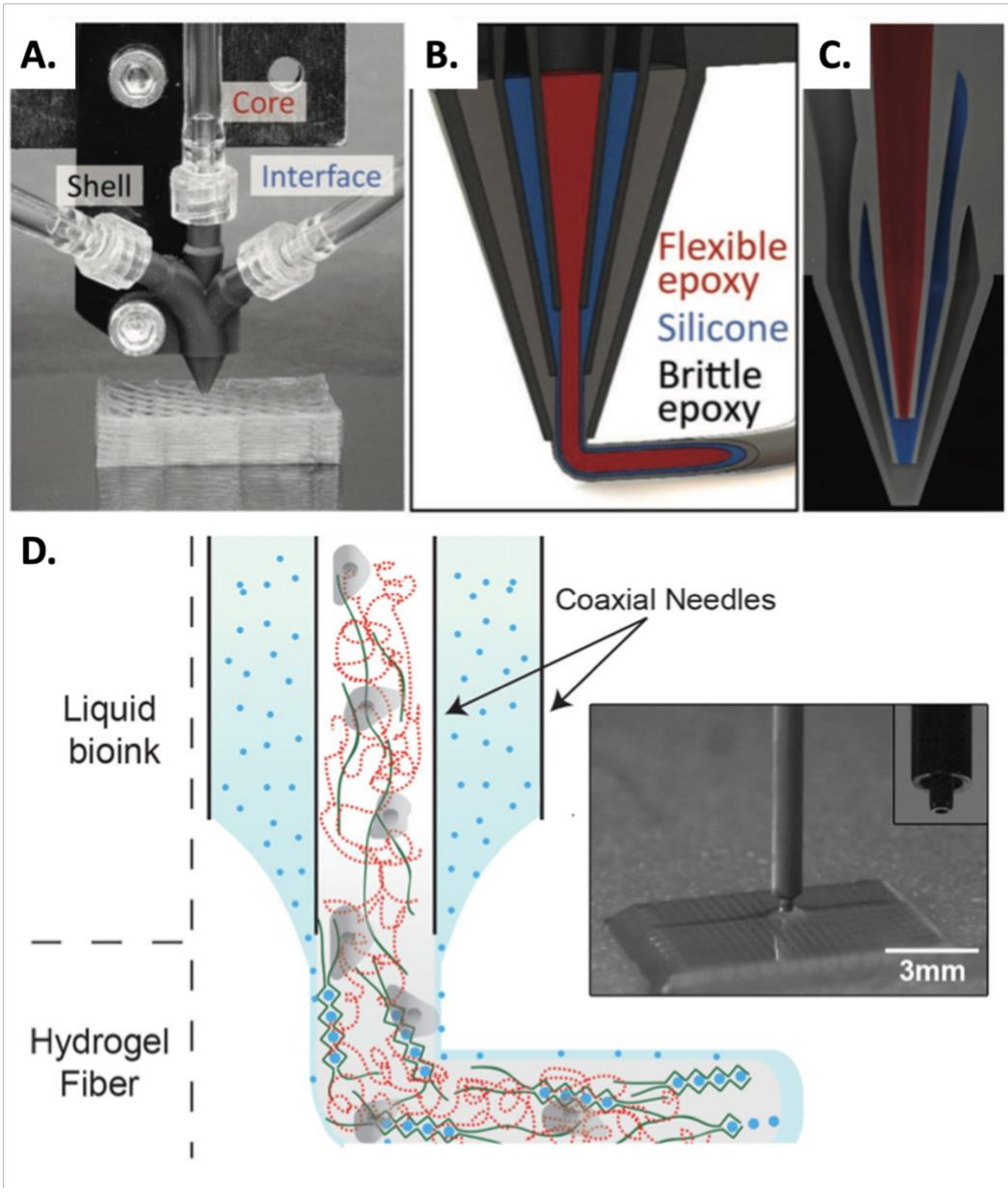

Figure 2. Extrusion printing of core-shell filaments using coaxial nozzles. (A) Extrusion printing of lattice structures using multicore-shell filaments (B) Sectional view multicore-shell filaments (C) Sectional view of the coaxial nozzle[30]. Reproduced with permission from Adv. Mater. 30, 12 (2018). Copyright 2018 WILEY-VCH Verlag GmbH \& Co. KGaA, Weinheim. (D) Bioprinting of alginate bioinks using coaxial streams of alginate pre-gel and crosslinker[31]. Reproduced with permission from Adv. Mater. 28, 4 (2015). Copyright 2015 WILEY-VCH Verlag GmbH \& Co. KGaA, Weinheim.

Co-flowing fluid streams are a common feature in glass capillary microfluidics where capillaries are aligned coaxially to position fluids and facilitate material synthesis of core-shell microparticles[32,33] and microfibers[34]. Similarly, coaxial nozzles represent a simple and effective method for arranging inks into a core-shell morphology for 3D printing wherein a single filament consists of one material encapsulated within another. The list of possible materials for coaxial extrusion can be extensive, limited only according to the desired application and the ability for material phases to remain distinct from one another. Using viscoelastic material with higher storage modulus (G') as the encapsulating layer enables an otherwise unprintable ink core to remain in place post-printing. Lorang et al used a hand-machined metallic coaxial needle to encapsulate an unprintable optical precursor ink core (Ormoclear™) within a fugitive Pluronic F127 sheath. This provided sufficient mechanical support while the core material underwent a 10-minute long UV cure process. The net result was a simple process for direct-writing of optical waveguides[35]. Similarly, Frutiger and colleagues used a series of coaxial glass capillaries housed within a larger device to print flexible multi-layered conductive wires. In this case, the sheaths of viscoelastic PDMS elastomer provide physical encapsulation, mechanical extensibility and electrical insulation to the ionically conductive liquid core[36] , thus enabling its use as a wearable soft robotic sensor.

Moreover, aside from providing direct physical support, the outer encapsulating layer can also work synergistically with the core layer to produce new material combinations with unique or superior properties. For instance, Mueller et al designed coaxial printhead to enable the printing of three-layered epoxy-silicone filaments. The arrangement of a flexible epoxy core followed by a flexible silicone intermediate layer and a brittle epoxy outer layer produced a filament with superior toughness and stiffness, while the recessed-layout of nozzles within a larger housing helps to minimize the final nozzle diameter as the number of ink streams for encapsulation scales up (Fig. 2A-C)[37]. Other examples include coaxial filaments of high-density and low-density polyethylene[38] or carbon-fiber epoxy with syntactic foam[39]. The use of coaxial nozzles for generating core-shell filaments can also be found in electrohydrodynamic printing where inks are extruded into filaments using electric fields instead of pressure-driven flow as is typical for extrusion-based printing.

Using this method, researchers were able to generate core-shell and hollow microfibers[40–45] whose diameters are smaller than that of the nozzles. In Chapter 3, we will introduce and discuss the use of a core-shell hydrogel filament for intestinal epithelial tissue engineering.

In addition to forming a distinct core-shell morphology with clear arrangements of different materials, the coaxial nozzle may be used to facilitate controlled interactions between the different layers of ink. Researchers from the Khademhosseini group developed a microfluidics-enabled process to print gel methacroyl (GelMA)-alginate bioinks. Using a coaxial nozzle, the cell-laden GelMA-alginate blend was encapsulated within a sheath of calcium chloride solution. They hypothesized that ionic crosslinking reaction of alginate would impart sufficient mechanical integrity for the more bioactive GelMA component to retain its shape while undergoing UV crosslinking. The selection of appropriate printing speeds and ink flow rates through the microfluidic printhead enabled the bioprinting of hydrogel filaments with diameters on the order of hundreds of microns, striking a critical balance between uncontrolled ink spread post-deposition due to the low viscosity of the inks and potential nozzle blockage due to the rapid ionic crosslinking reaction of alginate with calcium[31,46] (Fig. 2D). From this base concept or workflow, variations of the same bioprinting process were developed for different applications including that of vascular networks, osteoblasts, muscles and epithelial cells[47–49]. In the Appendix of Chapter 2, we will present some early work that utilizes a similar workflow in tandem with double emulsions. Overall, the coaxial nozzle is a simple and reliable technique utilizing laminar flow for stratifying different ink materials within the extruded filament, directly paralleling the use of co-flowing fluid streams in microfluidic material synthesis. Glass capillary microfluidics, despite the difficulty in device fabrication, facilitates the encapsulation of one material within another and is thus suitable for direct application in 3D printing of core-shell inks. At the same time, the rise of other nonplanar microfluidic devices made using SLA over the past decade[50,51] represents a breakthrough in ease of device design and manufacturing that enable researchers to more rapidly develop novel core-shell and multilayered material arrangements for 3D printing applications.

Another key goal of multimaterial printing is the controllable/programmable deposition of different materials/inks at desired locations along the printing path. For extrusion printing, this could be achieved by switching between multiple nozzles mid-print; however, the process calls for advanced or cumbersome control systems in order to minimize the introduction of defects arising from swapping out nozzles or extrusion start-up from the new nozzle. To realize an extrusion-based multimaterial 3D printing process, much research has been focused on designing a single nozzle that can predictably manipulate incoming material streams beyond simply arranging them into a concentric layout as seen in the coaxial nozzle.

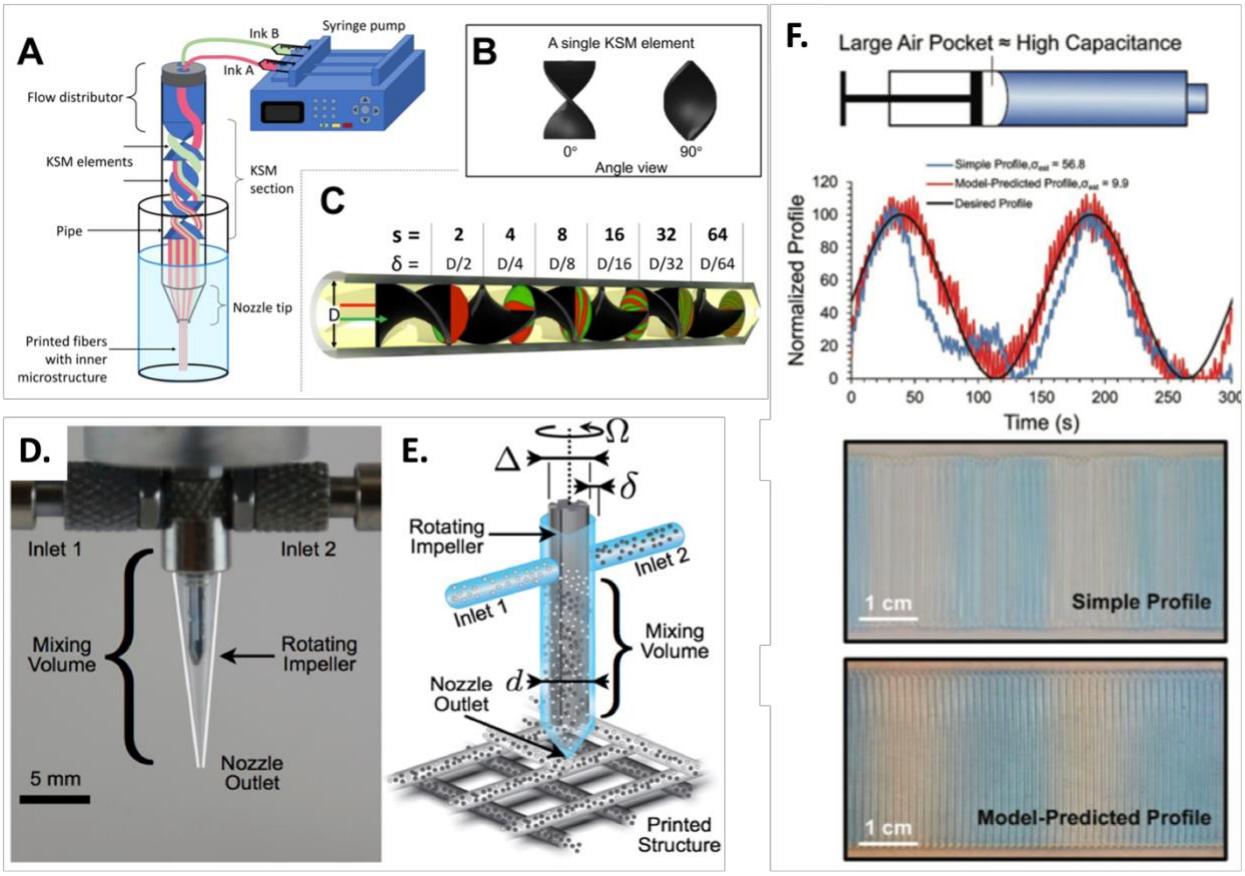

Figure 3. Extrusion printing with integrated microfluidic mixing strategies. (A) Schematic of fibers printed using continuous chaotic bioprinting (B) Images of Kenics static mixer (KSM) elements (C) Modelling fiber microstructure downstream of KSM[52]. Reproduced with permission from Chávez-Madero et al., Biofabrication 21, e00125 (2021); licensed under a Creative Commons Attribution 4.0 License. (D) Active mixing printhead using rotating impeller. (E) Illustration of printing using active mixer printhead[53]. Reproduced with permission from Ober et al., Proc. Natl. Acad. Sci. U.S.A. 112, 40 (2015). Copyright 2015 from National Academy of Science. (F) Microfluidic circuit analogy approach to design precise mixing to match desired profile[54]. Reproduced with permission Adv. Mater. Tech. 4, 1900784 (2019). Copyright 2019 WILEY-VCH Verlag GmbH \& Co. KGaA, Weinheim.

Low Reynolds number flow in microfluidics has prompted researchers to explore different mixing scheme in microfluidics to either exploit slow diffusion-dominant mixing or induce turbulence and speed up the mixing process[55]. The integration of similar passive and active mixing schemes within a 3D printhead was investigated as early as 2015. Passive mixing was achieved via the incorporation of fins and grooves along the internal walls of the printhead. For reasonable ink residence times, this method was shown to be incapable of thoroughly mixing ink components, especially when ink viscosity is high[53]. Furthermore, researchers utilized passive mixing as a method of inducing simple and predictable chaotic flows within microchannels to create complex patterns of ink layers, which was subsequently referred to as 'chaotic printing'[52,56]. This was demonstrated when researchers integrated Kenics static mixer (KSM) elements within a printhead for bioprinting complex micropatterned alginate-based bioink filaments (Fig. 3A-C) [57,58]. Other more modest instances of mixing printing include creating Janus or biphasic filaments, either by means of a microfluidic Y-channel[31,59] or by bundling microcapillaries together[60,61]. Lastly, active mixing via a rapidly spinning impeller within the printhead assembly has been shown to be fully capable of blending and homogenizing incoming inks prior to deposition[53,54,62,63]. This, coupled with programmable control over the incoming flow rates of separate inkstreams, enables real-time control over the composition of deposited inks and opens the possibility of incorporating functional gradients in 3D printed objects (Fig. 3D-F). It is worth noting the utility of computational fluid dynamics (CFD) for modeling-guided experimental design in printhead mixing capabilities[62,64] and even for generating desired micropatterns in 3D printed filaments as in the case of 'chaotic printing't[52,56].

1.2.3 Microfluidics for droplet-based 3D printing

Although inkjet printing is primarily associated with 2D patterns, it has nonetheless inspired the idea of using discrete droplets as the building blocks for 3D printed objects. However, commercial droplet-on-demand inkjet has limitations for ink surface and rheological properties in order to facilitate droplet generation, which thereby restricts the range of usable 3D printing inks. With the emergence of droplet-

based microfluidics for material synthesis applications (e.g. liposomes, polymersomes, microparticles), researchers in 3D printing can draw from an additional pool of literature and resources to design new droplet-based 3D printing strategies and applications.

Inkjet-based methods for metal additive manufacturing has been a major research focus over the past couple of decades as it represents a desirable simplification from the other metal additive manufacturing techniques that rely on capital-intensive and complex post-processing steps (e.g. sintering, laser annealing etc.). Outside of low-temperature metals such as lead, tin and solder, however, standard inkjet equipment is unsuitable for droplet-on-demand dispensing of metal due to the extreme temperatures involved[65]. To circumvent this, researchers resorted to modifying the piezoelectric actuators to ensure the actuators do not heat up past the Curie temperature at which all piezoelectric properties are lost. At the same time, researchers have proposed a number of novel actuation techniques featuring pressure-pulses[66–68] and Lorentz forces[69,70] to induce Rayleigh-Plateau instabilities that lead to droplet breakoff. Besides the physics of droplet breakup, droplet-based microfluidics also offers insights into using electrochemical reactions to synthesize metallic nanoparticles[71,72]. Correspondingly, other droplet-on-demand techniques were developed for metal printing that sidesteps the need for elevated temperatures altogether. In one approach, researchers used electrohydrodynamics to launch metal nanoparticles suspended in volatile solvent in order to print single micron diameter 3D metallic structures, similar to electrospraying[73]. Elsewhere, researchers used a redox approach wherein electrodes are oxidized in a reservoir of electrolytes prior to being launched as droplets of solvated metal ions via electrohydrodynamic forces through a glass microcapillary towards a substrate where the ions finally are reduced back into a metal to produce sub-micron metallic 3D features (Fig. 4A)[74]. Further developments in microfluidics-enabled metal droplet-on-demand printing can be geared towards using reduction reactions of metal precursors as a basis for 3D printing metallic structures.

As a means of creating 3D self-standing printed structures, researchers have resorted to using highly reactive precursors that can undergo rapid gelation/polymerization upon deposition and thereby retain

sufficient mechanical integrity during printing. In this regard, photopolymers are favored since they can undergo photopolymerization mid-flight prior to contact with the substrate[75,76]. However, when working with two or more highly reactive chemical components, it becomes exceedingly difficult to prevent unwanted or premature ink reactions without robust control systems in place[77,78]. To overcome this, Visser and colleagues first described a setup reminiscent of continuous inkjet where one actuated nozzle was used to launch a droplet train that subsequently collided with a liquid jet launched from another nozzle[79]. With this setup, spherical core-shell alginate particles were formed that could stack on top of one another to bioprint 3D tissue constructs. Following this, other researchers used a similar setup to handle and 3D print other reactive species, including PEDOT:PSS/ionic liquid[80], polyaniline[81] and silicones[82]. The design space afforded by this setup is wide, allowing for adjustments to print resolution and even printed ink rheology based on the reaction kinetics and other printing parameters (e.g. droplet ejection frequency, droplet trajectories and velocity). With appropriate choice of these parameters, researchers reported freeform printing of 3D shapes without the need for supporting materials[82]. Droplets generated from this "in-air" collision approach could be either homogeneous or heterogeneous, the latter being used to 3D print structures with tunable degrees of microporosity[75,76].

Dispersing droplets into a medium other than air presents the possibility of using interfacial forces to assist in droplet stabilization and assembly. Hagan Bayley's group has pioneered the use of a droplet-on-demand technique to 3D print lipid-stabilized droplet networks. Specifically, individual aqueous droplets are dispensed using a piezoelectric actuator and suspended within an oil bath where they are stabilized by lipid molecules at the liquid-liquid interface[83,84]. As each droplet sinks into the bottom of the oil bath, they maintain their roughly spherical shape and adhere to neighboring drops by forming a droplet lipid bilayers (DIB). The researchers subsequently used their droplet-on-demand process of lipid-coated hydrogel droplets in an oil bath for bioprinting high-resolution cellular/tissue constructs, reporting cell viabilities that are higher than those found in extrusion bioprinters while approaching the resolution of inkjet printers (10 μm droplet diameters) (Fig. 4B)[85–87]. The presence of DIB in these droplet networks demonstrated to

stabilize the network, thus overcoming the traditional difficulty associated with handling ECM materials that are otherwise unprintable due to lack of mechanical integrity. Consequently, researchers were able to use this droplet approach to print cartilage, neural and intestinal tissues[88–90] with prepatterned arrangements of cells. In addition, by incorporating functional particles and proteins into specific droplets within the network, researchers design complex synthetic tissues with internal functional compartments (e.g. ion conductivity) that allow for cross communication within the droplet network, as well as externally responsive compartments (e.g. magnetic sensitivity)[91,92].

In addition to using fluids, researchers have also utilized yield-stress fluid baths to suspend droplets in space as part of a strategy for organizing droplets into 3D geometries, a technique known as embedded printing. Unlike an oil-based mediums, yield-stress fluids used in embedding printing allow the deposited ink to remain fixed in place while simultaneously filling up the void spaces left behind by the travelling nozzle used to deposit the ink. While embedded printing is typically used for freeform printing of continuous ink patterns[12,93], the suspension of individual droplets within a quiescent bath has several benefits. For instance, the yield-stress baths are useful for handling and supporting materials that are otherwise unprintable in-air. Using a constant ink flow rate and nozzle travel speed, researchers successfully embedded high surface tension eGaIn droplets with consistent diameters and spacings within a Carbopol bath and organized into distinct 3D structures[94]. Moreover, the quiescent conditions afforded by the yield-stress bath and the precise control of droplet volumes are conducive for facilitating sensitive reactions and processes such as crystallization of active pharmaceutical ingredients in an advection-free environment[95,96].

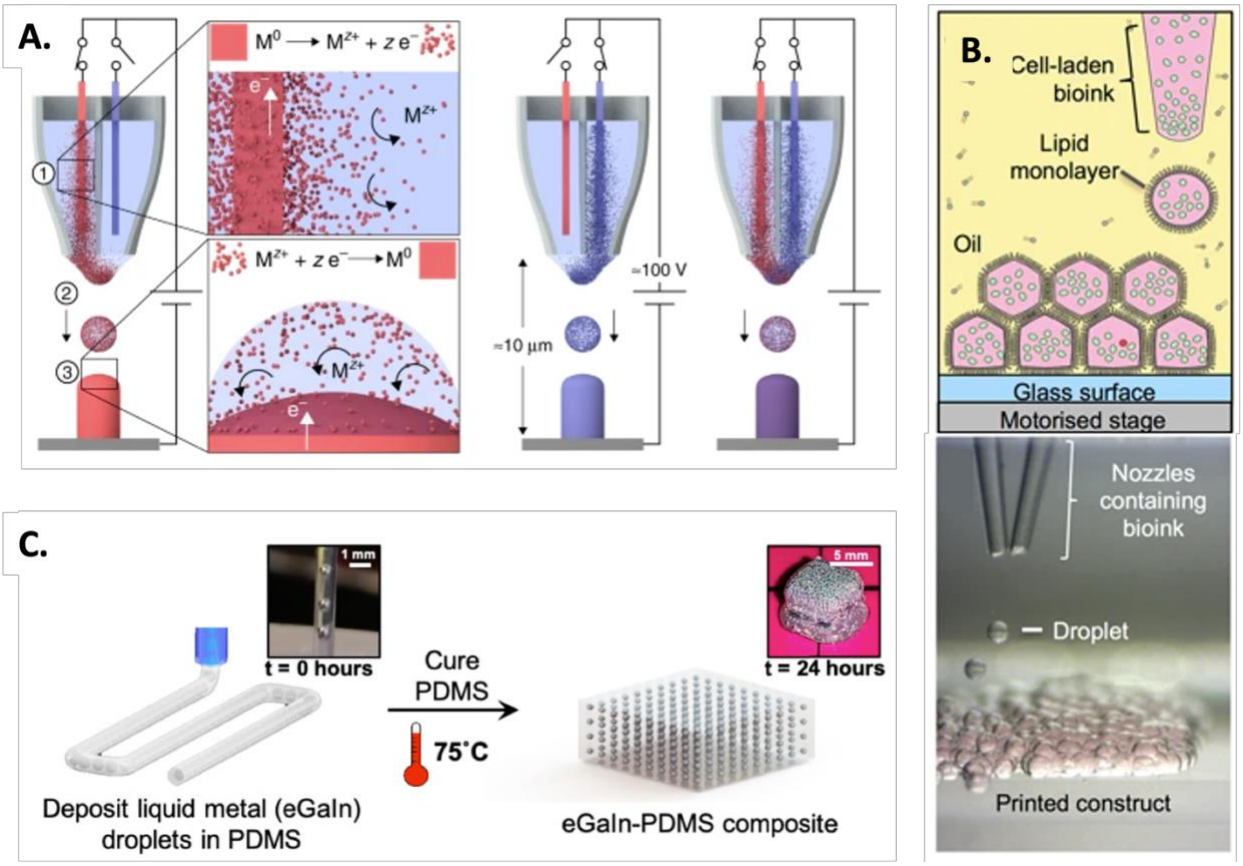

Figure 4. Droplet-based 3D printing. (A) Electrohydrodynamic droplet generation and subsequent redox of ionic solution for 3D printing metal microstructures[74]. Reproduced from Reiser et al., Nat. Comm. 10, 1853 (2019); licensed under a Creative Commons Attribution 4.0 International License. (B) Droplet network stabilized by droplet interface bilayers (DIB) and bioprinted into a tissue construct[85]. Reproduced from Graham et al., Sci. Rep. 7. 7004 (2017); licensed under a Creative Commons Attribution 4.0 International License. (C) 3D printing of liquid metal droplets in PDMS filaments[97]. Reproduced with permission from Proc Natl. Acad. Sci. 117, 26 (2020). Copyright 2020 National Academy of Sciences.

Aside from using individual droplets as building blocks, the encapsulating phase itself may be used to form continuous ink filaments containing discrete droplets, similar to the core-shell morphology of filament-based printing except with discretized cores. While the physics associated with droplet generation through multiphase flows, the hallmark of droplet-based microfluidics, has been extensively reviewed elsewhere, its use for 3D printing has remained largely unexplored. Using traditional droplet-based microfluidic devices, researchers reported the simultaneous generation and 3D printing of droplet core-shell inks. As the multiphase inks are deposited layer-by-layer into a 3D structure, the encapsulated droplets are held in place within the continuous phase, much like in embedded printing (Fig. 4C). Through the careful selection of

different ink materials and proportions for the droplet and continuous phases, researchers could modify and tailor bulk properties (e.g. mechanical stiffness, optical properties, appearance, thermal responsiveness and magnetism) as well as intrinsic properties (e.g. crosslinking density, self-healing)[97,98]. Thus, this direct adaptation of droplet microfluidics represents a multimaterial 3D printing strategy that can be adapted for almost any conceivable application, including soft robotics as discussed in Chapter 2. In addition to the impact of ink materials, we had previously noted how selective packing of droplets within the viscoelastic encapsulating phase due to both the droplet generation and printing processes results in highly textured inks with significant mechanical anisotropy depending on the printing path[97]. What remains to be seen, however, is the extent to which droplets within the encapsulating phase (i.e. multiple emulsions) could be reliably manipulated, redistributed and reorganized using advective forces from multiphase flows, which would enable the facile tuning the bulk functional properties of 3D printed objects.

1.3 Conclusion & Outlook

Laminar flow within microfluidics enables precise control capabilities over incoming material streams, whether it be organizing material into specific textures/patterns (e.g. core-shell, Janus) or homogenizing or seamless ink swapping. Thus, microfluidics in filament-based printing is conducive for the continuous generation of filaments for 3D printing and exerting on-the-fly control over their microstructure. Similarly, droplet-based microfluidics offers valuable insight into the production and manipulation of individual micro-sized droplets as well as the handling of multiphase flows. Such insight can be translated into a variety of 3D printing applications to overcome existing limitations, as in the case of inkjet printing, as well as developing new modes of 3D printing where individual droplets are used as the building blocks. Finally, the precise and controlled manipulation of small volumes of fluids in microfluidics enables streamlined switching and exchanging of photoresin materials, thus facilitating SLA multimaterial 3D printing. There remains many opportunities in this emerging area to explore how microfluidic devices and elements can be directly integrated or adapted for 3D printing applications, and Chapters 2 & 3 of this dissertation will

discuss in greater detail our efforts/contributions to this field with a view towards applications in soft robotics and tissue engineering.

1.4 References:

1. Mohamed, O. A., Masood, S. H. & Bhowmik, J. L. Optimization of fused deposition modeling process parameters: a review of current research and future prospects. *Adv. Manuf.* **3**, 42–53 (2015).
2. Penumakala, P. K., Santo, J. & Thomas, A. A critical review on the fused deposition modeling of thermoplastic polymer composites. *Compos. Part B Eng.* 108336 (2020).
3. Wang, X. C. *et al.* Direct selective laser sintering of hard metal powders: experimental study and simulation. *Int. J. Adv. Manuf. Technol.* **19**, 351–357 (2002).
4. Olakanmi, E. O., Cochrane, R. F. & Dalgarno, K. W. A review on selective laser sintering/melting (SLS/SLM) of aluminium alloy powders: Processing, microstructure, and properties. *Prog. Mater. Sci.* **74**, 401–477 (2015).
5. Malda, J. *et al.* 25th anniversary article: engineering hydrogels for biofabrication. *Adv. Mater.* **25**, 5011–5028 (2013).
6. Li, J., Wu, C., Chu, P. K. & Gelinsky, M. 3D printing of hydrogels: Rational design strategies and emerging biomedical applications. *Mater. Sci. Eng. R Reports* **140**, 100543 (2020).
7. Lee, M., Rizzo, R., Surman, F. & Zenobi-Wong, M. Guiding lights: tissue bioprinting using photoactivated materials. *Chem. Rev.* **120**, 10950–11027 (2020).
8. Yu, C. *et al.* Photopolymerizable biomaterials and light-based 3D printing strategies for biomedical applications. *Chem. Rev.* **120**, 10695–10743 (2020).
9. Zhou, L.-Y., Fu, J. & He, Y. A review of 3D printing technologies for soft polymer materials. *Adv. Funct. Mater.* **30**, 2000187 (2020).
10. Rayna, T. & Striukova, L. Assessing the effect of 3D printing technologies on entrepreneurship: An exploratory study. *Technol. Forecast. Soc. Change* **164**, 120483 (2021).
11. Wallin, T. J., Pikul, J. & Shepherd, R. F. 3D printing of soft robotic systems. *Nat. Rev. Mater.* **3**, 84–100 (2018).
12. Muth, J. T. *et al.* Embedded 3D printing of strain sensors within highly stretchable elastomers. *Adv. Mater.* **26**, 6307–6312 (2014).
13. Lind, J. U. *et al.* Instrumented cardiac microphysiological devices via multimaterial three-dimensional printing. *Nat. Mater.* **16**, 303–308 (2017).
14. Mishra, A. K. *et al.* Autonomic perspiration in 3D-printed hydrogel actuators. *Sci. Robot.* **5**, 1–10 (2020).
15. Richard, C., Neild, A. & Cadarso, V. J. The emerging role of microfluidics in multi-material 3D bioprinting. *Lab Chip* **20**, 2044–2056 (2020).
16. Wang, J., Shao, C., Wang, Y., Sun, L. & Zhao, Y. Microfluidics for medical additive manufacturing. *Engineering* **6**, 1244–1257 (2020).

17. Lewis, J. A. Direct ink writing of 3D functional materials. *Adv. Funct. Mater.* **16**, 2193–2204 (2006).
18. Derby, B. Inkjet printing of functional and structural materials: fluid property requirements, feature stability, and resolution. *Annu. Rev. Mater. Res.* **40**, 395–414 (2010).
19. Tumbleston, J. R. *et al.* Continuous liquid interface production of 3D objects. *Science (80-.).* **347**, 1349–1352 (2015).
20. Mea, H. & Wan, J. Microfluidics-enabled functional 3D printing. *Biomicrofluidics* **16**, 21501 (2022).
21. Shang, L., Cheng, Y. & Zhao, Y. Emerging droplet microfluidics. *Chem. Rev.* **117**, 7964–8040 (2017).
22. Zhu, Y. & Fang, Q. Analytical detection techniques for droplet microfluidics—A review. *Anal. Chim. Acta* **787**, 24–35 (2013).
23. Zenhausern, R., Chen, C.-H. & Yoon, J.-Y. Microfluidic sample preparation for respiratory virus detection: A review. *Biomicrofluidics* **15**, 11503 (2021).
24. Pamme, N. Continuous flow separations in microfluidic devices. *Lab Chip* **7**, 1644–1659 (2007).
25. Sajeesh, P. & Sen, A. K. Particle separation and sorting in microfluidic devices: a review. *Microfluid. Nanofluidics* **17**, 1–52 (2014).
26. Chang, Y., Chen, X., Zhou, Y. & Wan, J. Deformation-based droplet separation in microfluidics. *Ind. \& Eng. Chem. Res.* **59**, 3916–3921 (2019).
27. Günther, A. & Jensen, K. F. Multiphase microfluidics: from flow characteristics to chemical and materials synthesis. *Lab Chip* **6**, 1487–1503 (2006).
28. Marre, S. & Jensen, K. F. Synthesis of micro and nanostructures in microfluidic systems. *Chem. Soc. Rev.* **39**, 1183–1202 (2010).
29. Campbell, Z. S., Bateni, F., Volk, A. A., Abdel-Latif, K. & Abolhasani, M. Microfluidic synthesis of semiconductor materials: toward accelerated materials development in flow. *Part. \& Part. Syst. Charact.* **37**, 2000256 (2020).
30. Mueller, J., Raney, J. R., Shea, K. & Lewis, J. A. Architected lattices with high stiffness and toughness via multicore--shell 3d printing. *Adv. Mater.* **30**, 1705001 (2018).
31. Colosi, C. *et al.* Microfluidic bioprinting of heterogeneous 3D tissue constructs using low-viscosity bioink. *Adv. Mater.* **28**, 677–684 (2016).
32. Utada, A. S. *et al.* Monodisperse double emulsions generated from a microcapillary device. *Science (80-.).* **308**, 537–541 (2005).
33. Chen, H. *et al.* Reactions in double emulsions by flow-controlled coalescence of encapsulated drops. *Lab Chip* **11**, 2312–2315 (2011).
34. Jun, Y., Kang, E., Chae, S. & Lee, S.-H. Microfluidic spinning of micro-and nano-scale fibers for tissue engineering. *Lab Chip* **14**, 2145–2160 (2014).
35. Lorang, D. J. *et al.* Photocurable liquid core--fugitive shell printing of optical waveguides. *Adv. Mater.* **23**, 5055–5058 (2011).
36. Frutiger, A. *et al.* Capacitive soft strain sensors via multicore--shell fiber printing. *Adv. Mater.* **27**, 2440–2446 (2015).

37. Mueller, J., Raney, J. R., Shea, K. & Lewis, J. A. Architected Lattices with High Stiffness and Toughness via Multicore–Shell 3D Printing. *Adv. Mater.* **30**, 1–8 (2018).
38. Peng, F. *et al.* 3D printing with core--shell filaments containing high or low density polyethylene shells. *ACS Appl. Polym. Mater.* **1**, 275–285 (2019).
39. Pack, R. C. *et al.* Carbon Fiber and Syntactic Foam Hybrid Materials via Core--Shell Material Extrusion Additive Manufacturing. *Adv. Mater. Technol.* **5**, 2000731 (2020).
40. Liang, H., He, J., Chang, J., Zhang, B. & Li, D. Coaxial nozzle-assisted electrohydrodynamic printing for microscale 3D cell-laden constructs. *Int. J. bioprinting* **4**, (2018).
41. Wang, B., Chen, X., Ahmad, Z., Huang, J. & Chang, M.-W. 3D electrohydrodynamic printing of highly aligned dual-core graphene composite matrices. *Carbon N. Y.* **153**, 285–297 (2019).
42. Wang, B., Chen, X., Ahmad, Z., Huang, J. & Chang, M.-W. Engineering On-Demand Magnetic Core--Shell Composite Wound Dressing Matrices via Electrohydrodynamic Micro-Scale Printing. *Adv. Eng. Mater.* **21**, 1900699 (2019).
43. Yao, Z.-C., Wang, J.-C., Ahmad, Z., Li, J.-S. & Chang, M.-W. Fabrication of patterned three-dimensional micron scaled core-sheath architectures for drug patches. *Mater. Sci. Eng. C* **97**, 776–783 (2019).
44. Zhu, L.-F., Chen, X., Ahmad, Z., Peng, Y. & Chang, M.-W. A core--shell multi-drug platform to improve gastrointestinal tract microbial health using 3D printing. *Biofabrication* **12**, 25026 (2020).
45. Wang, D. *et al.* Numerical modeling and analysis of coaxial electrohydrodynamic jet printing. *Sci. Rep.* **12**, 1–17 (2022).
46. Liu, W. *et al.* Coaxial extrusion bioprinting of 3D microfibrous constructs with cell-favorable gelatin methacryloyl microenvironments. *Biofabrication* **10**, 24102 (2018).
47. Zhang, Y. S. *et al.* Bioprinting 3D microfibrous scaffolds for engineering endothelialized myocardium and heart-on-a-chip. *Biomaterials* **110**, 45–59 (2016).
48. Zhu, K. *et al.* Gold nanocomposite bioink for printing 3D cardiac constructs. *Adv. Funct. Mater.* **27**, 1605352 (2017).
49. Pi, Q. *et al.* Digitally tunable microfluidic bioprinting of multilayered cannular tissues. *Adv. Mater.* **30**, 1706913 (2018).
50. Männel, M. J., Selzer, L., Bernhardt, R. & Thiele, J. Optimizing Process Parameters in Commercial Micro-Stereolithography for Forming Emulsions and Polymer Microparticles in Nonplanar Microfluidic Devices. *Adv. Mater. Technol.* **4**, 1800408 (2019).
51. Männel, M. J., Baysak, E. & Thiele, J. Fabrication of microfluidic devices for emulsion formation by microstereolithography. *Molecules* **26**, 2817 (2021).
52. Chávez-Madero, C. *et al.* Using chaotic advection for facile high-throughput fabrication of ordered multilayer micro-and nanostructures: continuous chaotic printing. *Biofabrication* **12**, 35023 (2020).
53. Ober, T. J., Foresti, D. & Lewis, J. A. Active mixing of complex fluids at the microscale. *Proc. Natl. Acad. Sci.* **112**, 12293–12298 (2015).
54. Nguyen, D. T. *et al.* 3D printing of compositional gradients using the microfluidic circuit analogy. *Adv.*

Mater. Technol. **4**, 1900784 (2019).

55. Lee, C.-Y., Chang, C.-L., Wang, Y.-N. & Fu, L.-M. Microfluidic mixing: a review. *Int. J. Mol. Sci.* **12**, 3263–3287 (2011).
56. Trujillo-de Santiago, G. *et al.* Chaotic printing: using chaos to fabricate densely packed micro-and nanostructures at high resolution and speed. *Mater. Horizons* **5**, 813–822 (2018).
57. Bol\'\ivar-Monsalve, E. J. *et al.* Continuous chaotic bioprinting of skeletal muscle-like constructs. *Bioprinting* **21**, e00125 (2021).
58. Ceballos-González, C. F. *et al.* High-Throughput and Continuous Chaotic Bioprinting of Spatially Controlled Bacterial Microcosms. *ACS Biomater. Sci. \& Eng.* (2021).
59. Yao, Z.-C. *et al.* A novel approach for tailored medicines: Direct writing of Janus fibers. *J. Drug Deliv. Sci. Technol.* **50**, 372–379 (2019).
60. Liu, W. *et al.* Rapid continuous multimaterial extrusion bioprinting. *Adv. Mater.* **29**, 1604630 (2017).
61. Moon, S. *et al.* 3D jet writing of mechanically actuated tandem scaffolds. *Sci. Adv.* **7**, eabf5289 (2021).
62. Ortega, J. M. *et al.* Active mixing of disparate inks for multimaterial 3D printing. *Adv. Mater. Technol.* **4**, 1800717 (2019).
63. Pelz, J. S., Ku, N., Shoulders, W. T., Meyers, M. A. & Vargas-Gonzales, L. R. Multi-material additive manufacturing of functionally graded carbide ceramics via active, in-line mixing. *Addit. Manuf.* **37**, 101647 (2021).
64. Enders, A., Siller, I. G., Urmann, K., Hoffmann, M. R. & Bahnemann, J. 3D printed microfluidic mixers—a comparative study on mixing unit performances. *Small* **15**, 1804326 (2019).
65. Meda, M., Mehta, P., Mahajan, C., Kahn, B. & Cormier, D. Magnetohydrodynamic liquid metal droplet jetting of highly conductive electronic traces. *Flex. Print. Electron.* **6**, 35002 (2021).
66. Jiang, X.-S., Qi, L.-H., Luo, J., Huang, H. & Zhou, J.-M. Research on accurate droplet generation for micro-droplet deposition manufacture. *Int. J. Adv. Manuf. Technol.* **49**, 535–541 (2010).
67. Luo, J., Qi, L., Tao, Y., Ma, Q. & Visser, C. W. Impact-driven ejection of micro metal droplets on-demand. *Int. J. Mach. Tools Manuf.* **106**, 67–74 (2016).
68. Yi, H., Qi, L., Luo, J., Zhang, D. & Li, N. Direct fabrication of metal tubes with high-quality inner surfaces via droplet deposition over soluble cores. *J. Mater. Process. Technol.* **264**, 145–154 (2019).
69. Luo, Z., Wang, X., Wang, L., Sun, D. & Li, Z. Drop-on-demand electromagnetic printing of metallic droplets. *Mater. Lett.* **188**, 184–187 (2017).
70. Ansell, T. Y. Current status of liquid metal printing. *J. Manuf. Mater. Process.* **5**, 31 (2021).
71. Lazarus, L. L. *et al.* Two-phase microfluidic droplet flows of ionic liquids for the synthesis of gold and silver nanoparticles. *ACS Appl. Mater. \& interfaces* **4**, 3077–3083 (2012).
72. Zhang, L. *et al.* Continuous and scalable production of well-controlled noble-metal nanocrystals in milliliter-sized droplet reactors. *Nano Lett.* **14**, 6626–6631 (2014).
73. An, B. W. *et al.* High-resolution printing of 3D structures using an electrohydrodynamic inkjet with multiple functional inks. *Adv. Mater.* **27**, 4322–4328 (2015).

74. Reiser, A. *et al.* Multi-metal electrohydrodynamic redox 3D printing at the submicron scale. *Nat. Commun.* **10**, 1–8 (2019).
75. Visser, C. W., Amato, D. N., Mueller, J. & Lewis, J. A. Architected polymer foams via direct bubble writing. *Adv. Mater.* **31**, 1904668 (2019).
76. Amato, D. N. *et al.* Programmable porous polymers via direct bubble writing with surfactant-free inks. *ACS Appl. Mater. \& interfaces* **12**, 42048–42055 (2020).
77. Sturgess, C., Tuck, C. J., Ashcroft, I. A. & Wildman, R. D. 3D reactive inkjet printing of polydimethylsiloxane. *J. Mater. Chem. C* **5**, 9733–9743 (2017).
78. Schuster, F., Hirth, T. & Weber, A. Reactive inkjet printing of polyethylene glycol and isocyanate based inks to create porous polyurethane structures. *J. Appl. Polym. Sci.* **136**, 46977 (2019).
79. Visser, C. W., Kamperman, T., Karbaat, L. P., Lohse, D. & Karperien, M. In-air microfluidics enables rapid fabrication of emulsions, suspensions, and 3D modular (bio) materials. *Sci. Adv.* **4**, eaao1175 (2018).
80. Teo, M. Y. *et al.* Direct patterning of highly conductive PEDOT: PSS/ionic liquid hydrogel via microreactive inkjet printing. *ACS Appl. Mater. \& interfaces* **11**, 37069–37076 (2019).
81. Teo, M. Y. *et al.* The in situ synthesis of conductive polyaniline patterns using micro-reactive inkjet printing. *J. Mater. Chem. C* **7**, 2219–2224 (2019).
82. Śliwiak, M., Bui, R., Brook, M. A. & Selvaganapathy, P. R. 3D Printing of Highly Reactive Silicones Using Inkjet Type Droplet Ejection and Free Space Droplet Merging and Reaction. *Addit. Manuf.* 102099 (2021).
83. Villar, G., Heron, A. J. & Bayley, H. Formation of droplet networks that function in aqueous environments. *Nat. Nanotechnol.* **6**, 803–808 (2011).
84. Villar, G., Graham, A. D. & Bayley, H. A tissue-like printed material. *Science (80-.).* **340**, 48–52 (2013).
85. Graham, A. D. *et al.* High-resolution patterned cellular constructs by droplet-based 3D printing. *Sci. Rep.* **7**, 1–11 (2017).
86. Ma, S., Mukherjee, N., Mikhailova, E. & Bayley, H. Gel microrods for 3D tissue printing. *Adv. Biosyst.* **1**, 1700075 (2017).
87. Kumar, R. K. *et al.* Droplet printing reveals the importance of micron-scale structure for bacterial ecology. *Nat. Commun.* **12**, 1–12 (2021).
88. Zhou, L. *et al.* Lipid-bilayer-supported 3D printing of human cerebral cortex cells reveals developmental interactions. *Adv. Mater.* **32**, 2002183 (2020).
89. Alcinesio, A. *et al.* Controlled packing and single-droplet resolution of 3D-printed functional synthetic tissues. *Nat. Commun.* **11**, 1–13 (2020).
90. Zhou, L. *et al.* Bioengineered Gastrointestinal Tissues with Fibroblast-Induced Shapes. *Adv. Funct. Mater.* **31**, 2007514 (2021).
91. Downs, F. G. *et al.* Multi-responsive hydrogel structures from patterned droplet networks. *Nat. Chem.* **12**, 363–371 (2020).
92. Alcinesio, A. *et al.* Modular Synthetic Tissues from 3D-Printed Building Blocks. *Adv. Funct. Mater.* 2107773 (2021).

93. Zhao, J. & He, N. A mini-review of embedded 3D printing: supporting media and strategies. *J. Mater. Chem. B* **8**, 10474–10486 (2020).
94. Yu, Y., Liu, F., Zhang, R. & Liu, J. Suspension 3D Printing of Liquid Metal into Self-Healing Hydrogel. *Adv. Mater. Technol.* **2**, 1700173 (2017).
95. Nelson, A. Z., Kundukad, B., Wong, W. K., Khan, S. A. & Doyle, P. S. Embedded droplet printing in yield-stress fluids. *Proc. Natl. Acad. Sci.* **117**, 5671–5679 (2020).
96. Nelson, A. Z., Xie, J., Khan, S. A. & Doyle, P. S. Continuous Embedded Droplet Printing in Yield-Stress Fluids for Pharmaceutical Drug Particle Synthesis. *Adv. Mater. Technol.* **6**, 2001245 (2021).
97. Mea, H. J., Delgadillo, L. & Wan, J. On-demand modulation of 3D-printed elastomers using programmable droplet inclusions. *Proc. Natl. Acad. Sci.* **117**, 14790–14797 (2020).
98. Li, X. *et al.* Multimaterial microfluidic 3D printing of textured composites with liquid inclusions. *Adv. Sci.* **6**, 1800730 (2019).

CHAPTER 2: ON-DEMAND MODULATION OF 3D PRINTED ELASTOMERS USING DROPLET INCLUSIONS

2.1 Introduction

Additive manufacturing has evolved into a mainstream technology that is increasingly competitive to traditional manufacturing processes in terms of costs and process capabilities. Among the additive manufacturing technologies that have been developed, extrusion-based 3D printing (e.g. fused deposition modelling and direct ink writing) is highly popular due to its relative affordability and versatility in terms of suitable materials[1,2]. In terms of performance, industrial extrusion-based 3D printers, such as those developed by nScrypt, are capable of high precision layer by layer deposition of multiple inks with to generate high resolution compositionally-graded 3D constructs[3–6].

Despite such capabilities, the production of fully-printed functionally heterogeneous objects without resorting to a multistep assembly process remains an ongoing challenge. Some common approaches include sequential printing of different ink materials through multiple nozzles or blending ink materials at different proportions prior to extrusion[7,8]. Augmenting this material blending approach using microfluidic mixing, researchers were able to seamlessly exchange[9], homogenize[10,11] or texturize[12,13] ink blends at the point of printing. While these advances have demonstrated the printing of textured and heterogeneous constructs, the use of microfluidic mixers for extrusion printing has only been demonstrated in blends of miscible inks (e.g. silicone/silicone pastes, calcium/alginate aqueous solutions) and other solid additives (e.g. quantum dots and fumed silica). The application of microfluidics for multiphase or immiscible ink blends (i.e. emulsions) in a 3D printing context remains largely unexplored.

To generate heterogeneous prints, one of the current approaches is to selectively tune the microstructural properties of extruded inks in real-time. Using rotating photomasks and magnetic field sources, researchers were able to manipulate the alignment of magnetic nanoparticle fillers in a photocurable ink, creating a structure with a spatially graded microstructures and functional properties[14–16]. Elsewhere, a rotating

printhead was used to spatially control the orientation of short fibers in epoxy-fiber inks and to produce engineered composites[17]. The multi-dimensional printing strategy, despite its robust control capabilities, strictly requires that fillers have high aspect ratios and are capable of responding to the stimuli provided (i.e. the applied B-field and the rotational shear)[18] . Thus, there still exists a need for a generalizable strategy towards generating heterogeneous prints in an extrusion-based printing context.

Here we report the in-situ modulation of printed construct properties using controlled dispersion of droplet inclusions. By introducing immiscible inks in a glass capillary microfluidic device, we simultaneously generated and 3D printed highly textured emulsion inks consisting of well-organized droplets. We characterized the mechanical contribution of various droplet inclusions in printed polydimethylsiloxane (PDMS) constructs and in the process demonstrate the novel use of aqueous poly(ethylene glycol) diacrylate (PEGDA) droplets to chemically modify and intrinsically soften the surrounding PDMS phase. Finally, we designed and printed a primitive soft robotic actuator consisting of spatially defined mechanically compliant and magnetically-responsive domains capable of instantaneous bending at desired locations in response to an external B-field. Demonstrating the ability to impart functional properties at selective points across the printed construct, we anticipate the potential of our droplet-based strategy for next-generation rapid prototyping of heterogeneous and time-evolving structures.

2.2 Methods and Materials

2.2.1. PDMS ink design

The PDMS outer phase was designed specifically to enable shearing of inner phase droplets and retention of shape post-printing. 11 parts Dow Corning SE1700 was mixed with 9 parts silicone oil (20 cSt) containing 13 wt.% Dow Corning 749 fluid as a surfactant. For optimal mixing, the SE1700 elastomeric base and silicone oil were homogenized by hand prior to adding the SE1700 curing agent. Upon addition of the curing agent and subsequent mixing, the PDMS ink had a final appearance of a light grey opaque paste and a shelf life of 24 hours.

2.2.2 Microfluidic Printhead Design

A generic glass capillary microfluidic device made from borosilicate glass capillary tubes was used as the droplet microfluidic printhead. The injection capillary consisted of a round 1-mm diameter glass capillary that is pulled using a glass pulling device (MicroData Instruments Inc.) to form a tapered tip. The tip was subsequently polished using fine sandpaper (grit > 1500) to a final diameter of around 20 μm under an optical microscope. The collection capillary consisted of a round 1-mm diameter glass capillary whose length was limited to 0.75" to limit pressure build-up in the device. Both capillaries were aligned coaxially within a square glass capillary with 1.05 mm long sides and secured in place using Loctite clear epoxy glue. Blunt dispensing needles and polyethylene tubing were used to couple the glass capillary with a syringe pump (Harvard Technologies).

2.2.3 Inner Phase Formulation

Pure glycerol, fluorescein sodium salt, eutectic gallium-indium (eGaIn), poly(ethylene glycol) diacrylate (PEGDA) MW = 700 and diethoxyacetophenone (DEAP) were purchased from Sigma-Aldrich. The glycerol solution was generated by mixing pure glycerol into DI water at 62 wt.%. Fluorescein salt was added into the glycerol solution and DI water, giving them a strong green hue that fluoresces under UV light. The PEGDA solution was generated by dissolving 50 wt.% of PEGDA in deionized water, followed by addition of fluorescein salt. 3 wt.% of photoinitiator (DEAP) was added into the PEGDA solution to generate PEGDA particles upon UV exposure. The final appearance of the PEGDA solution with and without PI was a translucent grey liquid with a slight green hue.

2.2.4 Printing and Processing of Emulsion Inks

PDMS and the aqueous dispersed phase were supplied into the microfluidic printhead using a syringe pump (Harvard Technologies). The selected flow rate for PDMS was fixed at 1.50 mL/hr, and 2.00 mL/hr when

dispersing eGaIn, while the flow rate of the inner phase was adjusted to obtain the desired Q* values, where $Q^* = Q_{in}/Q_{out}$. Once the fluid phases in the microfluidic printhead reach hydrodynamic equilibrium, the devices were visually inspected for successful emulsion generation. Next, the printhead was mounted on a 3D printer machine, moved along the x, y and z directions to deposit the emulsion in 3D space according to the print path defined by the .gcode file used. The printhead travel speed was set to be equal to the velocity of the emulsion exiting the printhead (i.e. flow rate of PDMS and inner phase divided by cross sectional area of collection capillary). Upon successful printing of the emulsion inks, the printed constructs were then subjected to further processing that varied depending on the emulsion ink system. For glycerol and liquid metal droplets in PDMS, the constructs were heated at 75˚C for 24 hours to facilitate curing of the PDMS outer phase. For porous PDMS, the constructs were heated at 75˚C for 48 hours to both cure PDMS and evaporate the encapsulated water droplets. For PEGDA particles in PDMS, the constructs were first exposed to UV radiation from a 120 W mercury lamp to photopolymerize the PEGDA particles before being heated at 75˚C for 48 hours. All constructs in gel fraction experiments were exposed to UV if PI was present and subjected to heating at 75˚C for only 24 hours.

2.2.5. Compression Testing of PDMS Constructs

5-mm cube CAD files were converted into .gcode files to guide the motion of the printhead. Upon successful printing and curing of the printed cubes, the cubes were trimmed by hand to obtain flat surfaces and dimensioned prior to compression loading (Instron 1005, 10N load cell). The compressive extension rate and maximum applied compressive strain were set at 1.0 mm/min and 50\%, respectively. The mean and standard deviation of compressive elastic moduli were taken by calculating the stress-strain slope between 49 to 50% strain from three samples. The stress-strain curve whose elastic modulus is closest to the average was reported as the representative curve for its sample set (n = 3).

2.2.6. Surface Nanoindentation of PDMS Constructs

Samples were designed as 5-mm squares with a height of 2 mm. Samples were submerged in phosphate buffer solution and probed with a cantilever (OMCL-TR400PB) with a spring constant of 0.02 N/m at an indentation rate of 5 μm/second up until an indentation force of 5 nN is registered. For each sample, four force maps were obtained by selecting four 40 μm by 40 μm probing areas at random and obtaining 100 equally spaced points of data from each probing area. The 100 points were then fitted to a Gaussian distribution to determine a mean and standard deviation that was then reported on the plot in Fig. S3.

2.2.7. Swelling Ratio and Gel Fraction Determination

Printed 5-mm cubes (n = 3) were first weighed to record their original weights. Next, each individual sample was immersed in 5 mL of chloroform inside separate 20 mL glass vials for 48 hours. The samples were then dried for 1 minute under room ambient conditions before being weighed to record their swollen weight, which was then divided by the dry weight to obtain the swelling ratio. The samples were then left to dry for another 48 hours before being weighed once more to record their dried weight. The gel fractions were obtained by dividing the dried weight with the original weight.

2.2.8. Tensile Testing of Multi-Domain PDMS Samples

Tensile testing samples were generated by printing PEGDA-in-PDMS using a print path that was designed according to the dimensions of ASTM D638 type V test specimens. All testing samples (shown in Fig. 5) were only one layer thick (approximately 580 μm) and printed on a flattened sheet of aluminum foil. After thermal curing of the PDMS, the aluminum foil was dissolved in a 5.0M NaOH bath to liberate the tensile samples with minimal damage. To generate a step-change in the PEGDA particle content in PDMS, the feed of the inner phase was abruptly stopped at approximately halfway down the gauge length of the sample. Tensile stress-strain curves were obtained by subjecting the tensile samples to an extension rate of 25 mm/min until failure on a tensile testing machine (Instron 1028, 50 lb. load cell). The mean tensile elastic modulus was determined by taking the stress-strain slope up to 5\% strain from three samples. The stress-

strain curve reported in Fig. 5B. is derived from averaging the stress-strain data across different samples within each set.

2.2.9. Printing Magnetically-Actuated Soft Robotic Arm

The magnetically-actuated soft robotic arm in Fig. 5 was printed in several stages corresponding to the distinct compositional/functional domains. The pure PDMS and flexible PEGDA in PDMS segment was printed first using the PEGDA solution described earlier. Prior to printing the ferrofluid-in-PDMS segment, the microfluidic printhead was disconnected from the syringe pumps and the inner phase channel was rinsed once with deionized water. For the magnetically responsive segment, aqueous ferrofluid was dispersed in PDMS at a Q* = 0.05, which corresponds to Q_{in} = 75 µL/hr when Q_{out} = 1.5 mL/hr. The finished print was then subject to heating at 75˚C for 24 hours. To minimize damage to the finished prints, all objects were printed on aluminum foil substrates and subsequently liberated using NaOH same as before.

2.2.10. Soft Robotic Arm Characterization

To determine the lifting current of the soft robotic arms with different flexible segment configurations (i.e. different amounts of PEGDA particles), each soft robotic arm was laid flat on surface while a round electromagnet was suspended 10 mm above it. The electromagnet was then supplied with electric current that is gradually ramped up. The current at which the soft robotic arm is lifted up and held against the electromagnet is recorded as the lifting current (or $I_{lifting}$). Current measurements were performed in triplicate to obtain an average and standard deviation. To characterize the range of motion of the gripper arms in response to an external B-field, the arms were first suspended vertically. A round electromagnet is then placed next to the soft robotic arm at a horizontal distance of 10 mm. The round electromagnet was supplied with 36 Volts and 0.5 Amps, and the resulting deflection from the arms was visually analyzed using ImageJ to produce a quantitative measurement of the angular deflection of the soft robotic arm and the contributions from the flexible joints. The angles were recorded from three samples to report an average and standard deviation. The final magnetically-responsive soft robotic arm assembly consisted of 9/32”

stainless steel socket and multiple soft robotic arms attached to the round electromagnet using Loctite Plastics Bonding System and standard adhesive putty. The arms had flexible joints (Q* = 0.05) at locations 1 and 4.

2.3. Results and Discussion

2.3.1. 3D Printing Emulsion Inks Using a Droplet Microfluidic Printhead

Central to our strategy of using droplet inclusions to modify the functional properties of the surrounding matrix is the ability to controllably disperse droplets within another substance. We accomplished this by introducing an aqueous inner phase with PDMS outer phase within a standard glass capillary microfluidic device[19] while simultaneously depositing the resulting PDMS emulsion (Figure 1A and Movie S1). The PDMS outer phase, whose rheological properties are shown in Figure S1A, consisted of Dowsil SE 1700 and silicone oil; the former is a non-flowing elastomeric paste (μ = 500,000 cP) used for direct writing applications[9], and the latter is a liquid used as thinning agent. As opposed to previous reports of embedding of individual droplets into another phase at discrete points[20–22], the flowing PDMS outer phase is sufficiently capable of continuously shearing the aqueous inner phase into monodisperse droplets. The net result is the facile generation of PDMS emulsion inks that can be 3D printed into various geometries, as shown in Figure 1B.

The use of multiple flowing streams also allows us to independently control the injected fluid flow rates and to thereby tune the resulting emulsion characteristics. In Figure 1B, decreasing the flow rate of aqueous glycerol with fluorescein (Q_{in}) relative to PDMS (Q_{out}) caused a reduction in droplet volume fraction and droplet diameter, resulting in a visible decrease in fluorescence intensity. The relationship between Q*, where $Q^* = Q_{in}/Q_{out}$, and droplet diameter is graphically illustrated in Figure S1B. It should be noted that the exact relationship between Q*, droplet diameter and droplet generation frequency varies from device to device based on its key dimensions, such as the injection and collection capillary separation distance[23]. While the incorporation of microfluidics for blending miscible inks prior to extrusion printing has been

previously reported[9,10], our ability to 3D print highly textured constructs by mixing immiscible fluid streams using a droplet microfluidic approach represents a budding and unique application of these same principles and tools in an extrusion-based printing context.

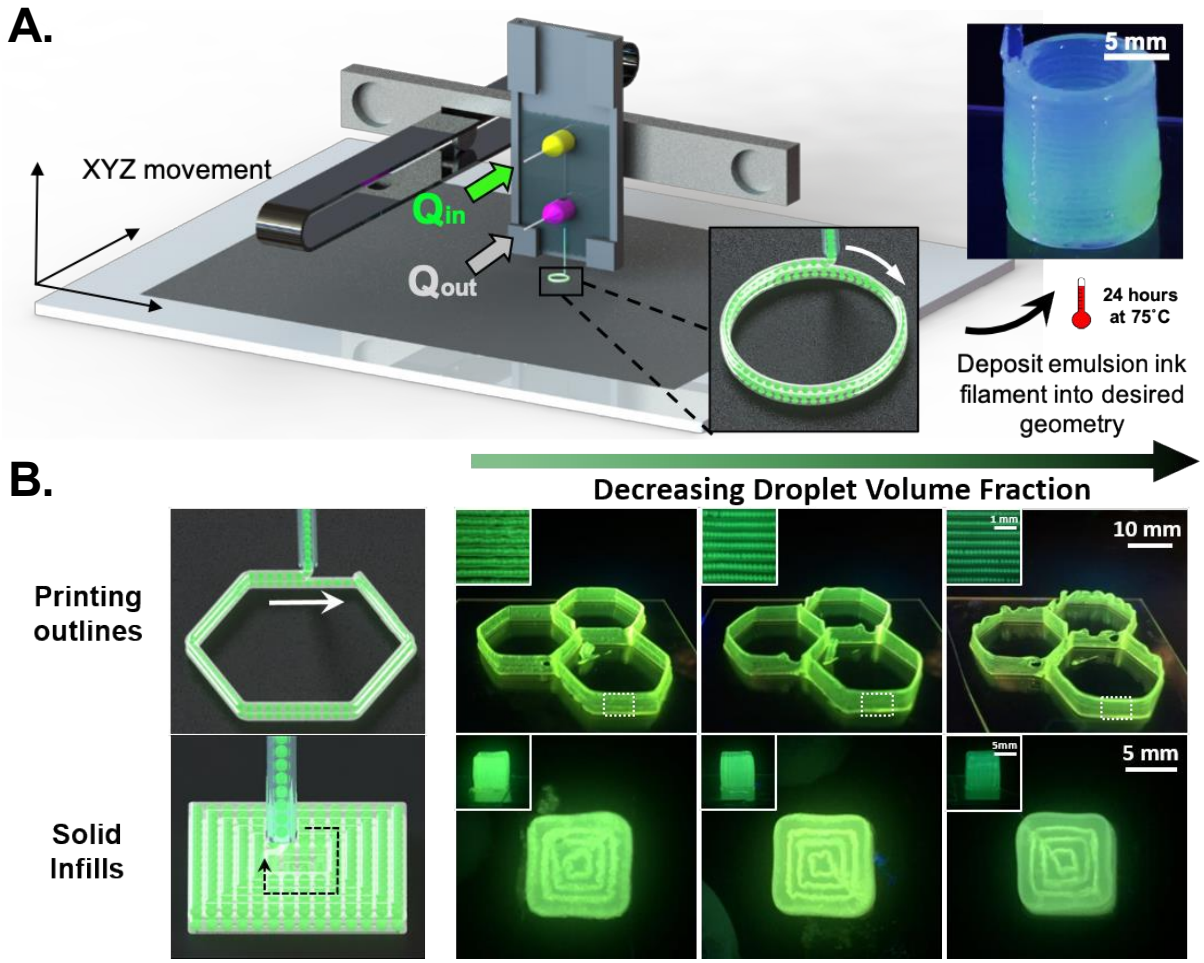

Figure 1. In situ dispersion and 3D printing of aqueous droplets in PDMS. **(A)** Schematic of droplet microfluidic 3D printing process. Q in and Q out refer to the flow rates of the inner (aqueous glycerol) and the outer (PDMS) phase, respectively. Inset shows experimental image of a cylinder printed from PDMS with aqueous droplet (with 62 wt% glycerol) inclusions. The green glow arises from the dissolved sodium fluorescein in the aqueous inner phase. **(B)** Printing constructs consisting of outlines and solid infills with different droplet volume fractions, which are controlled by adjusting the ratio of Q_{in} and Q_{out}. Droplet volume fractions from Left to Right are 16.7, 9.1, and 4.8%, respectively. Top Insets and Bottom Insets are micrographs of the printed outline objects and front view images of the solid infill objects, respectively.

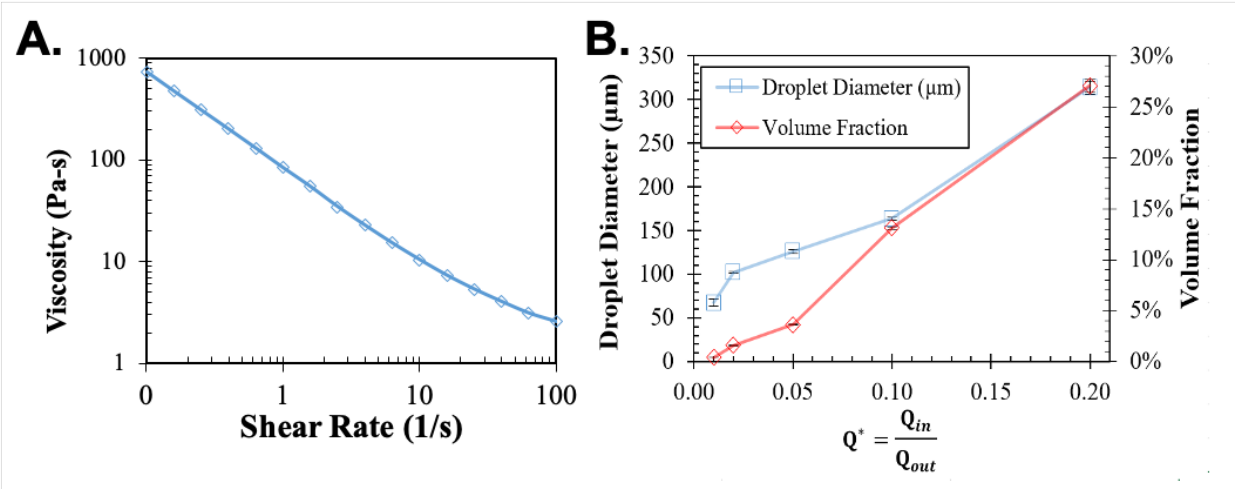

Figure S1. Rheological and droplet dispersion characterization of the PDMS phase. (A) Curves showing the viscosity of the PDMS outer phase (55 wt.% SE 1700, 1:10 ratio of curing agent to elastomer, and 45 wt.% silicone oil) as a function of shear rate. The relevant shear rates in our microfluidic printhead does not exceed $O(100\ s^{-1})$. (B) Curves characterizing the droplet generation of glycerol in PDMS for a representative device. The relationship between droplet diameter and Q* deviates from perfect linearity due to change in droplet generation frequency with Q*. Volume fraction is determined by calculating the total volume of droplets produced per unit time and dividing that by the total flow rate (i.e. $Q_{in} + Q_{out}$) per unit time.

2.3.2. Mechanical Anisotropy in PDMS Constructs Made With Different Printing Paths

We explored the impact of choosing different 3D printing paths on the properties of these highly textured PDMS constructs. For our comparison, we printed solid cubes using concentric (Con), bidirectional (Bi) and unidirectional serpentine (Uni) printing paths. The schematic and experimental images of the constructs made using each print path are shown in Figure 2A. The layer-by-layer deposition of PDMS emulsion filaments results in a closer packing of droplets along the print direction compared to the vertical direction (i.e. the z-axis) as shown in Figure 2B. At Q* = 0.20, we counted 5-6 droplets per mm in the y-axis, with droplets overlapping one another by several tens of microns. Note that the overlap becomes more pronounced under compression. In contrast, the z-axis has 2-3 droplets per mm, with droplets separated by a layer of PDMS with thicknesses of 308 and 144 µm at Q* = 0.05 and 0.20, respectively (Figure S2A).

We hypothesized that, despite the spherical nature of the droplets, our PDMS prints would exhibit anisotropic mechanical behaviour owing to differences in droplet distribution in the x, y and z-axes.

Specifically, the constructs will have different elastic moduli in the z versus x and y-axes. Note that the concentric (Con) and bidirectional (Bi) constructs shall have identical elastic modulus in the x and y-axes due to their rotational symmetry. To test our hypothesis, we subjected the cubic prints to uniaxial compression testing in all three directions and measured the mean elastic modulus of the constructs accordingly.

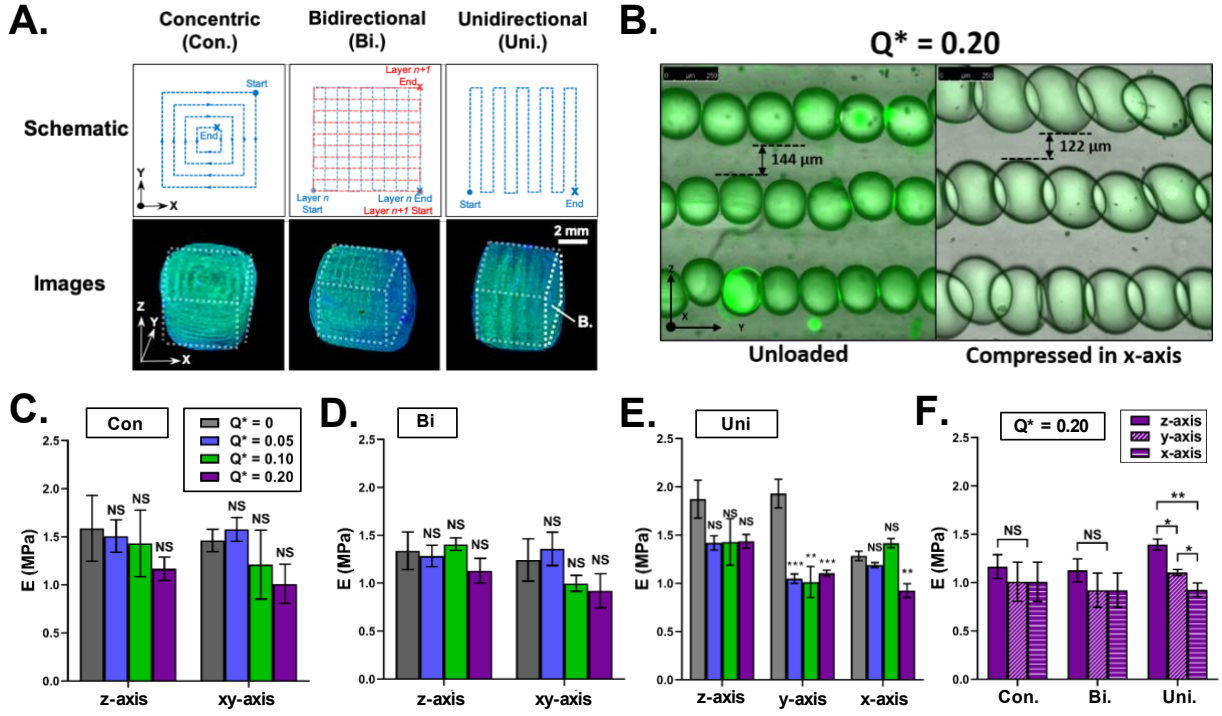

Figure 2. Mechanical responses of PDMS constructs with droplet inclusions at various printing paths. (A) Schematic and experimental images showing three different printing paths: concentric (Con), bidirectional (Bi), and unidirectional serpentine (Uni). All PDMS constructs used here contain aqueous droplets with glycerol. (B) Representative micrograph of the face (y–z plane) highlighted in A showing multiple PDMS emulsion filament layers stacked in the z-axis for Q_ = 0.20. Under compression in the x axis, the droplets expand in the y–z plane and visibly overlap with one another. (Scale bar, 250 _m.) (C–F) Measured elastic moduli from compressing glycerol-in-PDMS constructs show mechanical anisotropy in the Uni printing path. All printed PDMS constructs were cured for 24 h at 75˚C. * $P < 0.05$, ** $P < 0.01$, *** $P < 0.001$, respectively, using Student's t test. Error bars shown are SD. NS, not significant.

When the print path and direction of mechanical loading were kept constant, the elastic modulus in the x, y and z-axes showed no significant changes as Q* increased from 0 to 0.20 in the Con constructs (Figure

2C). The same insensitivity to Q* in all three directions was observed in Bi constructs (Figure 2D) . The Uni constructs showed no significant change in the z-axis elastic modulus with increasing Q*. However, in the y and x-axes, the elastic modulus decreased by 43% (from 1.93 ± 0.30 and 1.11 ± 0.06 MPa) and 8% (from 1.28 ± 0.10 and 0.93 ± 0.14 MPa) when Q* increased from 0 to 0.20 (Figure 2E). At Q* = 0.20, the variation in elastic moduli in the x, y and z-axes became more pronounced in the Uni constructs (Figure 2F), with constructs being consistently stiffer in the z-axis than in other directions. These results suggest that droplet organization in the Uni printing path gives rise to mechanical anisotropy in PDMS constructs. We however note the biphasic behavior of Uni prints in the x-axis as Q* increases from 0 to 0.20 (Figure 2E), which is likely due to poorer ink fusion in the x-axis (i.e. the direction orthogonal to the print direction) as evidenced in the control when Q* = 0 (i.e. no liquid inclusions) (Figure S2B).

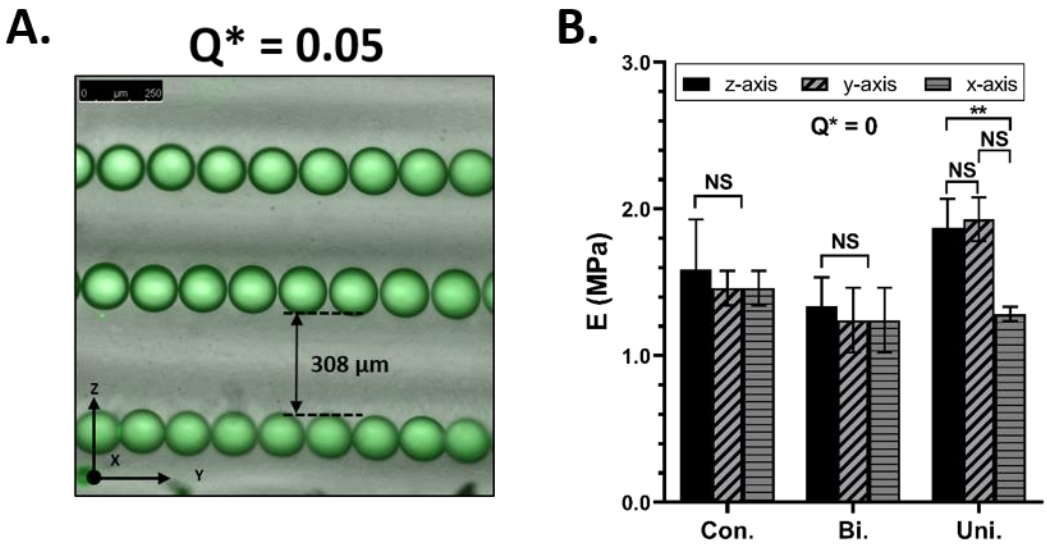

Figure S2. Mechanical anisotropy in PDMS constructs. A. Micrograph showing multiple PDMS emulsion filaments stacked in the z-axis for Q* = 0.05. B. Comparison of the effect of print path and loading orientations when no inner phase is present (i.e. Q* = 0). **p<0.01, using student t-test. Error bars as shown are SD. NS, not significant.

Previous studies have shown how droplet inclusions in solids can result in either softening or stiffening depending on the liquid and solid properties[24–27]. Specifically, the liquid droplets will mimic rigid inclusions and stiffen the surrounding solid matrix once the droplet diameter decreases below a characteristic elastocapillary length, which is defined by the relationship L = γ/E, where γ is the liquid surface tension

and E is the solid elastic modulus[24]. The characteristic length in this study is calculated to be O(10 nm) for a PDMS and aqueous glycerol combination, meaning our micrometer-sized droplets (50 μm to 200 μm) soften the PDMS, consistent with the experimental observations. In addition, our results show that the extent to which droplet inclusions soften 3D printed solids is dependent on print path and that this softening occurs preferentially in the direction of the close-packed and overlapping droplets as per our hypothesis. For example, only the Uni constructs displayed significant softening as droplet content (or Q*) increases, and the softening was predominantly observed in the y and, to a lesser extent, x-axes. We reckon that further theoretical studies are needed to corroborate our results and to determine how organization of liquid inclusions of different length scales interact with each other and the surrounding solid matrix.

2.3.3. Softening PDMS Constructs Using Droplets with Different Constituents

Having shown that printing path is a significant factor in softening PDMS constructs using aqueous glycerol droplet inclusions, we then sought after a different inner phase constituent that could more effectively soften the PDMS without relying on these printing parameters. At the same time, we also aimed to demonstrate the flexibility of our droplet-based strategy in handling a broad range of immiscible inks. To this end, we swapped out aqueous glycerol for other liquids including water (no glycerol), eutectic gallium-indium (eGaIn) and PEGDA prepolymer solution. Dispersing water droplets in PDMS and subsequent thermal processing resulted in PDMS with empty pores, which was visually confirmed as shown in Figure 3A. Upon escaping the surrounding gas-permeable PDMS, the water left behind only fluorescein salt crystals that roughly outline the pores, resulting in a porous PDMS construct. The stress-strain curves obtained from compression testing of the porous PDMS cubes are shown in Figure 3B. Analysis of the stress-strain curves reveal that the elastic modulus decreased by approximately 22.6% from 2.39 ± 0.12 to 1.85 ± 0.20 MPa as Q* changed from 0 to 0.20. Note the significantly higher elastic modulus of the Q* = 0 porous PDMS constructs compared to the Q* = 0 glycerol-in-PDMS constructs used previously (1.34 ± 0.38 MPa) was attributed to the increased thermal processing time (48 h) associated with evaporating the water droplets in PDMS.

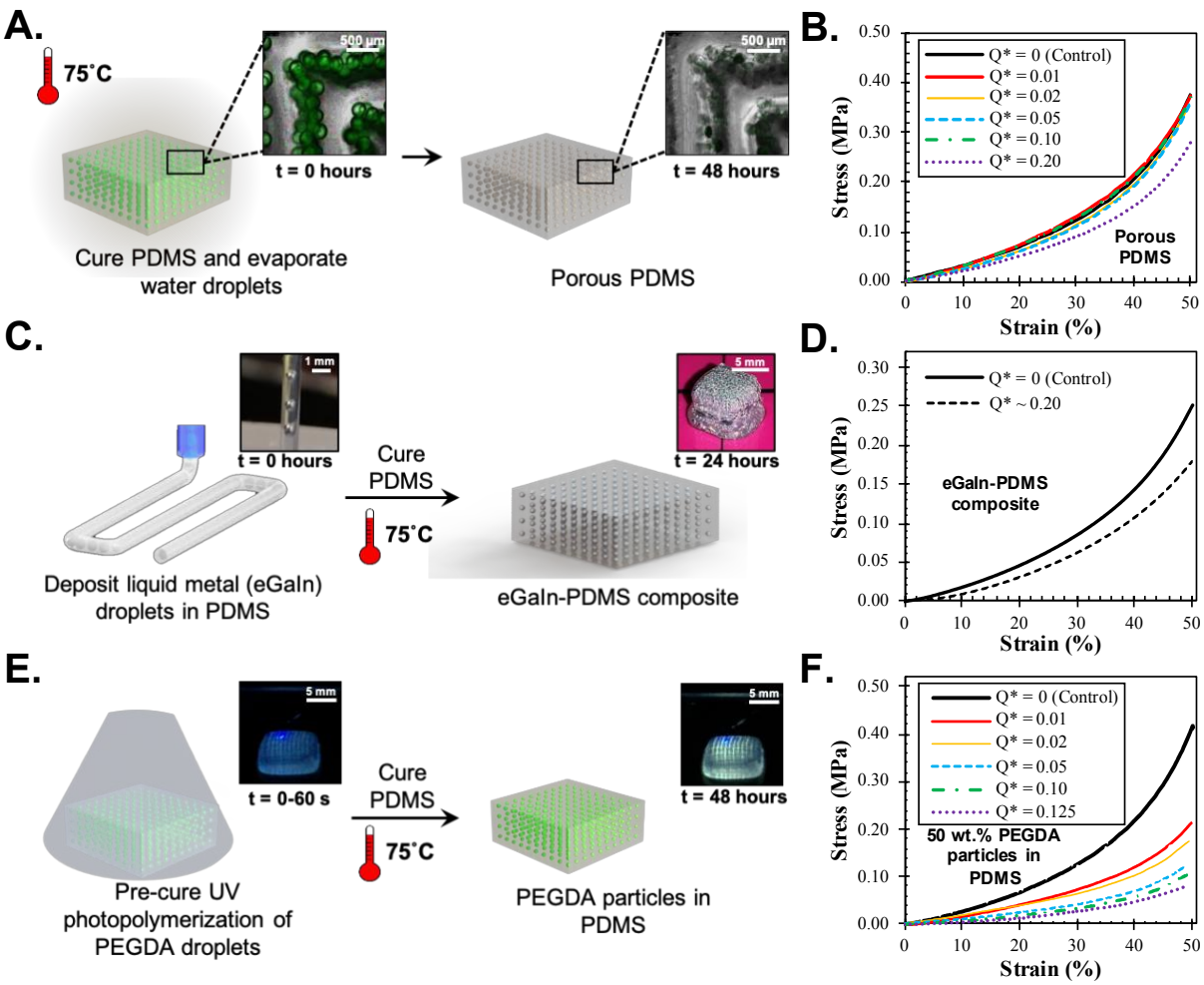

Figure 3. Softening in 3D-printed PDMS constructs with different inner phase constituents. (A) Schematic of generating porous PDMS from 3D-printed PDMS with water (no glycerol) droplet inclusions. Insets are micrographs of PDMS prints containing water droplets before and after evaporation of droplets. (B) Representative compressive stress–strain curves of porous PDMS with different Q*. Controls (i.e., Q* = 0) consist of pure PDMS prints with no inner phase present. (C) Schematic of 3D printing liquid metal (eGaIn)-PDMS composites. Left and Right Insets show the dispersal of eGaIn into droplets in PDMS and a 5-mm cube of printed eGaIn-PDMS composites, respectively. (D) Representative compressive stress–strain curves of pure PDMS (control) and eGaIn-PDMS composites. (E) Schematic of converting PEGDA droplets in 3D-printed PDMS into PEGDA particle inclusions via UV photopolymerization. (F) Representative compressive stress–strain curves of PEGDA particles-in-PDMS prints with different Q*.

Next, we dispersed eutectic gallium-indium (eGaIn) in PDMS and mechanically characterized the resulting eGaIn-PDMS composite under compression. Whereas liquid metal inclusions in soft materials were previously achieved via vortex mixing or sonication[28–30], we report for the first time, as far as our knowledge is concerned, the simultaneous formation and 3D printing of liquid metal-PDMS composite inks (Figure

3C). Under compression, the eGaIn-PDMS composite appeared to be softer than pure PDMS. Analysis of compression stress-strain curves in Figure 3D revealed that including liquid metal droplets at Q* = 0.20 (or 16.7 vol.%) in PDMS resulted in a decrease of 27% in elastic modulus from 1.32 ± 0.29 to 0.96 ± 0.18 MPa. A previous study reported that the mean elastic modulus of PDMS elastomers increased from 0.65 to 0.95 MPa as the liquid metal droplet content increased from 0 to 13 vol.%. We attribute the stark difference between our results to the size liquid metal droplets used. Whereas the eGaIn droplets in our constructs were hundreds of micrometers in diameter, the previous study used droplets that were hundreds of nanometers in diameter, which is on the same order of magnitude as the characteristic elastocapillary length for liquid metal in PDMS, thus resulting in elastocapillary stiffening[24].

Finally, we sought to include solid particles in PDMS. As shown in Figure 3E, our strategy for realizing this involved using polyethylene glycol diacrylate (PEGDA) prepolymer solution with 3 wt.% diethoxyacetophone photoinitiator (PI) as the inner phase. Upon dispersal in PDMS, the PEGDA prepolymer droplets were exposed to UV before thermal curing of PDMS. We observed that upon successful photopolymerization of PEGDA prepolymer solution, the fluorescence intensity of the dissolved fluorescein salt increases (Figure 3E). We attribute this to differences in fluorescein salt solvation between PEGDA prepolymer solution and solid polymer[31,32].

The stress-strain curves for compressing PDMS with PEGDA particle inclusions are shown in Figure 3F. At first glance, the softening effect arising from the PEGDA particles is already significantly greater compared to that arising from other inner phase constituents. Indeed, the elastic modulus between Q* = 0 to 0.125 decreased by 85% from 2.64 ± 0.56 to 0.42 ± 0.08 MPa in PDMS constructs with PEGDA particles. In contrast, aqueous glycerol droplets, porous PDMS and eGaIn droplets at Q* = 0.20 only decreased the elastic modulus by 16, 23 and 27%, respectively (Table S1). Strikingly, surface nanoindentation of these PEGDA particle-in-PDMS constructs revealed similar trends, with the mean elastic modulus decreasing by over 95% from 2.17 to 0.06 MPa as Q* changed from 0 to 0.125 (Figure S3). As the range of AFM

indentation is less than 500 nm, this would indicate that the dramatic softening effect is not an extrinsic phenomenon arising only from bulk compression, but that the entirety of the PDMS, from the internal PDMS/PEGDA interface to the external surface, is intrinsically softer due to the introduction of PEGDA particles.

Table S1. List of calculated elastic modulus values for different inner phase constituents, as well as p values comparing the control and max Q* cases. The control refers to when there is no inner phase (i.e. Q* = 0), and the max refers to Q* = 0.20 (or 0.125 in the case of PEGDA). All PDMS constructs used in compression testing were printed using the bidirectional serpentine (or Bi) printpath and loaded in the z-axis. Values are expressed as mean ± SD. SD values are formatted to 2 decimal places. P values are taken from student t-test and formatted to 2 significant figures.

Inner Phase	Control Elastic Modulus (MPa)	Max Q* Elastic Modulus (MPa)	n	P value
62 wt.% glycerol	1.34 ± 0.20	1.13 ± 0.13	3	0.11
Water	2.39 ± 0.06	1.85 ± 0.10	3	0.0020
eGaIn	1.32 ± 0.14	0.96 ± 0.09	3	0.0048
50 wt.% PEGDA + 3 wt.% PI	2.64 ± 0.28	0.42 ± 0.08	3	0.00019

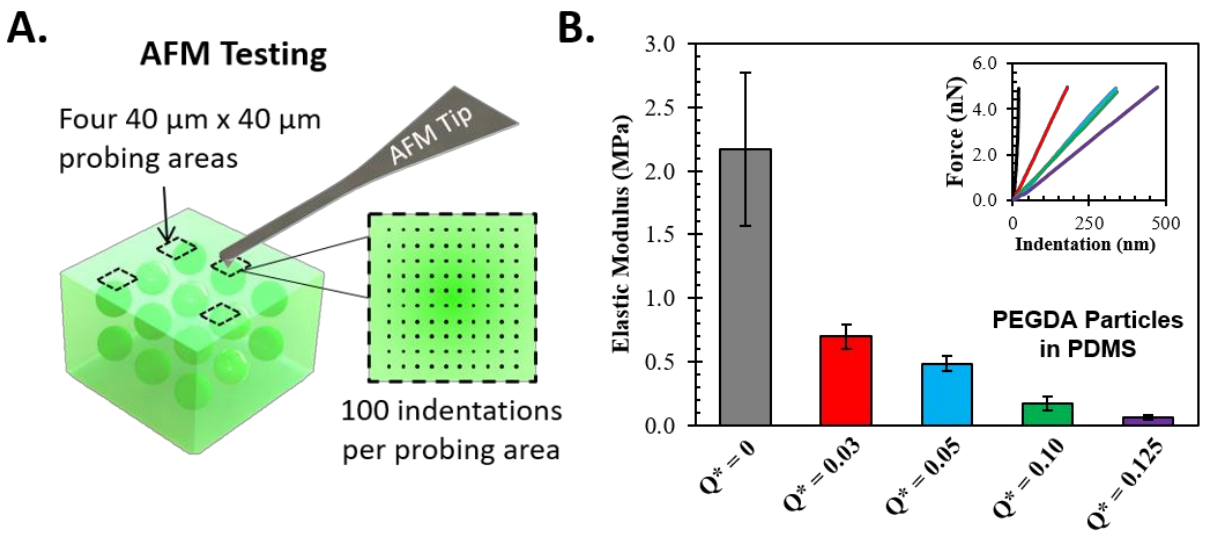

Figure S3. Surface nanoindentation confirms intrinsic softening of PDMS elastomer. A. Schematic of atomic force microscopy (AFM) surface nanoindentation of different 3D-printed PDMS constructs with PEGDA particle inclusions. B. Plot of calculated from AFM force-indentation of various Q* in PEGDA particles-in-PDMS. Inset shows the representative force-indentation curves. Samples were indented with a pyramidal tip (k = 0.10 kN/m) until a force of 5 nN was registered and the corresponding indentation depth was measured. Note, the maximum recorded indentation depth is 466 nm. Error bars as shown are SD.

2.3.4. PEGDA Inclusions Soften PDMS Constructs by Chemically Modulating PDMS Crosslinking Process

We then sought to understand the mechanism behind the dramatic softening of 3D printed PDMS constructs using PEGDA particle inclusions. First, we hypothesized that the inclusion of diethoxyacetophenone as a photoinitiator (PI) in the PEGDA inner phase is primarily responsible for softening the bulk PDMS via disruption of the crosslinking process[33]. To test this, we measured the swelling ratios and gel fractions of the PEGDA-in-PDMS constructs with and without PI along with stress-strain data to characterize the contributions of PDMS polymer chemistry to the observed softening effects.

From the stress-strain curves in Figure 4A, adding PI in the PEGDA droplet inner phase softened the bulk PDMS in a dose-dependent manner. As the amount of PI increased from 0 to 3 wt.\%, the mean elastic modulus of the bulk PDMS decreased by 31% from 0.77 ± 0.18 to 0.53 ± 0.24 MPa (Table S2). However, we note that the elastic modulus at 0 wt.% PI was already significantly lower than the pure PDMS case (1.36 ± 0.12 MPa). Furthermore, swelling ratio and gel fraction calculations show only mild changes as the amount of PI increased (Figure 4B). When we replaced PEGDA with a glycerol solution, we found that even as the amount of glycerol droplets with 3 wt.% PI dispersed in PDMS increased from Q* = 0 to 0.125, the compressive stress-strain curves remained relatively unchanged (1.23 ± 0.10 to 1.25 ± 0.27 MPa), as shown in Figure S4A. Likewise, gel fraction and swelling ratio exhibited minor changes (Figure S4B). The results thus show that PI is not wholly responsible for the dramatic softening of PDMS and that PEGDA by itself may play an essential role in the intrinsic softening of PDMS. To test this, we varied the PEGDA wt.% while keeping the PI concentration at 0 wt.% and dispersed the PEGDA aqueous solution in PDMS at Q* = 0.125. As seen in Figure 4C, varying the PEGDA wt.% in solution resulted in a dramatic change in the bulk PDMS compressive stress-strain behavior. As the PEGDA wt.% increased from 0 to 75%, the compressive elastic modulus changed from 1.23 ± 0.41 to 0.48 ± 0.07 MPa, which corresponds to a decrease of roughly 61% (Table S3). As PEGDA wt.% changes from 0 to 25, the swelling ratio increased by about 40 % from 3.64 ± 0.03 to 5.1 ± 0.3, while the gel fraction decreased by 7.7% from 0.567 ± 0.005 to 0.49 ±

0.02 (Figure 4D), indicating that the presence of PEGDA by itself lowers both the crosslinking density of the bulk PDMS and the relative amount of polymer bound in the crosslink network. We deduce that these chemical changes are then reflected in the mechanical softening of PDMS as shown in the compression stress-strain curves. Altogether, PEGDA and PI work synergistically to soften the surrounding PDMS phase, with PEGDA being the more significant contributor based on its double effect on polymer chemistry.

Table S2. List of calculated elastic modulus values for different PI content in 50 wtPEGDA droplet inclusions. Values are expressed as mean ± SD, which is formatted to 2 decimal places. P values are taken using student t-test and formatted to 2 significant figures.

Photoinitiator (PI) amount (wt.%)	Elastic Modulus (MPa)	n	P value
0	0.77 ± 0.10	3	-
0.3	0.67 ± 0.10	3	0.14
1.0	0.55 ± 0.11	4	0.016
3.0	0.53 ± 0.12	3	0.028

Table S3. List of calculated elastic modulus values for different PEGDA content with no PI. Values are expressed as mean ± SD, which is formatted to 2 decimal places. P values are taken using student t-test and formatted to 2 significant figures.

PEGDA content (wt.%)	Elastic Modulus (MPa)	n	P value
0	1.23 ± 0.21	3	-
10	0.88 ± 0.06	3	0.055
25	0.71 ± 0.02	3	0.025
50	0.65 ± 0.05	3	0.021
75	0.48 ± 0.04	3	0.013

Mechanistically, we infer that the PEGDA molecules are participating in side reactions with the individual PDMS constituent molecules, thereby modifying the polymer chemistry of PDMS itself, which is visualized in Figure 4E. Standard crosslinking of PDMS involves terminal vinyl groups in the PDMS macromonomer reacting with hydrogen donors found in the crosslinker molecule. With the introduction of PEGDA molecules, the acrylate end-groups which contain unsaturated carbon-carbon bonds may compete for hydrogen donors provided by the crosslinker molecules[34]. As a consequence, the PEGDA molecule acts as a contaminant that adds itself to the otherwise pristine PDMS crosslink network, resulting the softening of the PDMS network.

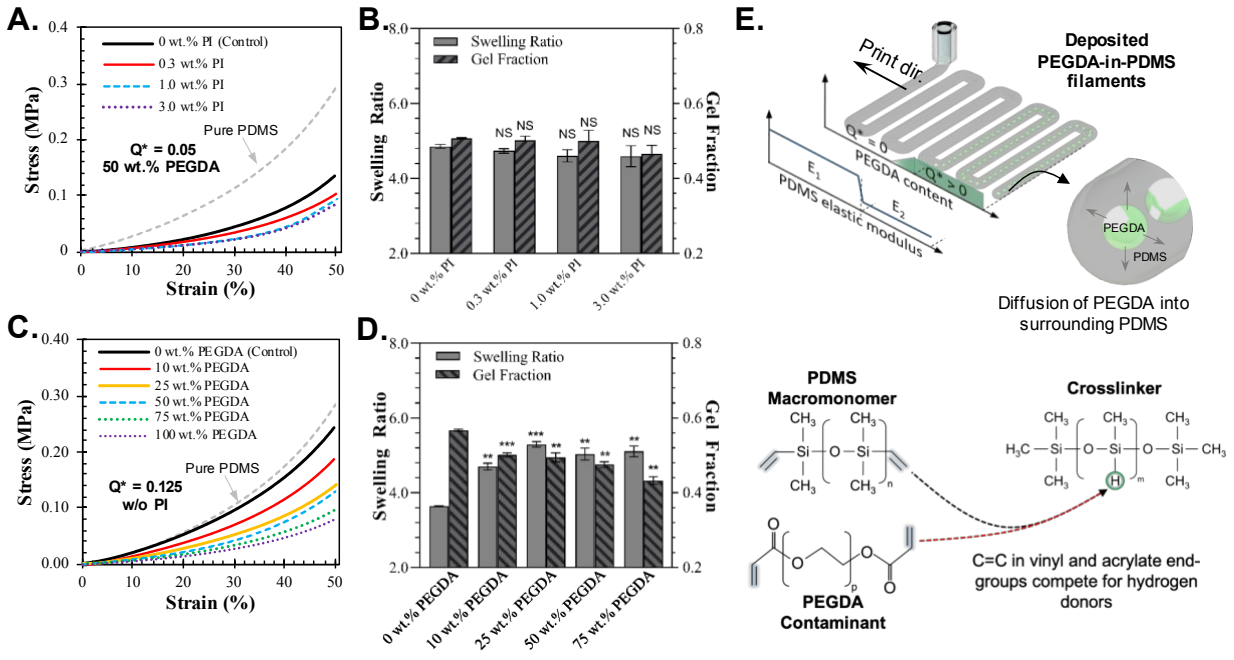

Figure 4. Dose-dependent softening of PDMS constructs using PEGDA inclusions. (A) Representative compressive stress–strain curves of PDMS with 50 wt.% PEGDA at various PI weight percentages. Controls refer to PDMS with 50 wt.% PEGDA droplet inclusions (Q* = 0.05) without PI. The pure PDMS (i.e., no inner phase) stress–strain curve is included for comparison. (B) Plot of calculated swelling ratios and gel fractions of PDMS with 50 wt.% PEGDA at various PI weight percentages, Q* = 0.05. (C) Representative compressive stress-strain curves of PDMS with droplets of different PEGDA-water solutions, Q* = 0.125. Controls refer to PDMS with water (no glycerol) droplet inclusions (Q* = 0.125). The pure PDMS (i.e., Q* = 0) stress–strain curve is included for comparison. (D) Plot of calculated swelling ratios and gel fractions of PDMS with droplets of different PEGDA–water solutions. Q* = 0.125. All constructs used here were heated to 75˚C for 24 h. (E) Schematic of the variation of PDMS elastic modulus resulting from PEGDA inclusions. Note the roles of diffusion and chemical interactions between PEGDA inclusions and PDMS cross-linker. * $P < 0.05$, ** $P < 0.01$, *** $P < 0.001$, t test. Error bars shown are SD. NS, not significant.

The occurrence of the proposed reactions is predicated upon the ability of PEGDA molecules to move beyond the PEGDA/PDMS interface and diffuse into the surrounding PDMS, as depicted in the schematic in Figure 4E. We believe this to be the case given the results from surface nanoindentation reported earlier. This consequently suggests that the range of PEGDA movement through the PDMS and subsequent interactions is on the order of hundreds of micrometers at minimum. In addition, the movement of PEGDA through PDMS, at least in its pre-cured state, is consistent with previous observations made in water-in-oil emulsions where hydrophobic and hydrophilic substances diffuse out aqueous droplets and through the oil continuous phase into neighboring drops[35]. The out-diffusion of these substances requires that the

substances are capable of partitioning at the phase boundary, which is highly likely in our case due to the mildly hydrophilic nature of PEGDA by virtue of its acrylate end-groups[36]. Taking this all together, we report the novel use of PEGDA droplet inclusions to modify the chemistry of PDMS, resulting in an elastomer that is an order of magnitude more mechanically compliant than unmodified PDMS.

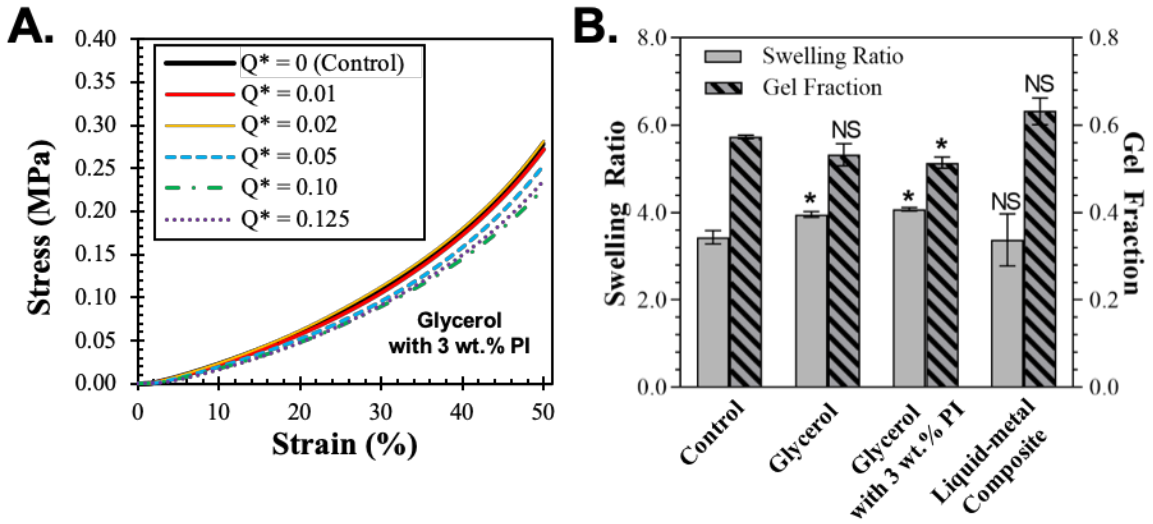

Figure S4. Investigation of PEGDA-mediated softening of PDMS using mechanical and polymer chemistry characterization. A. Representative compression stress-strain curves of PDMS samples with glycerol droplet inclusions and 3 wt.% PI for various Q* values. The control refers to PDMS with no inner phase (i.e. Q* = 0). B. Plot of calculated swelling ratios and gel fractions for PDMS with glycerol (Q* = 0.20), glycerol (Q* = 0.125) with PI and eGaIn inclusions (Q* ~ 0.20). The control refers to PDMS with no inner phase. * $p < 0.05$, student t-test. Error bars as shown are SD. NS, not significant.

2.3.5. Spatially-Defined Softening and Magnetization in 3D Printed Soft Actuator

The dramatic softening of PDMS using PEGDA inclusions, combined with the ability of our setup to independently control the inner and outer phase fluid flow rates, constitutes a novel strategy for generating heterogeneous constructs. We demonstrate this by printing single-layer dogbone-shaped tensile samples featuring a step-change in the inner phase content. We chose to use PEGDA particle inclusions to soften the PDMS due to the synergy between PEGDA and PI to modulate the chemistry of PDMS. The result is a construct consisting of two distinct compositional and functional domains, depicted as sample III in Figure 5A. We then subjected these samples to uniaxial tensile testing to produce the curves shown in Figure 5B.

Inspecting the curves, we observed that the sample with a step-change in PEGDA particle content (III) is nearly identical to that of the sample with a homogeneous distribution of PEGDA particles (II), and that they are both visibly more compliant than the pure PDMS sample (I). This, coupled with visual analysis of stretching sample III as shown in the inset of Figure 5B, led us to infer that the bulk tensile behavior was dominated by the mechanically compliant half consisting of PDMS with PEGDA particle inclusions. Meanwhile, the other half of the sample visibly retained the more rigid mechanical behavior of pure PDMS. Moreover, sample III had a mean breaking strain that is close to 50% of that for sample II (1.21 vs 2.07 mm/mm). This is consistent with the step change in PEGDA particle content being located roughly in the middle of the sample gauge length, as well as the fact that virtually all of the strain or deformation is sustained by mechanically compliant half.

Based on the demonstrated ability to produce constructs with mechanical heterogeneity, we conceptualized a primitive 3D-printed soft actuator that could bend or deflect at selected points in response to an external magnetic field (or B-field). As a proof of concept, we first generated flat single layer sheets (Figure 5C) consisting of three domains: a pure PDMS portion for attachment purposes, a portion with PEGDA particle inclusions to act as a flexible joint, and a magnetically-responsive portion with aqueous ferrofluid inclusions (Movie S2). We varied the Q* of PEGDA particles in the flexible joint and recorded its impact on the flexing capabilities of these samples as shown in Figure 5D. Increasing the Q* of PEGDA particles in the flexible joint resulted in a lower lifting current ($I_{lifting}$), which is defined as a the minimum current required to lift up the sheets 90 degrees from rest. These results simultaneously indicate that the ferrofluid droplet inclusions successfully imparted magnetism and that the printed PEGDA-in-PDMS flexible joint effectively behaved as a flexural hinge to facilitate bending.

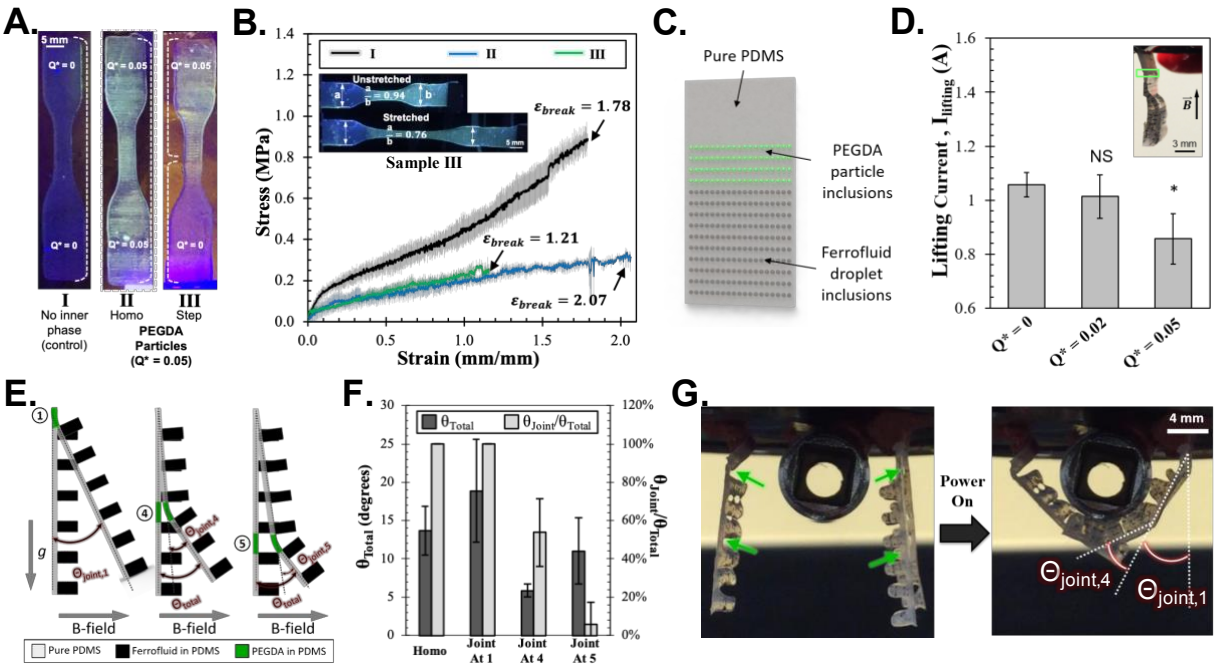

Figure. 5. Design, optimization, and operation of a 3D-printed soft-robotic gripper arm assembly. (A) Experimental images of dog bone tensile samples consisting of (I) pure PDMS, (II) homogeneous PEGDA particles in PDMS (at Q* = 0.05), and (III) step-change PEGDA particles in PDMS at Q* = 0 and 0.05. (B) Representative tensile stress–strain curves for sample sets I, II, and III, with annotations of breaking strain (ε_{break}). Insets are images of a step-change sample before and after stretching. The ratio of grip section widths is depicted to highlight the compositional and functional domains. All samples (n = 3) were extended at a rate of 25 mm/min. (C) A schematic of the proof-of-concept single-layer sheets with three domains: a region with no droplet inclusions, a mechanically compliant region with PEGDA particle inclusions, and a magnetically responsive region with aqueous ferrofluid droplet inclusions (Q* = 0.05). (D) Plot of lifting current ($I_{lifting}$) of sheets with different PEGDA particle content. Inset is image showing the printed sheet. The domain containing PEGDA particles is highlighted by a green box. (E) A schematic of the magnetically actuated printed soft actuators with flexible joints. The toothed portions contain ferrofluid inclusions. The possible locations of flexible PEGDA in PDMS joints (locations 1, 4, and 5) as well as the corresponding deflection angles are shown. (F) Plot of the deflection angles (θ_{total} and θ_{joint}) of each joint configuration in response to the same external B field. For the homo (homogeneous) and joint at 1 samples, the value of θjoint is the same as θ_{total}. (G) Experimental images showing the whole gripper arm assembly. Three 3D-printed gripper arms with flexible joints at locations 1 and 4 attached to an electromagnet wrap around the stainless-steel socket when the electromagnet is powered (applied current = 1.0 A). Green arrows indicate where the flexible joints are located. Angles of deflection from each joint are also shown. * $P < 0.05$, t test. Error bars shown are SD.

Having demonstrated our ability to incorporate mechanically compliant and B-field responsive domains into a larger printed construct, we generated a soft gripper arm whose design is illustrated in Figure 5E. The gripper arms featured a base layer of PDMS and toothed portions consisting of PDMS with aqueous ferrofluid inclusions. On the base PDMS layer, we identified specific locations on which we could place mechanically compliant PEGDA-in-PDMS in order to maximize B-field induced angular deflection. For

subsequent range of motion testing, we prepared samples with one flexible joint located either at the top (location 1), halfway down (location 4), near the bottom (location 5), or homogeneously distributed throughout the length of the gripper arm as a control (Figure S5). Note that due to the cantilever configuration of our gripper arms, the total angular deflection θ_{Total} has of two distinct contributions: one from the top and the other from the joint itself θ_{Joint}. These angles are illustrated in Figure 5E.

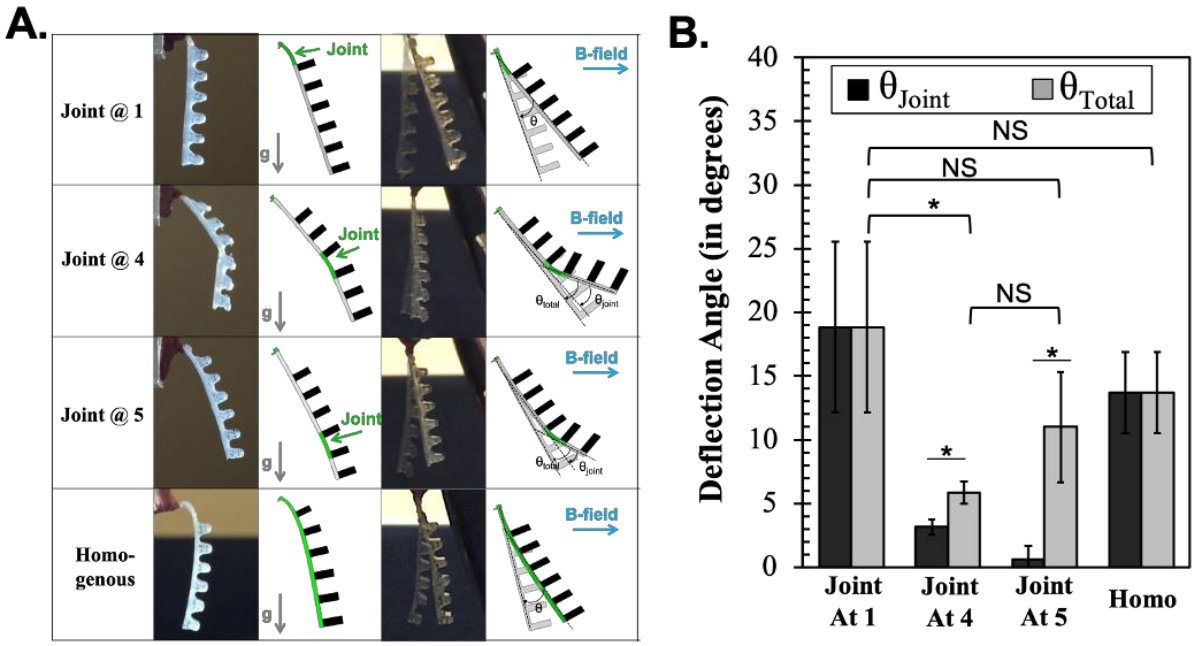

Figure S5. Design and optimization of softened PDMS joints in a soft-robotic gripper arm assembly. An illustration of the different flexible joint configurations considered for optimizing the deflection/bending response of the gripper arm. Left: experimental images and schematics of the different configurations under the load of gravity. Right: experimental images and schematics of the motion expected when subjected to an external B-field in the transverse direction.

Deflection angles from range of motion testing are measured and the results shown in Figure 5F. Placing the flexible joint at location 1 produced the highest mean θ_{Total}, making it the best location for a flexible joint. We also considered the need to have the gripper arms deflect midway along its length (i.e. at locations 4 or 5) as this would improve its ability to wrap around objects. Thus, in addition to θ_{Total}, we also measured the distinct angular deflection contribution (or θ_{Joint}) arising from when flexible joints are at locations 4 or 5. We found θ_{Joint} normalized by θ_{Total} at location 4 to be 54% compared to 6% at location 5, meaning that the flexible joint at location 4 is comparatively more capable of bending in response to an external B-field.

Having characterized the range of motion arising from the different flexible joints locations, we sought to demonstrate the gripping ability of our primitive 3D-printed gripper arm. To this end, we attached three gripper arms with flexible joints at locations 1 and 4 onto an electromagnet that would wrap around a stainless steel socket upon powering the electromagnet (Figure 5G). We observed that the gripper arm produced distinct deflection angle contributions at location 1 and 4 as intended. With this setup, we were able to lift and hold objects weighing several hundreds of milligrams (Movie S3). While 3D printed soft actuators[37,38] or shape-changing (or 4D) constructs[39–41] have been reported previously, such results were accomplished using functional inks that are prepared beforehand with fixed composition. In contrast, our results demonstrate the ability of selectively dispersed droplet inclusions to locally tune the functional properties in printed constructs.

2.4. Conclusion

We present a versatile strategy for the modulation of printed construct properties across space using droplet inclusions. By co-flowing immiscible inks in a microfluidic printhead, we could concurrently generate and extrude highly textured inks with well-organized droplet inclusions for use in extrusion-based 3D printing. The mechanical properties of the printed PDMS was found to depend on the composition and relative proportion of inner phase, with PEGDA inclusions being especially effective at softening PDMS even at low doses via chemical modulation of the crosslinking network. We then used these insights with our printing setup to design, fabricate and optimize the operation of soft robotic actuators, demonstrating the utility of our droplet-based strategy to impart both form and function into printed objects. Follow-up work could explore other interactions, physical or chemical, between the inner and outer phases at different length scales to generate novel materials with a tailorable functional properties for use in soft robotics and other applications.

2.5. References

1. Murphy, S. V & Atala, A. 3D bioprinting of tissues and organs. *Nat. Biotech* **32**, 773 (2014).

2. Wang, X., Jiang, M., Zhou, Z., Gou, J. & Hui, D. 3D printing of polymer matrix composites: A review and prospective. *Compos. Part B Eng.* **110**, 442–458 (2017).
3. Serra, T., Planell, J. A. & Navarro, M. High-resolution PLA-based composite scaffolds via 3-D printing technology. *Acta Biomater.* **9**, 5521–5530 (2013).
4. Larimore, Z. *et al.* Use of space-filling curves for additive manufacturing of three dimensionally varying graded dielectric structures using fused deposition modeling. *Addit. Manuf.* **15**, 48–56 (2017).
5. Lu, B., Lan, H. & Liu, H. Additive manufacturing frontier: 3D printing electronics. *Opto-Electronic Adv.* **1**, 170004 (2018).
6. Lille, M., Nurmela, A., Nordlund, E., Metsä-Kortelainen, S. & Sozer, N. Applicability of protein and fiber-rich food materials in extrusion-based 3D printing. *J. Food Eng.* **220**, 20–27 (2018).
7. Oxman, N. Variable property rapid prototyping: inspired by nature, where form is characterized by heterogeneous compositions, the paper presents a novel approach to layered manufacturing entitled variable property rapid prototyping. *Virtual Phys. Prototyp.* **6**, 3–31 (2011).
8. Minas, C., Carnelli, D., Tervoort, E. & Studart, A. R. 3D printing of emulsions and foams into hierarchical porous ceramics. *Adv. Mater.* **28**, 9993–9999 (2016).
9. Hardin, J. O., Ober, T. J., Valentine, A. D. & Lewis, J. A. Microfluidic printheads for multimaterial 3D printing of viscoelastic inks. *Adv. Mater.* **27**, 3279–3284 (2015).
10. Ober, T. J., Foresti, D. & Lewis, J. A. Active mixing of complex fluids at the microscale. *Proc. Natl. Acad. Sci.* **112**, 12293–12298 (2015).
11. Nguyen, D. T. *et al.* 3D printing of compositional gradients using the microfluidic circuit analogy. *Adv. Mater. Technol.* **4**, 1900784 (2019).
12. Colosi, C. *et al.* Microfluidic bioprinting of heterogeneous 3D tissue constructs using low-viscosity bioink. *Adv. Mater.* **28**, 677–684 (2016).
13. Liu, W. *et al.* Rapid continuous multimaterial extrusion bioprinting. *Adv. Mater.* **29**, 1604630 (2017).
14. Martin, J. J., Riederer, M. S., Krebs, M. D. & Erb, R. M. Understanding and overcoming shear alignment of fibers during extrusion. *Soft Matter* **11**, 400–405 (2015).
15. Martin, J. J., Fiore, B. E. & Erb, R. M. Designing bioinspired composite reinforcement architectures via 3D magnetic printing. *Nat. Commun.* **6**, 1–7 (2015).
16. Kokkinis, D., Schaffner, M. & Studart, A. R. Multimaterial magnetically assisted 3D printing of composite materials. *Nat. Commun.* **6**, 1–10 (2015).
17. Raney, J. R. *et al.* Rotational 3D printing of damage-tolerant composites with programmable mechanics. *Proc. Natl. Acad. Sci.* **115**, 1198–1203 (2018).
18. Tandon, G. P. & Weng, G. J. The effect of aspect ratio of inclusions on the elastic properties of unidirectionally aligned composites. *Polym. Compos.* **5**, 327–333 (1984).
19. Utada, A. S. *et al.* Monodisperse double emulsions generated from a microcapillary device. *Science (80-.).* **308**, 537–541 (2005).
20. Nelson, A. Z., Kundukad, B., Wong, W. K., Khan, S. A. & Doyle, P. S. Embedded droplet printing in yield-

stress fluids. *Proc. Natl. Acad. Sci.* **117**, 5671–5679 (2020).

21. Yu, Y., Liu, F., Zhang, R. & Liu, J. Suspension 3D Printing of Liquid Metal into Self-Healing Hydrogel. *Adv. Mater. Technol.* **2**, 1700173 (2017).
22. Gupta, M. K. *et al.* 3D printed programmable release capsules. *Nano Lett.* **15**, 5321–5329 (2015).
23. Benson, B. R., Stone, H. A. & Prud'homme, R. K. An "off-the-shelf" capillary microfluidic device that enables tuning of the droplet breakup regime at constant flow rates. *Lab Chip* **13**, 4507–4511 (2013).
24. Style, R. W. *et al.* Stiffening solids with liquid inclusions. *Nat Phys* **11**, 82 (2015).
25. Liang, H., Cao, Z. & Dobrynin, A. V. Molecular dynamics simulations of the effect of elastocapillarity on reinforcement of soft polymeric materials by liquid inclusions. *Macromolecules* **49**, 7108–7115 (2016).
26. Owuor, P. S. *et al.* Nature inspired strategy to enhance mechanical properties via liquid reinforcement. *Adv Mater Interfaces* **4**, 1700240 (2017).
27. Li, X. *et al.* Multimaterial microfluidic 3D printing of textured composites with liquid inclusions. *Adv. Sci.* **6**, 1800730 (2019).
28. Jeong, S. H. *et al.* Mechanically stretchable and electrically insulating thermal elastomer composite by liquid alloy droplet embedment. *Sci. Rep.* **5**, 18257 (2015).
29. Kazem, N., Bartlett, M. D. & Majidi, C. Extreme toughening of soft materials with liquid metal. *Adv Mater* **30**, 1706594 (2018).
30. Markvicka, E. J., Bartlett, M. D., Huang, X. & Majidi, C. An autonomously electrically self-healing liquid metal--elastomer composite for robust soft-matter robotics and electronics. *Nat. Mater.* **17**, 618–624 (2018).
31. Jones, G. *et al.* Photoinduced electron transfer in arylacridinium conjugates in a solid glass matrix. *J Phys Chem B* **111**, 6921–6929 (2007).
32. Madigan, C. F. & Bulović, V. Solid state solvation in amorphous organic thin films. *Phys Rev Lett* **91**, 247403 (2003).
33. Bhagat, A. A. S., Jothimuthu, P. & Papautsky, I. Photodefinable polydimethylsiloxane (PDMS) for rapid lab-on-a-chip prototyping. *Lab Chip* **7**, 1192–1197 (2007).
34. Ma, Z., Wang, X. & Zhang, L. The Effect of Weight Fraction of H-PDMS on the Latex Membrane and the Stability of Composite Emulsion of H-PDMS/Acrylate. *J. Macromol. Sci. Part A* **45**, 1078–1083 (2008).
35. Chen, Y., Gani, A. W. & Tang, S. K. Y. Characterization of sensitivity and specificity in leaky droplet-based assays. *Lab Chip* **12**, 5093–5103 (2012).
36. Helgeson, M. E., Moran, S. E., An, H. Z. & Doyle, P. S. Mesoporous organohydrogels from thermogelling photocrosslinkable nanoemulsions. *Nat. Mater.* **11**, 344–352 (2012).
37. Truby, R. L. *et al.* Soft somatosensitive actuators via embedded 3D printing. *Adv. Mater.* **30**, 1706383 (2018).
38. Zhu, P. *et al.* 4D Printing of Complex Structures with a Fast Response Time to Magnetic Stimulus. *ACS Appl. Mater. \& interfaces* **10**, 36435–36442 (2018).
39. Kotikian, A., Truby, R. L., Boley, J. W., White, T. J. & Lewis, J. A. 3D printing of liquid crystal elastomeric actuators with spatially programed nematic order. *Adv. Mater.* **30**, 1706164 (2018).
40. Kim, Y., Yuk, H., Zhao, R., Chester, S. A. & Zhao, X. Printing ferromagnetic domains for untethered fast-

transforming soft materials. *Nature* **558**, 274–279 (2018).

41. Boley, J. W. *et al.* Shape-shifting structured lattices via multimaterial 4D printing. *Proc. Natl. Acad. Sci.* **116**, 20856–20862 (2019).

CHAPTER 3: BIOPRINTING MULTI-LAYER HYDROGELS FOR INTESTINAL EPITHELIAL TISSUE ENGINEERING

3.1 Introduction

The gastrointestinal (GI) tract is not only responsible for digestive functions and absorption of nutrients, but also plays a key role in mediating the absorption or other bioactive compounds (e.g. drugs, gut flora metabolites) and shaping host immune responses[1,2]. As such, it has come under increased scrutiny for potentially contributing to areas of human health far beyond the GI tissue itself. This has been demonstrated in the case of cardiovascular health[3–7] and in neurodegeneration[8–13], although the exact molecular mechanisms and causal links have yet to be studied in detail. While *in vivo* studies using animals such as gnotobiotic mice have been indispensable in observing associations between the gut and wider aspects of host health, *in vitro* models of the GI tract are highly coveted due to their relative simplicity and relative ease of use. Due to the absence of crosstalk and other convoluting factors associated with normal host physiology, simplified *in vitro* models of the gut epithelium have immense utility in facilitating molecular mechanistic studies that provide clinically-useful insights into the manifold ways in which the GI tract regulates human health. This is especially so considering the rising global health burden of not only GI-related chronic inflammatory conditions (e.g. inflammatory bowel disease, Crohn's disease and ulcerative colitis)[14,15], but also that of cardiovascular disease[16] and neurological disorders[17–19] and GI-related chronic inflammatory conditions.

Early *in vitro* models that use transformed cell lines such as Caco-2 or HCT116 have steadily been replaced by *in vitro* primary-derived intestinal epithelial tissues as the latter is demonstrably capable of producing models that successfully recapitulate physiological functions, model GI disease pathophysiology and studying drug responses[20–22]. Models engineered from *in vitro* primary-derived intestinal epithelial tissues rely heavily on ECM materials such as Matrigel or collagen type I to enable successful cell proliferation and differentiation, whether as 3D organoids[23,24] or 2D surface monolayers[25–27]. Typically, Lgr5 stem cell-rich crypts are harvested from animals or patients and are then expanded *in vitro* to form organoids by

suspending within ECM, typically Matrigel due to its similarity with basement membrane matrix, or plated on ECM substrates (e.g. collagen type I or Matrigel) to form a continuous surface monolayer. Nevertheless, these ECM materials possess extremely low stiffnesses (<1 kPa) and slow gelation kinetics especially in the case of collagen type I, which limit their ease of handling in bioengineering approaches. The same problem is more or less true for other recently developed scaffold materials derived from fibrin[28] and polyethylene glycol (PEG)[29] as these material systems were specifically engineered to match the low stiffness of Matrigel or native intestinal epithelium ECM.

Here, we explored the use of agarose in conjunction with Matrigel for *in vitro* intestinal epithelial engineering. By stacking layers of Matrigel and agarose (which we coin "dual layers"), we were able to support the growth of intestinal organoids *in vitro*. Analysis of organoid growth and morphology using bright field and immunofluorescence microscopy reveal the presence of highly elongated organoids grown on dual layers marked by extended proliferative budding structures similar to intestinal crypts *in vivo*. Using these findings, we also report a protocol for bioprinting core-shell filaments consisting of Matrigel and agarose to produce *in vitro* intestinal epithelial tubes that are easy to handle due to the mechanical integrity of agarose. We also used this protocol to generate thin sub-millimeter diameter Matrigel filaments suspended with organoids that are not only capable of producing elongated organoids, but also hybrid 2D-3D intestinal epithelial tissue morphologies that exhibit apical-out epithelial monolayers as well as crypt structures.

3.2 Materials and Methods:

3.2.1. Reagents:

DMEM/F12 with HEPES, IntestiCult™ Organoid Growth Media (mouse), Mouse intestinal organoids and Gentle Cell Dissociation Reagent were purchased from StemCell Technologies. 30 wt.% BSA solution was purchased from VWR. Matrigel, growth factor-reduced Matrigel® (#356231) and Costar 96-well plates

(#3595) were purchased from Corning. UltraPure™ low melting point agarose (#16520100) was purchased from Invitrogen.

3.2.2. Intestinal Organoid Culture and Expansion:

Mouse intestinal organoids were purchased from StemCell Technologies in cryovials. To thaw the organoids from cryopreservation, the vials were warmed in a water bath at 37˚C until the contents of the cryovial have mostly liquefied. The contents were promptly mixed with 5 mL of 1 wt.% BSA solution in DMEM and centrifuged at 200 x RCF for five minutes. The organoids were then resuspended in 30 µL of 1:1 ratio of Matrigel and IntestiCult media per well, pipetted onto 4 wells within 24-well tissue culture plates, and incubated at 37˚C for 10 minutes to allow polymerization of Matrigel. 700 µL of IntestiCult is then added into the well, and the media was exchanged every two days.

Wells were selected for subculturing upon organoids exhibiting pronounced budding/crypt-like structures (typically within 5-9 days). Media was aspirated before introducing 1 mL of cold Gentle Cell Dissociation Reagent into these wells. The contents of the wells were then pipetted up and down 20 times to break up the Matrigel before being transferred into a 15 mL conical tube. The tube containing the resuspended organoids were then mechanically dissociated further by inverting for 10 minutes before being centrifuged at 300 x RCF for five minutes. The supernatant was discarded before resuspending the organoids in 10 mL of DMEM/F12 and centrifuging at 200 x RCF for five minutes. All centrifugation steps were performed at 4˚C. The supernatant was then discarded, leaving behind a pellet consisting of dissociated organoids that could be sub-cultured for subsequent regular organoid culture maintenance or for experiments.

3.2.3. Hydrogel preparation and organoid growth experiments in Transwell inserts

Agarose solution was prepared by dissolving the appropriate weight percent of agarose into 1x PBS. In order to ensure the osmotic pressures are in the expected range when constituting 1x PBS agarose, DI water was added to replenish any volume lost due to evaporation. For agarose conditioning, agarose pre-gel

solution was mixed at a 1:1 ratio with IntestiCult media to form a final agarose concentration of 1.5 w/v% agarose. Once the agarose solution is properly constituted, it was added into the Transwell insert at a volume corresponding to a desired layer thickness (~32 µL per mm thickness) and allowed to undergo gelation for 10 minutes at room temperature.

Following this, organoid-laden Matrigel suspension was prepared by mixing Matrigel in a 1:1 ratio with organoid-laden (~800 organoids per mL) IntestiCult media prior to being pipetted onto the Transwell insert for a 24-well plate. A 0.5mm-thick layer was formed in the Transwell insert by pipetting the appropriate volume of the Matrigel mixture either on top of the agarose or on the bare Transwell, and the Matrigel was then allowed to undergo gelation for 10 minutes at 37˚C. Following this, 700 µL of IntestiCult growth media was added to the bottom compartment while 100 uL of IntestiCult growth medium was added to the top (Transwell) compartment, thus completing the setup. The media in the bottom compartment was replaced every 2 days, while the top compartment was left untouched throughout the culture to avoid washing away the organoids suspended in Matrigel.

3.2.4. Growth quantification

Images were taken using a Leica DMi8 microscope, and all images were analyzed using ImageJ. Growth was assessed by measuring the projected area of the organoids in select locations in each well over the course of the culture. The measured areas from days 3, 5, 7, 9, 11 and 13 were normalized by the projected area of organoids on day 1. Organoid longest bud lengths at various days were determined by tracing the longest budding structure of each organoid through its center to where it meets the darkened rounded core of the organoid. In the case where organoids displayed a high degree of blebbing and darkening to the point where no viable budding structures could be identified, longest bud length was determined by measuring the length of any darkened structures that resembled typical budding structures.

3.2.5. Immunofluorescent Staining:

Solutions prepared for use in immunofluorescent staining include 10% Formalin, permeabilization/washing solution (0.2 % Triton X-100 + 0.05 % Tween-20 in PBS), blocking solution (5% goat serum + 5% BSA in washing solution), primary antibody solution (rabbit anti-mouse Lysozyme monoclonal antibody, MA5-32154, 1:50 dilution in blocking solution) and secondary antibody solution (anti-rabbit goat Alexa Fluor 594 secondary antibody, A32740, 1:500 dilution in blocking solution).

Prior to fixing, organoids were suspended in cold PBS for up to 10 minutes to ensure dissociation of Matrigel. Organoids were then fixed and permeabilized using 10% Formalin for 20 minutes and washing solution for 20 minutes, respectively. Following this, organoids were blocked with 5% goat serum + 5% BSA in washing solution (0.2 % Triton X-100 + 0.05 % Tween-20 in PBS) overnight at 4˚C. Next, organoids were incubated with primary antibodies solution overnight at 4˚C, followed by washing 3 times with washing solution. Following this, secondary antibody solution was added to the cells for 1 hour at room temperature, followed by 3 more washing steps. Finally, Hoechst 33342 and optional phalloidin stain was added to the cells. Organoids were then transferred to a glass chamber slide for subsequent confocal imaging. For EdU staining, Click-iT EdU imaging kits were used following the manufacturer's protocols.

3.2.6. Core-shell Filament Printing Setup

A coaxial printhead assembly was built using a glass capillary (side length of 0.4 or 1.05 mm), a male-to-male luer connector and a custom 3D-printed nozzle (outlet diameter of 2.5 or 4.5 mm). The 3D-printed nozzle was designed on SolidWorks and made using Formlabs Form 3B SLA printer with Surgical Guide resin. The glass capillary was centered inside the barrel of the 3D-printed nozzle prior to being glued to a male-to-male luer connector to form a watertight seal and complete the coaxial printhead assembly. Polyethylene tubing (16 or 27.5 Birmingham needle gauge) was used to connect the coaxial printhead assembly to the bioink feeds.

Agarose (3% w/v) in the liquified pre-gel state was added to a 10-mL syringe. The syringe was subsequently wrapped in a syringe heating jacket (New Era Pump Systems) set at 40˚C and loaded onto a syringe pump. The syringe was connected via 16-gauge polyethylene tubing to the 3D-printed nozzle and the tubing was quickly filled with agarose prior to setting the flow rate at between 0.3 to 0.4 mL/min to produce filaments. Upon verification of steady-state agarose filament production, organoids-laden Matrigel suspension was added into a 1-mL syringe which was then loaded onto a separate syringe pump whose flow rate was set to match the velocity of the agarose layer. Core-shell agarose filaments were collected in a 60mm-wide Petri dish and at 37˚C for 10 minutes upon completion of printing. Immediately prior to adding 6mL media for 12-day culture, the filaments were optionally sealed with 3% w/v. agarose at the ends to prevent unintended dislodging of the Matrigel core mid-culture. To trigger dislodging of Matrigel core, ends were cut/left open and media was lightly perfused to impinge upon the Matrigel core until it slides out. All filaments/cores were cultured in 6 mL of IntestiCult media for 12 days, with 3mL of the media being exchanged once at day 6.

3.2.7. Statistical Analysis

Statistically significant differences in organoid projected area and longest axis were assessed using nonparametric Mann-Whitney U-test in GraphPad Prism when p-values under 0.05. Annotations used include: ns = not significant, * = $p < 0.05$, ** = $p < 0.01$, *** = $p < 10^{-3}$, **** $p < 10^{-4}$.

3.3 Results

3.3.1 Elongated organoids on agarose-Matrigel dual layers

To test the compatibility of agarose with Matrigel, we used a Transwell insert setup to compare the growth and expansion of murine intestinal organoids when cultured in Matrigel versus a dual layer setup featuring a layer of agarose atop the organoid-laden Matrigel layer (Figure 1A). Since, agarose is water-permeable and allows the transport of nutrients and growth factors much like the track-etched membrane on the bottom of the Transwell insert, we hypothesized that dual layers should support cell/tissue culture much the same

its Matrigel counterpart, so long as agarose is constituted to resemble physiological osmolality. Timelapse imaging over 13-days of culture revealed that both Matrigel-only and dual layer trials exhibit standard intestinal organoids growth behavior. Specifically, organoids initially produce Lgr5 stem cell-rich budding structures and gradually develop darkened cores that then overtake the budding structures[23]. By day 13, many of the organoids grown in the Matrigel-only control exhibited a low number of buds and predominantly consisted of the darkened cores. At the same time, within the dual layer experiments, we noticed a subset of organoids where one or several budding structures grew far beyond (> 500 μm) the bounds of the darkened core, resulting in a highly elongated and snaking appearance in contrast to the more rounded appearance of regular organoids (Figure 1B). Overtime, these highly elongated buds also begin to round out and form darkened cores, as seen in the day 7 and 13 images.

Analyzing the bright field timelapse images, the growth kinetics of dual layer organoid cultures shows broad similarity with the Matrigel-only control at the start of the 13-day culture. Starting at day 9, however, the median fold-increase of the dual layer setup begins to overtake that of the Matrigel-only control. By day 13, median fold-increase was 34.4-fold (n = 22) vs 16.5-fold (n = 23) in the dual layer versus Matrigel-only control, respectively (Figure 1C). The same trend is present when analyzing the longest organoid bud length. In both dual layers and Matrigel-only controls, the bud length increases steadily and peaks at day 11, before falling off at day 13. Dual layers generate comparatively shorter buds compared to the Matrigel-only controls up to day 9, but overtake the Matrigel-only experiments starting in day 11, with the median longest bud length in dual layers exceeding that of the Matrigel-only experiments by 34% and 91% at days 11 and 13, respectively (Figure 1D). This is further evidenced by the distribution of longest bud lengths at day 11, with 25.6% organoids in dual layers longest bud lengths being greater than 500 μm compared to 12.5% in Matrigel-only (Figure 1E). Altogether, these results indicate that addition of the agarose layer in the Transwell setup is not only compatible with Matrigel for intestinal organoid culture, but helps to induce highly proliferative organoid phenotypes that can outperform Matrigel-only cultures.

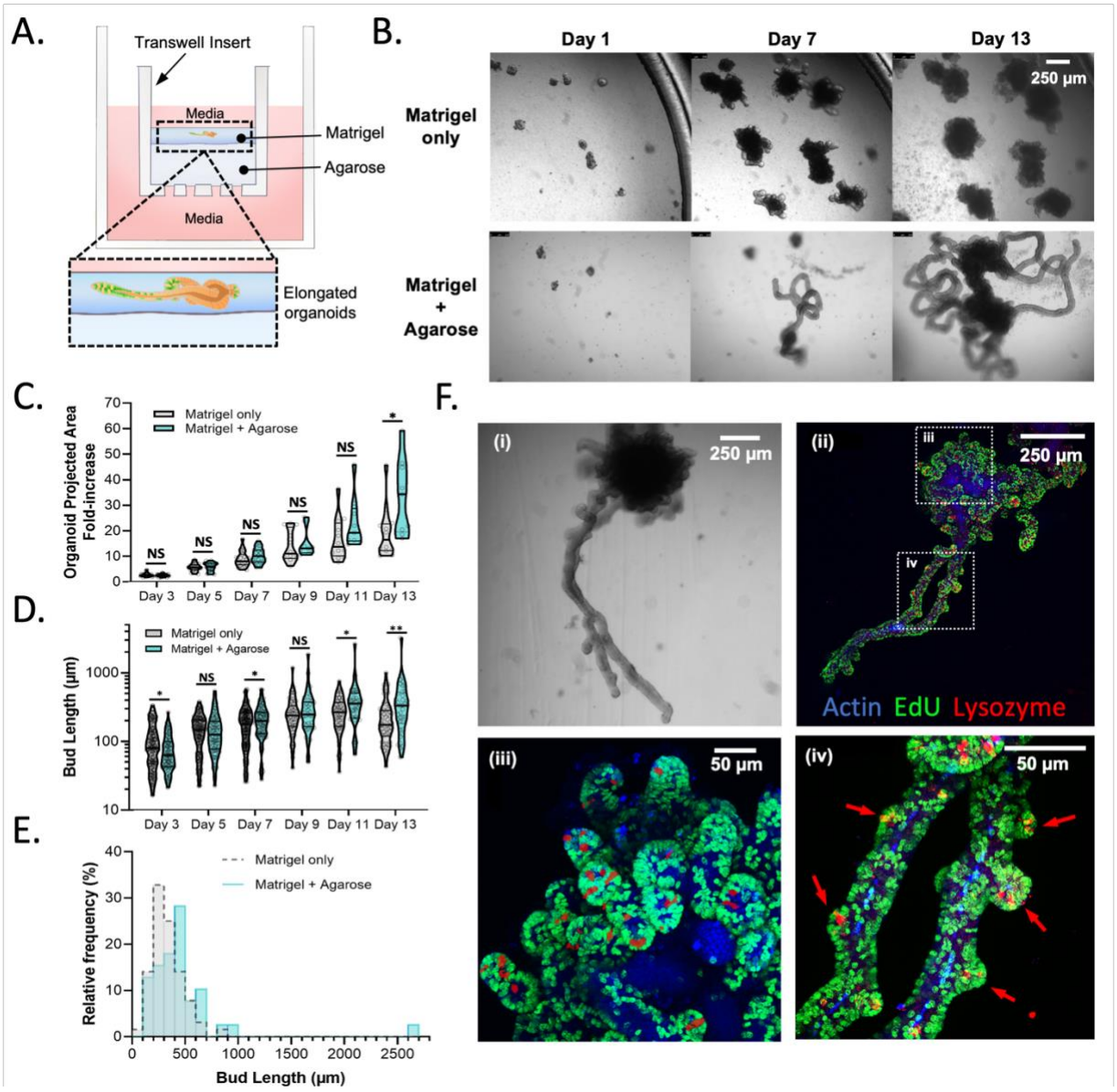

Figure 1. Agarose-Matrigel dual layers promote intestinal organoid growth and elongation *in vitro*. (A) Schematic of the in vitro culture of intestinal organoids using agarose-Matrigel dual layers in a Transwell setup. Matrigel layer: 0.5mm; Agarose layer: 3mm, 1.5% w/v. (B) Timelapse images of organoids grown in Matrigel only versus agarose-Matrigel in a Transwell setup. Scale bars: 250 µm. (C) Violin plots comparing the organoid growth (projected area increase) and (D) longest bud length in Matrigel-only versus dual-layer cultures. (E) Histograms of longest bud lengths at day 11. (F) Immunofluorescence images of intestinal organoids with elongated morphologies. EdU (green) was used to stain cells undergoing proliferation and was pulsed for 24-hours in all the images. Actin (blue) was used to stain cell bodies. Lysozyme (red) was used to stain Paneth cells. Parts ii – iv have actin stained in the blue channel and EdU in the green channel. The red arrows in part iv indicate regions stained positive for Lysozyme and are forming new budding structures. * $p < 0.05$, ** $p < 0.01$, *** $p < 0.001$ and **** $p < 0.0001$, respectively, using Mann-Whitney U-test. All violin plots show the median (solid line) and the 25th & 75th percentiles (dashed lines).

Immunofluorescence staining revealed that the highly elongated budding structures contain a high proportion of EdU positive cells (after a 24-hour pulse) and a lesser number of Paneth cells localized in regions where new budded structures are emerging as evidenced by the curvature. (Figure 1F) In terms of

apical-basal polarity, F-actin staining shows the apical surface facing the internal volume of the organoid, consistent with the apical-in polarity of regular intestinal organoids (Figure 2). These results indicate that the highly elongated budding structures are reminiscent of regular Lgr5 stem cell-rich budding structures seen in regular intestinal organoids. Their elongated appearance compared to regular budding structures is due primarily to their relatively high level of proliferation. At the same time, the presence of Paneth cells along the long budding structure is likely indicative of the production of new Lgr5 stem cell-rich budding structures, similar to crypt fission events *in vivo* that lead to formation of new crypts[30].

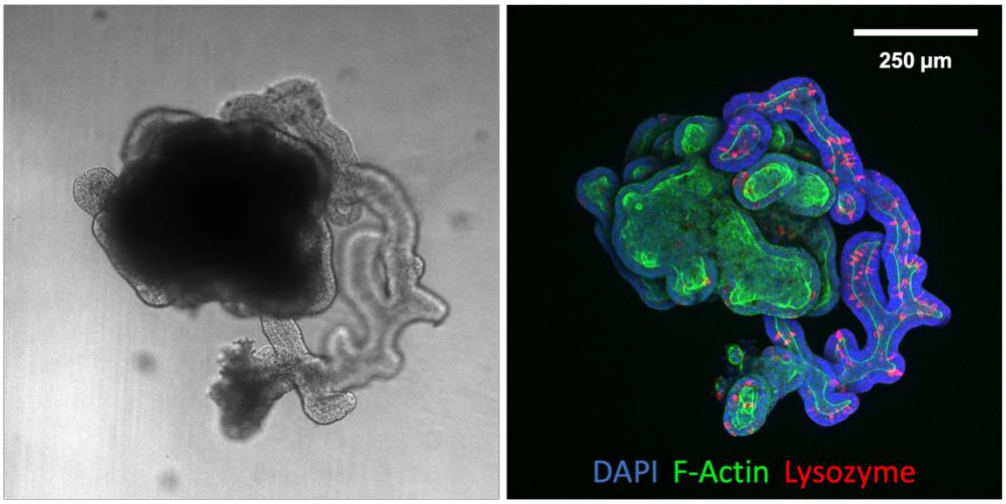

Figure 2. Bright-field and immunofluorescent staining of elongated organoids showing apical-in polarity of cells, with F-actin as the apical marker. Blue = actin, Green = EdU, Red = Lysozyme. Scale bar = 250 µm.

3.3.2 Agarose layer properties directly influence intestinal organoid growth in dual layers

To elucidate the means by which the addition of agarose in the dual layer organoid culture promotes elongated morphology and organoid growth, we repeated the Transwell growth experiments while making changes in agarose thickness and concentration. Analysis of organoid growth revealed that thinner agarose layers provide a significant improvement as early as day 3 in the case of 0.5mm. At day 7, the 0.5mm dual layer had produced a median fold-change of 15.61 (n = 16) versus 8.05 (n = 11) from the Matrigel-only control. This is particularly striking considering how parity with the Matrigel-only organoid culture was only achieved by the dual layer in day 9 as shown in Figure 1 when the agarose layer was 3mm. Similarly, addition of thicker agarose layers (1.0 and 3.0mm) also results in an improvement in organoid growth over

the Matrigel-only culture, but only at later days (i.e. day 7) (Figure 3A). When comparing the distribution of longest bud lengths, a similar trend was observed with the thinnest agarose layer giving a comparatively early boost to longest bud length at day 5, in contrast to thicker agarose layers which did so at day 7. The 1.0mm agarose layer produced the highest median longest bud length of 229.7 μm, which is 29.3% higher than 177.7 μm from Matrigel-only experiments (Figure 3B). Comparing the histograms of longest bud lengths at day 7 reveals a consistent right shift when agarose layer is added (Figure 3C).

Changing the agarose permeability had a similar effect to with varying the thickness. When agarose concentration was decreased from 1.5 to 0.5 % w/v, it conferred an early benefit to the organoid growth ; quantitatively, the 0.5% w/v produced a 3.15-fold change in organoid projected area versus 2.57-fold from the control at day 3. Strikingly, an early improvement of similar magnitude (3.37-fold) was also seen when increasing the agarose concentration from 1.5 to 3.0% w/v. In subsequent days, however, the early improvement from 3.0% w/v agarose over the Matrigel-only culture all but disappeared, while lower agarose concentrations produced a sustained improvement in organoid growth throughout the 7-day culture (Figure 3D). A similar trend is seen when analyzing the longest bud length where the 0.5% w/v agarose provided an early and sustained improvement, reaching a maximum median longest bud length of 267.6 μm at day 7 compared to 232.2 μm from the 3.0% w/v dual layers (Figure 3E). Comparing the distribution of longest bud lengths show that 0.5% w/v agarose has a clear lead over the more concentrated (or less permeable) agarose dual layers (Figure 3F). Taken together, thinner and more permeable agarose layers confer an earlier benefit to organoid growth than thicker and less permeable layers. This may be attributed to earlier breakthrough times for the diffusion of growth factors/nutrients to the organoid-laden Matrigel layer.

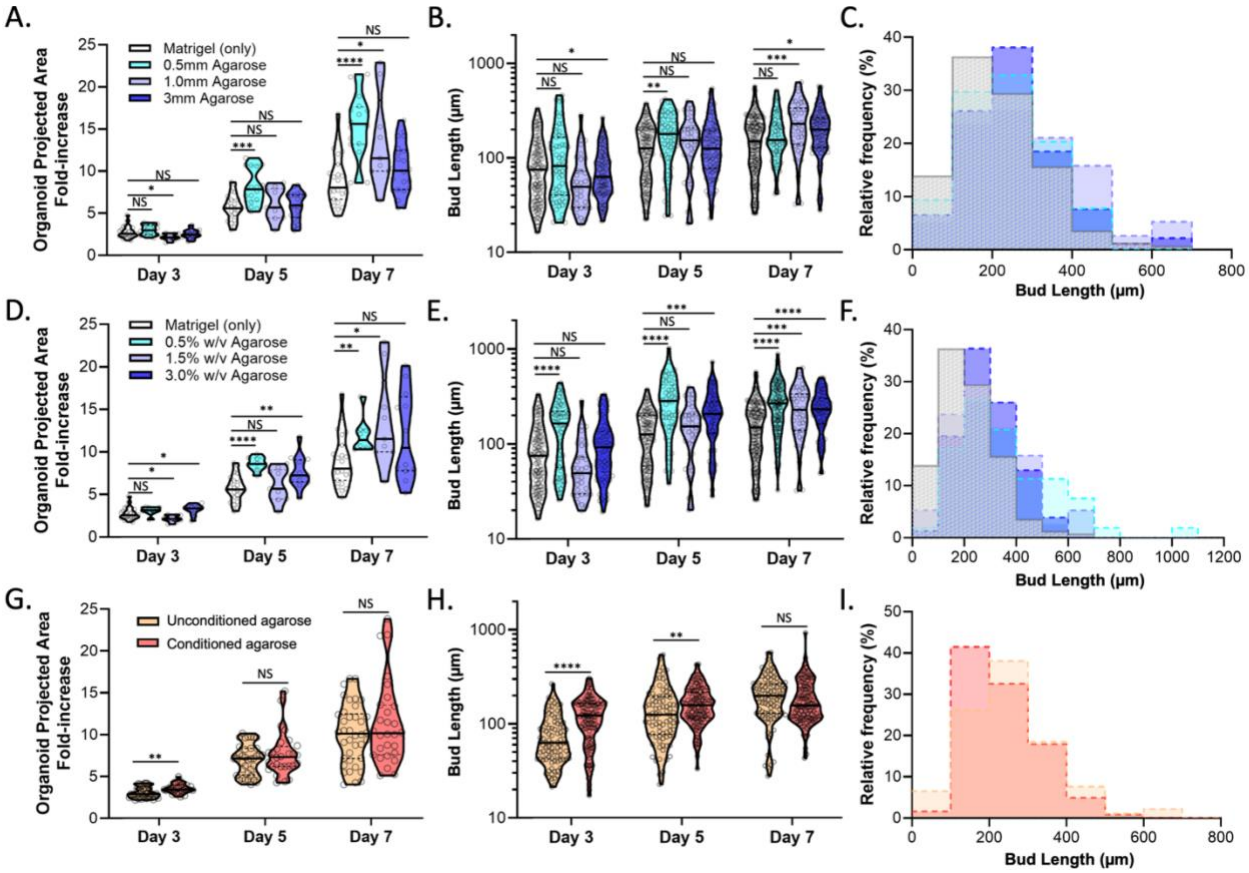

Figure 3. Adjusting agarose layer changes the growth kinetics of intestinal organoids. (A) Graphs comparing the 7-day organoid growth (projected area increase) in Matrigel-only versus dual layer cultures with 0.5mm, 1.0mm and 3.0mm thicknesses of agarose layer. (B) Graph comparing the bud lengths in Matrigel-only versus dual-layer cultures with 0.5mm, 1.0mm and 3.0mm thicknesses of agarose layer. (C) Histograms of bud length at day 7 for different agarose layer thicknesses. All agarose used in parts A-C are 1.5% w/v. (D) Graphs comparing the 7-day organoid growth (projected area increase) in Matrigel-only versus dual layer cultures with 0.5, 1.5 and 3.0% w/v agarose. (E) Graph comparing the bud lengths in Matrigel-only versus 0.5, 1.5 and 3.0% w/v dual-layer cultures. (F) Histograms of bud length at day 7 for different agarose concentrations. All agarose used in parts D-F have a thickness of 1mm. (G) Graphs comparing the 7-day organoid growth (projected area increase) in dual layers with unconditioned agarose (prepared using PBS) versus conditioned agarose (prepared using growth media). (H) Graph comparing the distribution of longest buds in Matrigel-only versus 0.5, 1.5 and 3.0% w/v dual-layer cultures. (I) Histograms of longest bud length at day 7 for different agarose concentrations. All agarose used in parts G-I have a thickness of 3mm and a concentration of 1.5% w/v. * $p < 0.05$, ** $p < 0.01$, *** $p < 0.001$ and **** $p < 0.0001$, respectively, using Mann-Whitney U-test. All violin plots show the median (solid line) and the 25th & 75th percentiles (dashed lines).

Next, we hypothesized that the initial concentration of growth factors/nutrients in the proximity of the organoids in the Matrigel layer plays a critical role in the successful growth of organoids in dual layers. To produce a higher initial concentration, we conditioned the agarose layer by mixing it with intestinal organoid growth media at a 1:1 ratio prior to plating. We then repeated the Transwell experiments comparing regular dual layers (or unconditioned) with conditioned dual layers over a 7-day culture.

Organoid projected area measurements revealed a boost conferred by conditioning agarose as early in day 3 (3.45-fold versus 2.91-fold), and that this boost effectively disappears in subsequent days (Figure 3G). A similar trend is seen in the longest bud length data where the conditioned agarose dual layers saw an improvement over its unconditioned counterpart between days 3-5, but no advantage by day 7 (Figure 3H), which is corroborated by largely overlapping histograms of the longest bud lengths at day 7 (Figure 3I). These results indicate that the initial concentration of growth factor/nutrients in proximity to the organoids influences early growth kinetics.

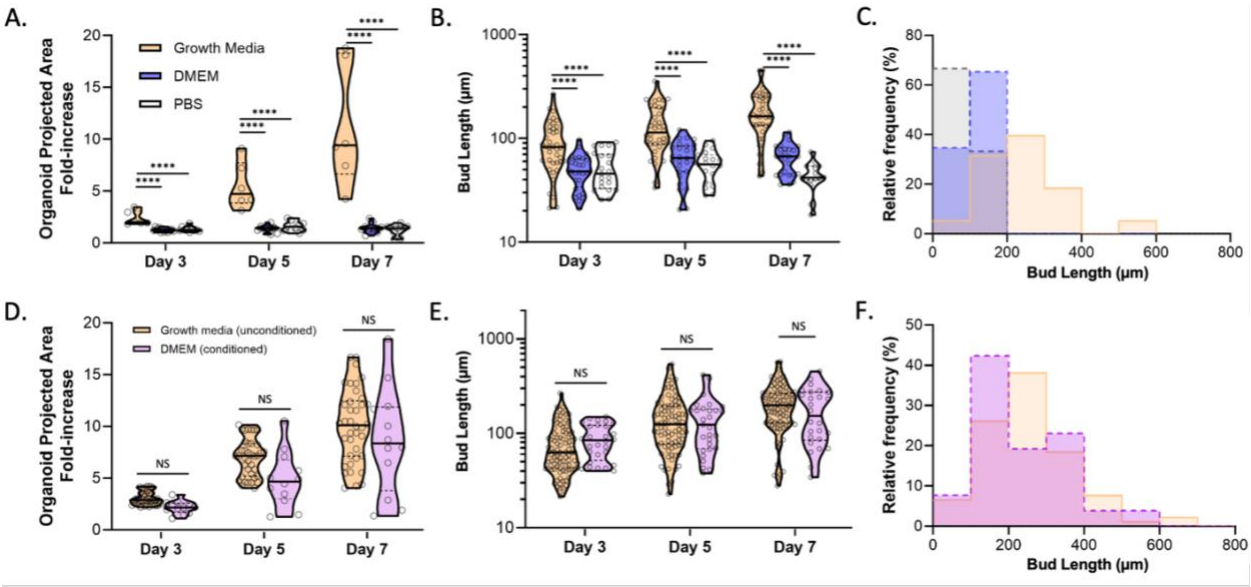

Figure 4. Transwell top compartment media composition influence organoid growth and prevalence of elongation phenomenon in intestinal organoids grown in agarose-Matrigel dual layers. All dual layers used have a thickness of 3mm and a composition of 1.5% w/v. (A-C) Graphs comparing the 7-day organoid growth (projected area increase) and longest bud length when different top compartment media is used. Histogram shows the longest bud length distribution at day 7. (D-F) Graphs comparing the organoid growth (projected area increase) and longest bud length with different combinations of agarose conditioning and top compartment media composition. Histogram shows the longest bud length distribution at day 7. * $p < 0.05$, ** $p < 0.01$, *** $p < 0.001$ and **** $p < 0.0001$, respectively, using Mann-Whitney U-test. All violin plots show the median (solid line) and the 25th & 75th percentiles (dashed lines).

Next, we devised experiments where we swapped organoid growth media in the top compartment for DMEM/F12 and PBS, hypothesizing that the growth media on top was responsible for providing a sufficient amount of growth factors initially. Analysis of organoid projected area and longest bud length revealed that organoids grown in dual layers where the top compartment had DMEM/F12 or PBS instead of growth factor-containing media failed to grow altogether (Figure 4A-C), thus supporting our hypothesis. Strikingly,

conditioning the agarose in dual layers where the top compartment is growth factor-free (i.e. DMEM/F12) provided full recovery of organoids, as exhibited by its parity with regular dual layer cultures (growth media on top, unconditioned agarose) (Figure 4D-F). Taken together, the initial concentration of growth factors is a key factor in successful organoid expansion in the Transwell dual layer setup, and that transport of growth factors from the bottom compartment alone through the agarose layer is capable of supporting organoid expansion for the remainder of culture since the top compartment remained untouched throughout the 7 or 13-day cultures.

3.3.4 Bioprinting Matrigel-agarose core-shell filaments

Having established how agarose complements Matrigel for intestinal organoid culture, we then established a protocol for bioprinting using these materials. Previous work from our group demonstrated the limited printability of blended Matrigel-agarose composite bioinks[31]. As such, we decided on a core-shell filament strategy in which an agarose layer surrounded an organoid-laden Matrigel core, thus providing the mechanical integrity of agarose while keeping the Matrigel layer intact (Figure 5A). The cornerstone of this technique is the continuous extrusion and gelation of agarose within the nozzle through tight control over agarose temperature and flow rate, which are chosen to ensure ideal flow/extrusion behavior. Specifically, agarose is fed into the nozzle as a warm pre-gel liquid where it flows around the inner glass capillary. In the course of the flow through the nozzle, agarose cools and turns into a viscoelastic gel as it exits the nozzle, thus resulting in a relatively homogeneous and smooth agarose filament in contrast to the rough and chunky texture from our previous work. As the agarose filament emerges from the nozzle, an internal cavity/channel corresponding to the shape of the inner glass capillary is formed that is subsequently filled by flowing Matrigel bioink.

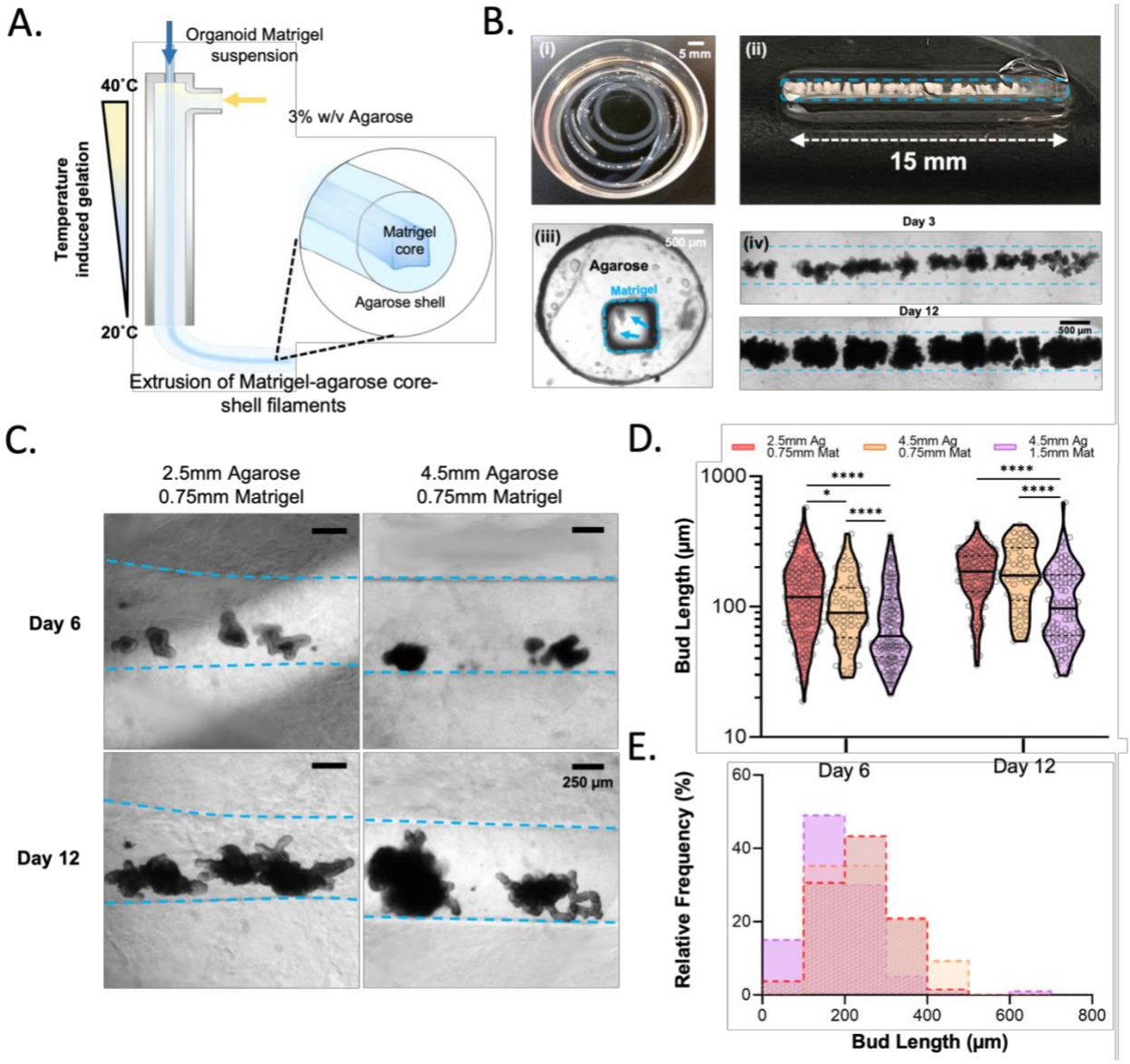

Figure 5. Bioprinting Matrigel-agarose core-shell filaments. (A) Schematic of printing process for Matrigel-agarose core-shell filaments. (B) Images of Matrigel-agarose filaments. Part (i) shows spools of filament in a 60mm diameter petri dish; part (ii) shows a 15mm long filament with dense organoid suspension (~4000 organoids/mL) at day 12, with the right end sealed up with additional agarose post-printing; part (iii) shows the cross section of a Matrigel-agarose filament, with Matrigel outlined in blue; Blue arrows indicate the organoids inside Matrigel core. part (iv) shows micrographs of the organoids grown in part (ii). Scale bar is 500 µm. (C) Timelapse images of organoids grown in different filaments. Interface between agarose and Matrigel shown in dotted lines. (D) Violin plots of bud lengths for different Matrigel-agarose filaments. (E) Histogram showing distribution of bud lengths at day 12. * $p < 0.05$, ** $p < 0.01$, *** $p < 0.001$ and **** $p < 0.0001$, respectively, using Mann-Whitney U-test. All violin plots show the median (solid line) and the 25th & 75th percentiles (dashed lines).

Agarose filaments produced through this method exhibit high optical transparency, display high shape fidelity and exhibit sufficient mechanical integrity for ease of handling. As seen in Figure 5B, centimeter scale core-shell filaments can be produced while cells suspended in the Matrigel core are capable of

expanding and self-organizing to the point where it is visible to the naked eye. Inspecting the filament's cross section, we see that there is a defined core channel wherein organoid-laden Matrigel is located, and that this core-channel takes on the shape of the inner capillary, which in this case is an 800 μm x 800 μm square. With sufficiently high cell seeding density, filaments can achieve nearly full coverage of the core volume and create continuous epithelial tubes. Compared to other reports of tissue engineering with agarose where agarose is first micropatterned before being loaded with Matrigel[32], our filament printing strategy is capable of producing Matrigel-agarose filaments in one step without the need to multiple pattern transferring steps.

Throughout the duration of 12-day culture, the agarose shell remained stable with no sign of mechanical damage or distortion, thus maintaining a consistent boundary/interface with the Matrigel core. Timelapse images of intestinal organoids revealed growth and expansion that is consistent with regular organoids in that budding structures form in addition to darkened core domains (Figure 5C). We compared the organoid growth in filaments with different geometries (e.g. agarose shell and Matrigel core thickness). Longest bud length data shows that thin Matrigel cores are more conducive to organoid growth than thicker cores, with 0.5mm diameter cores producing median longest bud lengths that are 86% greater than in 1.5mm diameters at day 12 (185.9 μm versus 97.1 μm) (Figure 5D-E). Indeed, close inspection of organoids in thick-core filaments reveals poorer growth at the center of the filaments away from the edges over the course of 12-day culture. Organoids located furthest away from the edge of the filament and from the agarose-Matrigel interface exhibit limited expansion and produce fewer pronounced budding structures compared to organoids at the edge (Figure 6). Interestingly, the distribution of longest bud lengths in the bioprinted filaments, regardless of geometry/thickness, is markedly lower than those observed in the Transwell setup at similar time points. We attribute this to the difference in layout between the Transwell setup and the core-shell filaments, with the former having two separate media compartments, one of which is immediately adjacent to the Matrigel layer containing the agarose.

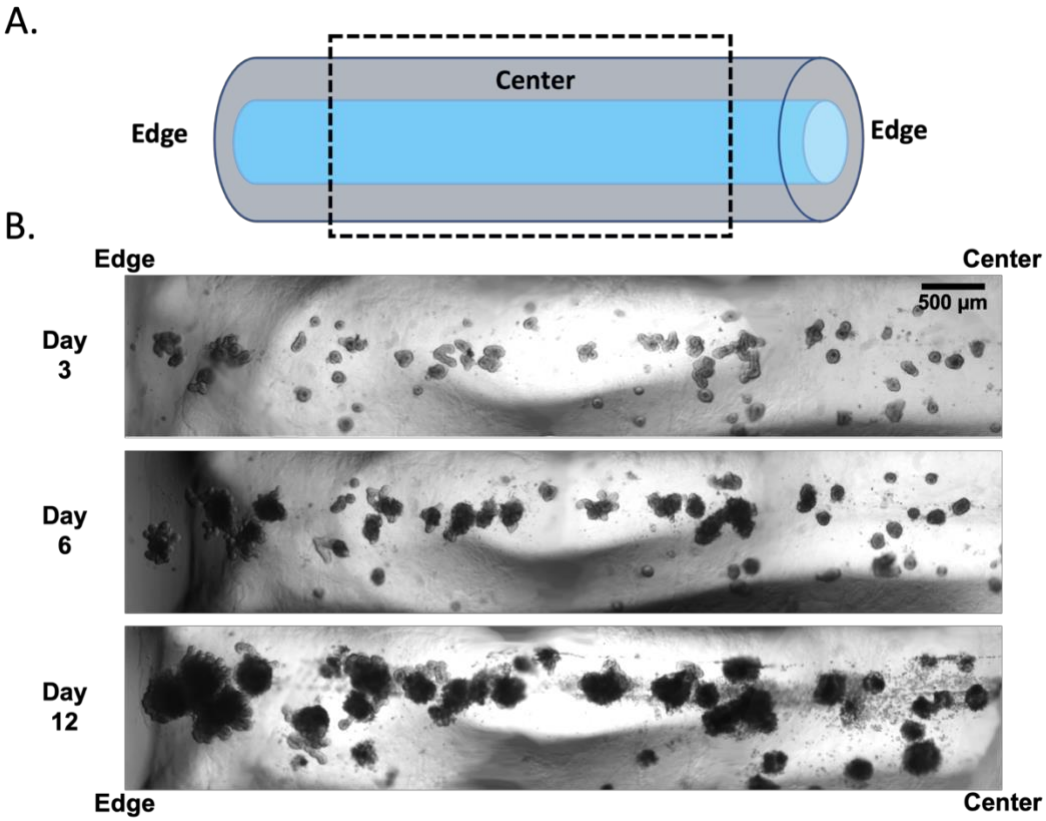

Figure 6. Heterogeneous growth of intestinal organoids in core-shell filaments with thick cores (1.5 mm) over 12-day culture. (A) Schematic of core-shell filaments illustrating edge versus center regions of the filament. (B) Bright-field timelapse images of organoids grown in Matrigel-agarose core shell filaments.

3.3.4 Dislodging Matrigel cores from core-shell filaments

We noticed during the preparation of Transwell dual layers that Matrigel adheres poorly onto an agarose surface and that light mechanical agitation is often sufficient to successfully displace Matrigel. The same is true in the Matrigel-agarose core-shell filaments wherein Matrigel cores could be dislodged from the agarose sheath when subjected to sufficient agitation of the liquid media, whether intentionally or otherwise. Thus, in addition to producing core-shell filaments, our bioprinting protocol is capable of producing thin Matrigel filaments (< 1mm diameter) that took on the shape of the inner glass capillary used during the printing process. Although dislodged filaments freely float and flex within the culture media, they roughly retain their original shape over the course of culture (Figure 7A).

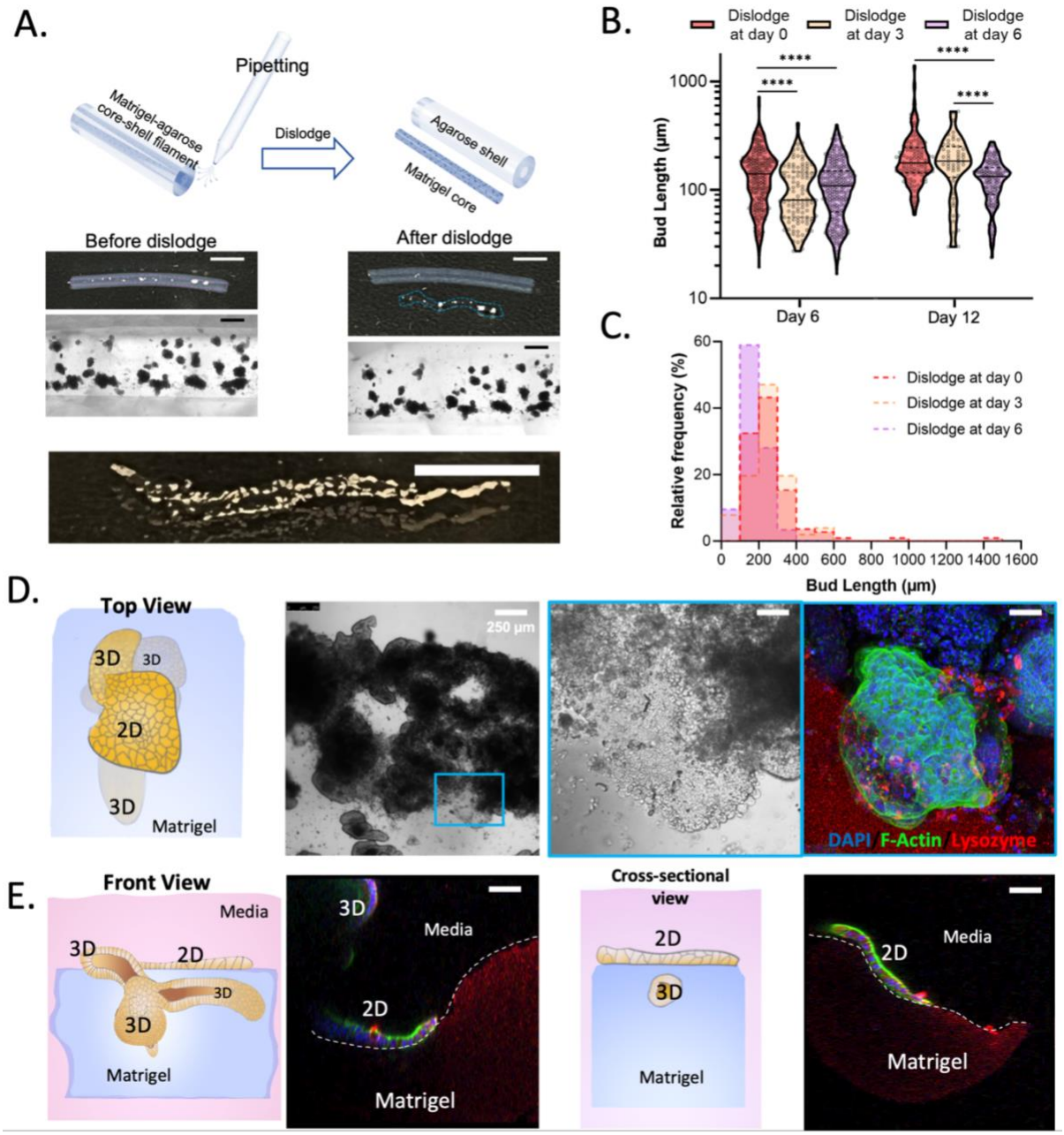

Figure 7. Dislodged Matrigel filaments support intestinal organoid culture and 2D-3D hybrid morphologies. (A) Schematic and images of the Matrigel core dislodging process. Micrographs show the organoids in the Matrigel core at day 6 before and after dislodging. Scale bars are 5 mm and 250 µm for macroscopic images and micrographs, respectively. (B) Violin plots comparing the bud lengths of organoids in filaments dislodged at different times. (C) Histograms of bud lengths at day 12. (D) Top-view of hybrid 2D-3D organoid morphologies on dislodged Matrigel filaments. Scale bars = 50 µm unless otherwise noted. DAPI (blue) was used as nuclear counterstain; F-actin (green) was used to mark the apical surface of cells that typically face inwards. Lysozyme (red) was used to stain Paneth cells. (E) Orthogonal views (front and cross-sectional) of 2D-3D organoid morphologies. Scale bars = 50 µm * $p < 0.05$, ** $p < 0.01$, *** $p < 0.001$ and **** $p < 0.0001$, respectively, using Mann-Whitney U-test. All violin plots show the median (solid line) and the 25th & 75th percentiles (dashed lines).

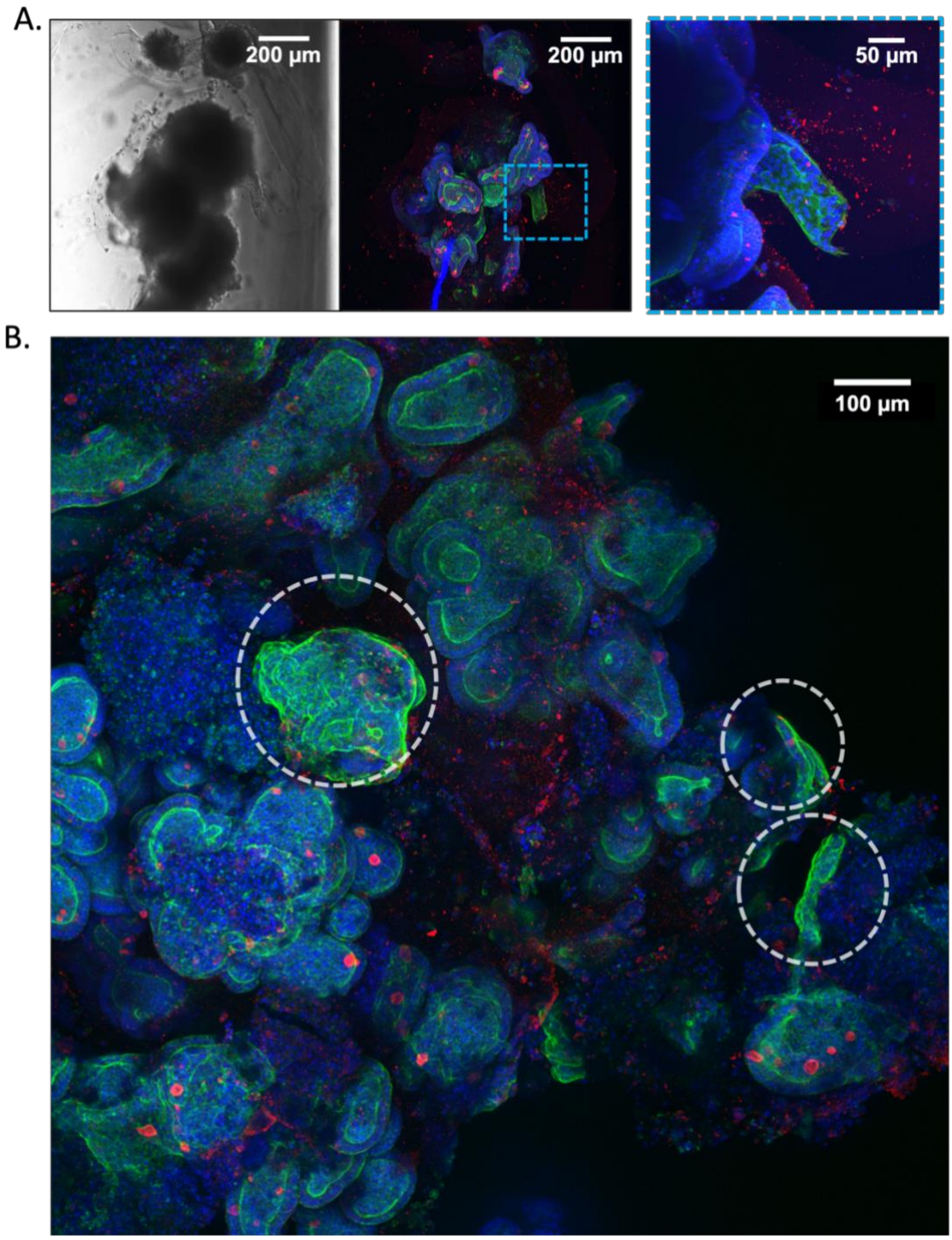

Figure 8 (A) Whole organoid showing 2D-3D hybrid morphology. Left: Bright field image of organoids. Center: Immunofluorescence image of intestinal epithelial with 2D-3D region highlighted. Right: 40x image of 2D-3D region. (B) 10x objective immunofluorescence image of intestinal epithelial tissue, with circled portions denoted areas with high expression of F-actin, suggesting surface breakthrough. Blue: DAPI, Green: F-Actin, Red: Lysozyme. Blue: DAPI, Green: F-Actin, Red: Lysozyme.

Analyzing the longest buds of organoids within dislodged filaments, we observed that the time of dislodging plays a significant role in subsequent organoid expansion, with early times of dislodging (i.e. dislodge at

day 0) resulting in the highest longest bud lengths (Figure 7B-C) and exhibiting a greater proportion of organoids with elongated budding structures (>500 μm) by day 12 of culture. Compared to the Matrigel-agarose core-shell filaments which had 1% organoids exhibiting elongated budding structures, day 0 and day 3-dislodged filaments had 5.4% and 3.9 (Figure 7C). These results confirm once more that the positive impact of agarose on organoid growth in the context of the Transwell setup did not translate over to the bioprinted context. We attribute this again to the absence of a separate media compartment adjacent to the organoid-laden Matrigel layer that is otherwise present in the Transwell setup.

Strikingly, there were a number of occurrences where organoids from dislodged filaments developed hybrid 2D-3D intestinal epithelial morphologies at day 12 that deviated from typical organoid shapes. Specifically, these epithelial tissues exhibited surface monolayers, marked by their cobblestone-like appearance, alongside standard folding/budding structures regularly seen in intestinal organoids (Figure 7D-E). That these monolayers exist on the surfaces and not in the bulk Matrigel is confirmed by orthogonal views produced using Immunofluorescence microscopy also reveals high expression of F-actin in both apical and basolateral surface for certain regions of epithelial tissue, including but not limited to those corresponding to surface monolayers (Figure 8). Since regular organoids grown in bulk Matrigel usually display F-actin on the luminal surface (i.e. the surface facing in), these regions of high F-actin on both surfaces would suggest a reorganization of epithelial cells and may be indicative of a transition from the folded/budding structure into a surface monolayer wherein epithelial cells are display apical-out polarity.

3.4. Discussion

Agarose is known to be a bioinert polysaccharide and unable to support cell adhesion and growth. In terms of mechanics, agarose is an order of magnitude stiffer than Matrigel and has a higher crossover frequency[33], allowing it to exhibit more gel-like/elastic behavior under the mechanical loading conditions associated with regular handling. As such, previous reports of using agarose in tissue engineering involve exploiting agarose's mechanical integrity and ease of molding to pattern physical barriers to guide neuron growth to

promote axonal regeneration[32] or to create custom *in vitro* neuronal networks[34]. For intestinal epithelial engineering, previous work with HCT116 cell lines grown in agarose-Matrigel composites display cell viability and spreading[31], but such has not been demonstrated for primary-derived intestinal epithelial cells. Our results in the Transwell and bioprinted filament contexts demonstrate that bioinert hydrogels such as unmodified agarose are capable of being used in tandem with Matrigel to support *in vitro* intestinal epithelial growth once certain conditions are met, namely sufficient levels of growth factors pertinent to intestinal stem cell biology. This contrasts with a 2017 paper which reported that monolayers grown on agarose-collagen substrates did not exhibit any measure of self-renewal[25]. We attribute this difference in outcome to variation in growth factor distribution, undefined composition of agarose and possible differences between culture requirements for intestinal 2D monolayers versus 3D organoids *in vitro*.

The occurrence of highly elongated budding structures (>500 μm in length) in Transwell cultures (and in dislodged filaments to a lesser extent) is likely the result of those particular budding structures exhibiting heightened proliferation rates that far surpass the rate at which new crypts can emerge. This is supported by computational simulation studies of multicellular structures that show how the occurrence/prevalence of tubulation/branching behavior depends on the relative time scales between patterning (e.g. cell signaling) and deformation (e.g. proliferation)[35]. Mechanistically, researchers have long identified the Wnt signaling pathway as responsible for promoting proliferation in intestinal epithelium, and that gradients in Wnt signaling can result in tissues that are polarized into distinct proliferative and differentiated domains[36,37]. We hypothesize that aspects of the Transwell dual layer setup accentuates Wnt signaling in the transverse (i.e. in-plane direction) and results in hyperpolarization of the organoid, so long as there is a sufficient level of growth factors at the initiation of culture.

Previous research has shown the importance of removing Wnt signaling antagonists (e.g. Dkk-1) secreted by intestinal epithelial cells to enhance tissue organization. It has been noticed that organoid densities play a non-negligible role in subsequent growth performance, with higher densities often promoting poorer

growth quality and smaller/shorter morphologies due to excess local Dkk-1 levels around the organoids[38,39]. In our Transwell dual layer setup, liquid media on the top compartment allows Wnt antagonists to diffuse out from the Matrigel layer and thus prevent buildup around the organoids. At the same time, there would be buildup of Wnt antagonists just underneath the organoids at the interface of the Matrigel and underlying agarose layers simply due to the relative difference in diffusion rates. This leaves only the tranverse directions along the Matrigel layer available for high levels of Wnt signaling and thus driving hyper-polarization and proliferation in the tranverse directions. Nevertheless, further studies on this elongation phenomenon should specifically interrogate the role played, if any, by Wnt antagonists such as Dkk-1 secreted by cells. At the same time, previous literature that documented the formation of elongated budding structures in intestinal organoids associated the elongated morphologies with a regenerative phenotype that emerges upon intestinal injury, and that YAP-signaling is heavily implicated in inducing and maintaining this phenotype[40,41]. Thus, targets associated with YAP-signaling should also be the focus of future mechanistic studies on the role of agarose in promoting intestinal growth and elongation.

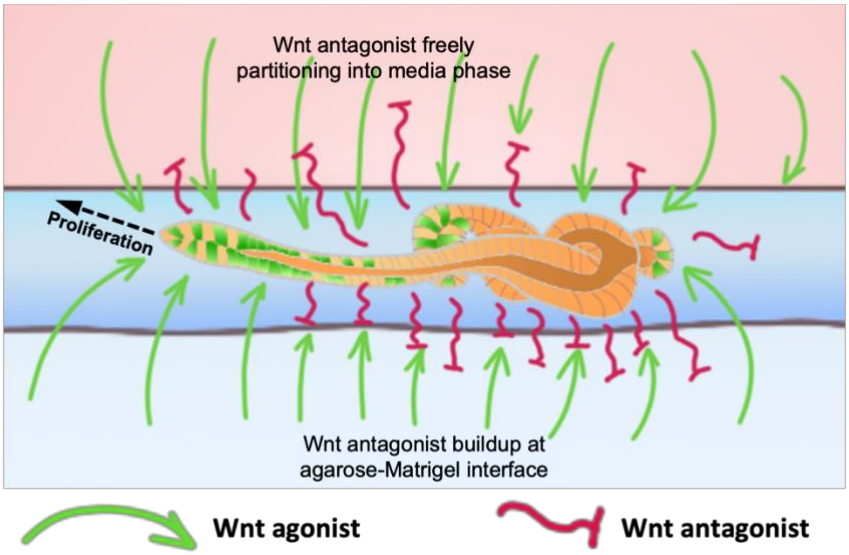

Figure 9. Schematic of dual layer effect leading to elongated organoids, with accumulation of Wnt antagonists leading to hyperpolarization of organoid to drive proliferation in the horizontal direction.

Standard intestinal epithelial culture using primary-derived cells typically consist of 2D surface monolayers or 3D organoids. Drawbacks of the former include lack of physiological architecture (e.g. crypts and villi) whereas the latter lacks accessibility to the apical surface/compartment. The hybrid 2D-3D morphology observed in intestinal epithelial tissues from dislodged filaments presents and interesting possibility to break the tradeoff inherent in 2D monolayers or tissue cultures. Factors that may contribute to the occurrence of hybrid 2D-3D morphologies include occasional fluid shear mid-culture and the emergence of organoids beyond the Matrigel-media interface. Future work should be aimed at interrogating the roles of these factors on intestinal epithelium morphogenesis using controlled platforms (e.g. microfluidic flow cells).

The development of core-shell Matrigel-agarose filaments reported in this work is part of a larger trend in tissue engineering wherein multiple biomaterials are arranged hierarchically to improve tissue growth, uniformity, visibility or usability or all of the above[42,43]. We had previously reported a workflow for extrusion bioprinting of agarose-Matrigel bioinks as an initial attempt at overcoming the limitations of individual hydrogel materials, namely the tradeoff between printability, mechanical integrity and cytocompatibility. Comparing both approaches, the 1:1 agarose-Matrigel blend used previously exhibited limited coherence and mechanical integrity. In contrast, the core-shell filament bioprinting approach from this paper has several key advantages in terms of reliability of filament quality (e.g. optical transparency, ease of handling) and workflow flexibility (e.g. customizable core-shell geometry, ability to manipulate the Matrigel core post-gelation). While the lack of adhesion between agarose and Matrigel allowed for the selective formation of thin Matrigel filaments, further development in the agarose-Matrigel material system should consider methods for tuning the chemistry of agarose or other similarly mechanically robust hydrogels to render it more adhesive to the Matrigel, thus limiting the occurrence of unintentional dislodging and enabling more consistent/stable positioning of Matrigel relative to agarose.

3.5. Conclusion & Outlook

In summary, we report how agarose-Matrigel dual layers can be used for intestinal organoid growth and expansion, documenting not only agarose's compatibility intestinal organoids, but also its crucial role in inducing a highly elongated morphology. These findings raises new possibilities on how different biomaterials can engineered to interact with various morphogen signaling to thus offer spatiotemporal control over tissue architecture and cellular fate. Moreover, using a core-shell layout, we present a bioprinting approach that is flexible in its ability to either generate continuous core-shell filaments or dislodged cores that support intestinal epithelial tissue growth *in vitro*. Overall, the approach presented herein is represents a continuing trend of engineering multiple hydrogel materials to improve the performance, capabilities or ease of experimentation in the area of tissue engineering and bioprinting.

3.6. References

1. Lindell, A. E., Zimmermann-Kogadeeva, M. & Patil, K. R. Multimodal interactions of drugs, natural compounds and pollutants with the gut microbiota. *Nat. Rev. Microbiol.* 1–13 (2022).
2. Ma, W. *et al.* Gut microbiota shapes the efficiency of cancer therapy. *Front. Microbiol.* **10**, (2019).
3. Wang, Z. *et al.* Gut flora metabolism of phosphatidylcholine promotes cardiovascular disease. *Nature* **472**, 57–65 (2011).
4. Koeth, R. A. *et al.* Intestinal microbiota metabolism of l-carnitine, a nutrient in red meat, promotes atherosclerosis. *Nat. Med.* **19**, 576–585 (2013).
5. Gregory, J. C. *et al.* Transmission of atherosclerosis susceptibility with gut microbial transplantation. *J. Biol. Chem.* **290**, 5647–5660 (2015).
6. Claesson, M. J. *et al.* Composition, variability, and temporal stability of the intestinal microbiota of the elderly. *Proc. Natl. Acad. Sci. U. S. A.* **108**, 4586–4591 (2011).
7. Jie, Z. *et al.* The gut microbiome in atherosclerotic cardiovascular disease. *Nat. Commun.* **8**, 1–11 (2017).
8. Holmqvist, S. *et al.* Direct evidence of Parkinson pathology spread from the gastrointestinal tract to the brain in rats. *Acta Neuropathol.* **128**, 805–820 (2014).
9. Scheperjans, F. *et al.* Gut microbiota are related to Parkinson's disease and clinical phenotype. *Mov. Disord.* **30**, 350–358 (2015).
10. Braniste, V. *et al.* The gut microbiota influences blood-brain barrier permeability in mice. *Sci. Transl. Med.* **6**, (2014).
11. Sampson, T. R. *et al.* Gut Microbiota Regulate Motor Deficits and Neuroinflammation in a Model of Parkinson's Disease. *Cell* **167**, 1469-1480.e12 (2016).
12. Mertsalmi, T. H. *et al.* More than constipation – bowel symptoms in Parkinson's disease and their connection to gut microbiota. *Eur. J. Neurol.* **24**, 1375–1383 (2017).
13. Pietrucci, D. *et al.* Dysbiosis of gut microbiota in a selected population of Parkinson's patients. *Parkinsonism Relat. Disord.* **65**, 124–130 (2019).
14. Kaplan, G. G. The global burden of IBD: From 2015 to 2025. *Nat. Rev. Gastroenterol. Hepatol.* **12**, 720–727 (2015).
15. Li, K., Feng, C., Chen, H., Feng, Y. & Li, J. Trends in Worldwide Research in Inflammatory Bowel Disease Over the Period 2012–2021: A Bibliometric Study. *Front. Med.* **9**, 1–11 (2022).
16. Thomas, H. *et al.* Global Atlas of Cardiovascular Disease 2000-2016: The Path to Prevention and Control. *Glob. Heart* **13**, 143–163 (2018).
17. James, B. *et al.* Contribution Of Alzheimer disease to mortality in the United States. *Neurology* **82**, 1302 (2014).

18. Winblad, B., Amouyel, P., Andrieu, S. & Ballard, C. Defeating Alzheimer's Disease and other dementias : a priority for European science and society. *Lancet Neurol.* **15**, 455–532 (2016).
19. Association, A. Alzheimer's disease facts and figures. *Alzheimer's Dement.* **15**, 321–387 (2019).
20. Sontheimer-Phelps, A. *et al.* Human Colon-on-a-Chip Enables Continuous In Vitro Analysis of Colon Mucus Layer Accumulation and Physiology. *Cmgh* **9**, 507–526 (2020).
21. Jalili-Firoozinezhad, S. *et al.* A complex human gut microbiome cultured in an anaerobic intestine-on-a-chip. *Nat. Biomed. Eng.* **3**, (2019).
22. Co, J. Y., Margalef-Català, M., Monack, D. M. & Amieva, M. R. Controlling the polarity of human gastrointestinal organoids to investigate epithelial biology and infectious diseases. *Nat. Protoc.* **16**, 5171–5192 (2021).
23. Sato, T. *et al.* Single Lgr5 stem cells build crypt-villus structures in vitro without a mesenchymal niche. *Nature* **459**, 262–265 (2009).
24. Zhang, Y. G., Wu, S., Xia, Y. & Sun, J. Salmonella-infected crypt-derived intestinal organoid culture system for host–bacterial interactions. *Physiol. Rep.* **2**, 1–11 (2014).
25. Wang, Y. *et al.* Self-renewing Monolayer of Primary Colonic or Rectal Epithelial Cells. *Cmgh* **4**, 165-182.e7 (2017).
26. Wang, Y. *et al.* In Vitro Generation of Mouse Colon Crypts. *ACS Biomater. Sci. Eng.* **3**, 2502–2513 (2017).
27. Nikolaev, M. *et al.* Homeostatic mini-intestines through scaffold-guided organoid morphogenesis. *Nature* **585**, 574–578 (2020).
28. Broguiere, N. *et al.* Growth of Epithelial Organoids in a Defined Hydrogel. *Adv. Mater.* **30**, (2018).
29. Gjorevski, N. *et al.* Designer matrices for intestinal stem cell and organoid culture. *Nature* **539**, 560–564 (2016).
30. Langlands, A. J. *et al.* Paneth Cell-Rich Regions Separated by a Cluster of Lgr5+ Cells Initiate Crypt Fission in the Intestinal Stem Cell Niche. *PLoS Biol.* **14**, 1–31 (2016).
31. Fan, R. *et al.* Bio-printing cell-laden Matrigel-agarose constructs. *J. Biomater. Appl.* **31**, 684–692 (2016).
32. Han, S. *et al.* Implantation of a Matrigel-loaded agarose scaffold promotes functional regeneration of axons after spinal cord injury in rat. *Biochem. Biophys. Res. Commun.* **496**, 785–791 (2018).
33. Zuidema, J. M., Rivet, C. J., Gilbert, R. J. & Morrison, F. A. A protocol for rheological characterization of hydrogels for tissue engineering strategies. *J. Biomed. Mater. Res. - Part B Appl. Biomater.* **102**, 1063–1073 (2014).
34. Krumpholz, K. *et al.* Agarose-Based Substrate Modification Technique for Chemical and Physical Guiding of Neurons In Vitro. *ACS Appl. Mater. Interfaces* **7**, 18769–18777 (2015).
35. Okuda, S., Miura, T., Inoue, Y., Adachi, T. & Eiraku, M. Combining Turing and 3D vertex models reproduces autonomous multicellular morphogenesis with undulation, tubulation, and branching. *Sci. Rep.* **8**, 1–15 (2018).
36. Attayek, P. J. *et al.* In vitro polarization of colonoids to create an intestinal stem cell compartment. *PLoS One* **11**, 1–23 (2016).
37. Libby, A. R. G. *et al.* Axial elongation of caudalized human organoids mimics aspects of neural tube development. *Dev.* **148**, (2021).
38. Shin, W., Hinojosa, C. D., Ingber, D. E. & Kim, H. J. Human Intestinal Morphogenesis Controlled by Transepithelial Morphogen Gradient and Flow-Dependent Physical Cues in a Microengineered Gut-on-a-Chip. *iScience* **15**, 391–406 (2019).
39. Shin, W. *et al.* Spatiotemporal Gradient and Instability of Wnt Induce Heterogeneous Growth and Differentiation of Human Intestinal Organoids. *iScience* **23**, 101372 (2020).
40. Qu, M. *et al.* Establishment of intestinal organoid cultures modeling injury-associated epithelial regeneration. *Cell Res.* **31**, 259–271 (2021).
41. Sprangers, J., Zaalberg, I. C. & Maurice, M. M. Organoid-based modeling of intestinal development, regeneration, and repair. *Cell Death Differ.* **28**, 95–107 (2021).
42. Mistry, P. *et al.* Bioprinting Using Mechanically Robust Core–Shell Cell-Laden Hydrogel Strands. *Macromol. Biosci.* **17**, 1–8 (2017).
43. Tallapragada, N. P. *et al.* Inflation-collapse dynamics drive patterning and morphogenesis in intestinal organoids. *Cell Stem Cell* **28**, 1516-1532.e14 (2021).

3.7 Data Tables

Table 1. List of median organoid projected area fold-increase values over the 13-day culture and respective p-values obtained using Mann-Whitney U-test. Dual layers consisted of 3mm 1.5% w/v agarose.

Day	Matrigel-only organoid projected area fold-increase	Dual layer organoid projected area fold-increase	n (Matrigel-only)	n (Dual layer)	P value
3	2.572	2.45	23	22	0.4014
5	5.596	5.928			0.6088
7	8.05	10.06			0.11
9	11.08	12.54			0.3164
11	13.73	19.24			0.0815
13	16.49	34.35			0.0339

Table 2. List of median longest bud lengths over the 13-day culture and respective p-values obtained using Mann-Whitney U-test.

Day	Matrigel-only Longest bud length (μm)	Dual layer Longest bud length (μm)	n (Matrigel-only)	n (Dual layer)	P value
3	79.8	62.88	181	90	0.4014
5	145.4	125.4	185	89	0.6088
7	177.7	199.3	236	92	0.11
9	238.5	246.5	60	42	0.3164
11	266.5	356	64	39	0.0815
13	174	333	64	38	0.0339

Table 3. List of median organoid projected area fold-increase values over the 7-day culture for different thicknesses. All dual layers consisted of 1.5% w/v agarose.

Day	Matrigel-only organoid projected area fold-increase	0.5mm organoid projected area fold-increase	1.0mm organoid projected area fold-increase	3.0mm organoid projected area fold-increase	n (Matrigel-only)	n (0.5mm)	n (1.0mm)	n (3.0mm)
3	2.572	2.99	2.11	2.45	23	16	9	22
5	5.596	7.835	5.67	5.928				
7	8.05	15.61	11.54	10.06				

Table 4. List of median longest bud lengths over the 7-day culture for different thicknesses. All dual layers consisted of 1.5% w/v agarose.

Day	Matrigel-only Longest bud length (μm)	0.5mm Longest bud length (μm)	1.0mm Longest bud length (μm)	3.0mm Longest bud length (μm)	n (Matrigel-only)	n (0.5mm)	n (1.0mm)	n (3.0mm)
3	79.8	82.15	49.28	62.88	181	59	35	90
5	145.4	179	153.2	125.4	185	64	36	89
7	177.7	155.1	229.7	199.3	236	60	38	92

Table 5. List of median organoid projected area fold-increase values over the 7-day culture for different agarose concentrations. All dual layers have 1mm-thick agarose.

Day	Matrigel-only organoid projected area fold-increase	0.5% w/v organoid projected area fold-increase	1.5% w/v organoid projected area fold-increase	3.0% w/v organoid projected area fold-increase	n (Matrigel-only)	n (0.5%)	n (1.5%)	n (3.0%)
3	2.572	3.15	2.11	3.365	23	8	9	12
5	5.596	8.595	5.67	7.245				
7	8.05	11.4	11.54	10.5				

Table 6. List of median longest bud lengths over the 7-day culture for different agarose concentrations. All dual layers consisted of 1mm-thick agarose.

Day	Matrigel-only organoid projected area fold-increase	0.5% w/v organoid projected area fold-increase	1.5% w/v organoid projected area fold-increase	3.0% w/v organoid projected area fold-increase	n (Matrigel-only)	n (0.5%)	n (1.5%)	n (3.0%)
3	79.8	164.8	49.28	92.16	181	63	35	73
5	145.4	284	153.2	208.2	185	53	36	76
7	177.7	267.6	229.7	232.2	236	137	38	77

Table 7. List of median organoid projected area fold-increase values over the 7-day culture for conditioned vs unconditioned agarose. All dual layers have 3mm 1.5% w/v. agarose.

Day	Unconditioned agarose organoid projected area fold-increase	Conditioned agarose organoid projected area fold-increase	n (Unconditioned)	n (Conditioned)
3	2.906	3.45	38	28
5	7.15	7.33		
7	10.11	10.16		

Table 8. List of median longest bud length over the 7-day culture for conditioned vs unconditioned agarose. All dual layers have 3mm 1.5% w/v. agarose.

Day	Matrigel-only organoid projected area fold-increase	0.5% w/v organoid projected area fold-increase	n (1.5%)	n (3.0%)
3	62.88	122.3	90	112
5	125.4	157.7	89	119
7	199.3	156.6	92	123

Table 9. List of median organoid projected area fold-increase values over the 7-day culture for different top compartment media. All dual layers have 3mm 1.5% w/v. agarose.

Day	Growth media organoid projected area fold-increase	DMEM organoid projected area fold-increase	PBS organoid projected area fold-increase	n (growth factor)	n (DMEM)	n (PBS)
3	2.906	1.22	1.245	38	12	10
5	7.15	1.41	1.555			
7	10.11	1.405	1.39			

Table 10. List of median longest bud length over the 7-day culture. All dual layers have 3mm 1.5% w/v. agarose.

Day	Growth media longest bud length (µm)	DMEM longest bud length (µm)	PBS longest bud length (µm)	n (growth factor)	n (DMEM)	n (PBS)
3	2.906	1.22	1.245	90	28	21
5	7.15	1.41	1.555	89	27	19
7	10.11	1.405	1.39	92	26	15

Table 11. List of median organoid projected area fold-increase values over the 7-day culture for different combinations of top media and agarose conditioning. All dual layers have 3mm 1.5% w/v. agarose.

Day	Growth media (unconditioned) organoid projected area fold-increase	DMEM (conditioned) organoid projected area fold-increase	n (growth media, unconditioned)	n (DMEM conditioned)
3	2.906	2.155	38	12
5	7.15	4.68		
7	10.11	8.35		

Table 12. List of median longest bud length over the 7-day culture for conditioned vs unconditioned agarose. All dual layers have 3mm 1.5% w/v. agarose.

Day	Matrigel-only organoid projected area fold-increase	0.5% w/v organoid projected area fold-increase	n (1.5%)	n (3.0%)
3	62.88	84.19	90	28
5	125.4	123.6	89	29
7	199.3	153.4	92	26

Table 13. List of median longest bud length over the 7-day culture for different bioprinted filaments.

Day	2.5mm Ag 0.75mm Mat longest bud length (µm)	4.5mm Ag 0.75mm Mat longest bud length (µm)	4.5mm Ag 1.5 mm Mat longest bud length (µm)	n (2.5mm Ag, 0.75mm Mat)	n (4.5mm Ag, 0.75mm Mat)	n (4.5mm Ag, 1.5mm Mat)
6	118.7	89.57	59.49	164	59	127
12	185.9	173.5	97.12	134	54	100

Table 14. List of median longest bud length over the 7-day culture for different dislodge times

Day	Day 0 dislodge longest bud length (µm)	Day 6 dislodge longest bud length (µm	Day 12 dislodge longest bud length (µm	n (day 0 dislodge)	n (day 6 dislodge)	n (day 12 dislodge)
6	140.6	8086	109.3	216	107	257
12	177.6	200.1	133.4	111	71	146